

https://dspace.org/

Characterisation and surface finish evaluation of Direct Energy Deposited AlCoCrCuFeNi High Entropy Alloys

Modikwe, Thembisile Patience

2024-01
University of the Witwatersrand, Johannesburg
https://hdl.handle.net/10539/38881

Modikwe, Thembisile Patience. (2024). Characterisation and surface finish evaluation of Direct Energy Deposited AlCoCrCuFeNi High Entropy Alloys. [Master's dissertation, University of the Witwatersrand, Johannesburg]. WIReDSpace. https://hdl.handle.net/10539/38881

Downloaded from a DSpace repository. https://dspace.org/



UNIVERSITY OF THE
WITWATERSRAND,
JOHANNESBURG

Characterisation and surface finish evaluation of Direct Energy Deposited AlCoCrCuFeNi High Entropy Alloys

By

Thembisile Patience Modikwe

673864

A dissertation submitted to the school of Chemical and Metallurgical Engineering, Faculty of Engineering and Built Environment, University of the Witwatersrand, Johannesburg. In fulfilment of the requirements for the degree of Master of Science in Engineering

January 2024

Declaration

I declare that the content in this dissertation is my own unaided work. It is being submitted for the degree of Master of Science in Engineering to the University of the Witwatersrand, Johannesburg. I also confirm that it has not been submitted before for any degree or examination to any other university and that all sources are acknowledged by means of referencing.



Signature of candidate

10 January 2024

Abstract

This study focused on the use of direct energy deposited (DED) techniques for the fabrication of AlCrCoCuFeNi high entropy alloy (HEAs) samples. HEAs have become a ground-breaking research field that provides solutions to complex problems in the aerospace industry. The industry requires improvement in the application of structural materials that are well-functioning at a low cost for example turbine blades. The fabrication of HEAs via DED commonly produces poor surface finish Ra in the range of 5 µm - 20 µm due to the layer-by-layer deposition method, as a result, it fails the industrial application requirements where the usual range of roughness tolerance required in the industry ranges from Ra is 0.8 µm < Ra < 1.6 µm thus, the need to deploy post-processing methods.

This study focused on electropolishing (EP) and centrifugal barrel finishing (CBF) of AlCrCoCuFeNi-HEA samples. The polishing was performed using 80% methanol and 20% per-chloric acid solution used as the electrolyte. The samples were polished for 30 and 60 seconds in a Struers LectroPol-5 electrolytic polishing and etching device. The surface removal at 1200W for 30 sec on sample a was 50.29%, 58.65% for sample b, and 75.48% for sample c. The surface removal at 1400W for 60 sec on sample d is 63.25%, 45% for e, and 49.19% for f. The samples were polished for 7 and 14 hours in a CB320-CBF. During the period of 14 hours, a surface removal where the proportion of material removed for sample a was 55.37%, sample b was 43.13%, and sample c was 32.2% at a laser power of 1200W. After 7 hours of polishing, sample d achieved a surface removal of 86.02%, sample e achieved a surface removal of 43.18%, and sample f achieved a surface removal of 90% at a power of 1400W.
Oxidation tests were conducted in static air at 1000˚C for 200h. The presence of FCC, BCC, and Fe_2O_3 oxide scales resulted in a noticeable increase in mass, with Fe_2O_3 scales being the most prevalent.

Keywords: Additive Manufacturing, High Entropy Alloy, Electropolishing, Centrifugal Barrel Finishing, High-temperature Oxidation, Surface Roughness, Direct Energy Deposition

Acknowledgements

To God whose continual plans are to give me hope and a future.

I would like to thank my supervisor Prof Nthabiseng Maledi for giving me an opportunity to work with her on my studies. Her guidance and constructive contribution has played an important role in completing this work.

An utmost appreciation to my co-supervisor Dr Ntombi Mathe-Maleboho for her unwavering support, guidance, patience, availability, encouragements and all the effort of helping me get to where I am today. The technical assistance throughout my research has led to the success of my studies. I will forever be grateful for her support.

I would like to thank the CSIR National Laser Center (NLC) team for their support. Prof Sisa Pityana for his constant support and guidance throughout my studies. Dr Lerato Tshabalala for always being available to assist me with anything I needed for this project. Mr Nana Arthur for his guidance and encouragement whenever I needed assistance. Mr Samuel Skhosana for taking the time to assist me with fabrication of samples. Mr Washington for assisting me with polishing the sample on the barrel finisher and the rest of the team for their moral support, I truly appreciate it.

I would also like to thank Miss M Dada from Tshwane University of Technology for the sincere support and guidance she has shown me throughout this journey. I would not have made it this far, for that I am truly grateful.

To my husband, Mr Simon Modikwe thank you for the continual love, support and understanding you have shown throughout this journey. You were with me through it all and you kept on supporting me. I truly appreciate you.

To my parents (Angie and Muso Dlamini) and younger brother (Dumisani Dlamini) I appreciate you guys so much, thank you the constant support you have shown me it has not been an easy journey, but we keep on keeping on.

I am honoured to have been selected as the CSIR bursary recipient, I am truly thankful for the financial support which allowed me to complete my studies.

List of contributions

Modikwe, T., Maledi, N., Mathe, N., Pityana, S., Dada, M. and Makoana, W., Post-processing of direct metal deposited AlCrCoCuFeNi HEA using centrifugal barrel finishing. In *MATEC Web of Conferences* (Vol. 370, p. 06007). EDP Sciences.

Table of Content

Declaration ..... **i**

Abstract ..... **ii**

Acknowledgements ..... **iii**

List of contributions ..... **iv**

List of Figures ..... **viii**

List of Tables ..... **x**

List of Abbreviations ..... **xi**

Chapter 1 ..... **1**

1.1 Background 1

1.2 Aim 4

1.3 Objectives 5

1.4 Research question 5

1.5 Delineation 5

1.6 Research problem 6

1.7 Hypothesis 7

1.8 Significance of this study 7

1.9 Outline of the dissertation 7

Chapter 2 ..... **9**

2.1 Additive Manufacturing Technology 9

2.1.1 Additive Manufacturing Applications 10

2.2 Laser deposition process 13

2.2.1 Wire feed system 14

2.2.2 Powder-bed fusion 15

2.2.3 Direct Energy Deposition 16

2.3 High entropy alloys 18
2.3.1 The four-core effect 19
2.3.2 High entropy alloy applications 24
2.4 Post-surface Treatment 25
2.4.1 Electropolishing 25
2.4.2 Centrifugal Barrel Finishing 28
2.4.3 Surface roughness measurement 29
2.5 High-Temperature Oxidation 30
2.6 Summary 33
Chapter 3 34
3.1 Material 34
3.2 Powder analysis 34
3.3 Deposition process 35
3.3.1 Process parameters 35
3.4 Sample preparation 36
3.5 Characterisation of as-built and processed samples 38
3.5.1 Density Measurement 38
3.5.2 Optical microscope 39
3.5.3 Scanning electron microscope 39
3.5.4 XRD analyses 39
3.5.5 Hardness measurement 39
3.6 Post-processing 40
3.6.1 Electropolishing 40
3.6.2 Centrifugal Barrel Finishing 42
3.6.3 Surface analysis 43
3.7 High temperature oxidation 43
3.8 Conclusion 43
Chapter 4 44

4.1 Powder analysis 44
4.1.1 Chemical composition 44
4.1.2 Morphology and Particle Size Distribution 45
4.2 Process development of the samples 50
4.2.1 Density using Archimedes Principle 51
4.2.2 Microstructural analysis 53
4.2.3 Phase analysis 59
4.2.4 Hardness 61
4.3 Post-Processing 63
4.3.1 As-built sample 63
4.3.2 Electropolishing 67
4.3.3 Centrifugal Barrel Finishing 71
4.4 High-temperature oxidation 76
Chapter 5 82
5.1 Conclusion 82
5.2 Recommendations 84
References 86
Appendix A: Angle of internal friction 109
Appendix B: Measured densities of AlCrCoCuFeNi-HEA using Archimedes principal. 110
Appendix C: 2022 RAPDASA-RobMech-PRASA-CoSAAMI Conference 111

List of Figures

Figure 2.1: Additive manufacturing process illustration 10
Figure 2.2: Additive manufacturing industrial role in different sectors 12
Figure 2.3: Classification of AM categories 13
Figure 2.4: LBAM manufacturing process divided into three categories 14
Figure 2.5. Schematic representation of the Direct Energy Deposition 16
Figure 2.6 XRD patterns of the addition of elements in the series of alloys 20
Figure 2.7 BCC lattice that contains a) Cr b) Cr and V c) Cr, Ni, Fe, Co, Al, Ti 21
Figure 2.8. Potential energy changes when the Ni atom migrates 22
Figure 2.9. The hardness of AlxCoCrCuFeNi alloy as Al content increases 23
Figure 2.10 An electropolishing diagram with labelling 26
Figure 2.11 Polarization curve used in electropolishing system 28
Figure 3.1 3kW IPG Kuka robot with furnace 35
Figure 3.2: DED samples produced using the KUKA robot 37
Figure 3.3 Auto-lab Potentiostat (PGSTAT302) 40
Figure 3.4. Struers LectroPol-5 electropolishing machine 41
Figure 3.5. CB320-CBF machine and ceramic media used to polish the samples 42
Figure 4.1: SEM micrograph of AlCrCoCuFeNi-HEA powder sample (a) 500×, (b) 500×, (c) 500×, (d) 500×, (e) 500×and (f) 500× at different areas of the same powder. 46
Figure 4.2. Particle size distribution of AlCrCoCuFeNi-HEA powder 47
Figure 4.3: Powder yield locus schematic diagram of AlCrCoCuFeNi powder 49
Figure 4.4. Unconfined yield strength on major principal stress. 50
Figure 4.5 optical microscopic images of sample a, produced at 1200W, 0.48mm/s. 54
Figure 4.6 Optical Microscope images of sample b, produced at 1200W, 0.6mm/s. 55
Figure 4.7 Optical Microscope images of sample c, produced at 1200W, 0.72mm/s. 56
Figure 4.8 Optical Microscope images of sample d, produced at 1400W, 048mm/s. 56
Figure 4.9 Optical Microscope images of sample e, produced at 1400W, 06mm/s. 57
Figure 4.10 Optical Microscope images of sample f, produced at 1400W, 072mm/s. 58
Figure 4.11 X-ray diffraction pattern of as-built AlCrCoCuFeNi HEA: (a) at different laser power and scan speed, (b) enlarged (200) peak. 60

Figure 4.12. Hardness profile of samples a, b, c, d, e and f at different laser power and scanning speed. 62
Figure 4.13 SEM images of untreated as-built samples a_3, b_3, c_3, d_3, e_3, and f_3 64
Figure 4.14 Roughness profile of the untreated as-built samples a_3, b_3, c_3, d_3, e_3, and f_3 65
Figure 4.15Three-dimension topographical representation of the untreated sample a_3, b_3, c_3, d_3, e_3 and f_3. 66
Figure 4.16 Linear sweep voltammetry graph of AlCrCoCuFeNi HEA 67
Figure 4.17 The electropolished SEM micrographs of AlCrCoCuFeNi HEA 68
Figure 4.18. Roughness profile of the electropolished samples a_1, b_1, c_1, d_1, e_1 and f_1 69
Figure 4.19 Three-dimension topographical representation of the electropolished sample a_1, b_1, c_1, d_1, e_1 and f_1 70
Figure 4.20 SEM images of centrifugal barrel finished samples a_2, b_2, c_2, d_2, e_2, and f_2. 72
Figure 4.21. Roughness profile of the centrifugal barrel finished sample a_2, b_2, c_2, d_2, e_2, f_2. 73
Figure 4.22 Three-dimension topographical representation of the CBF sample a_2, b_2, c_2, d_2, e_2 and f_2. 74
Figure 4.23. DED untreated as-built samples (i) (iii) and CBF treated samples (ii) (iv) 75
Figure 4.24 The mass change of samples a, b, c, d, e, and f at 1000˚C for 200h 77
Figure 4.25 XRD spectrum of oxidized samples after 200 hours. 78
Figure 4.26 SEM surface images of AlCrCoCuFeTi-HEA after oxidizing for 200h 80

List of Tables

Table 3.1: Laser process parameters of AlCoCrCuFeNi-HEA 36
Table 3.2: EP optimum process parameters 41
Table 3.3: CBF process parameters 42
Table 4.1: Chemical composition of AlCrCoCuFeNi-HEA powder (wt. %) 45
Table 4.2: Characteristics values for the particle size distribution 47
Table 4.3: Shear cell test properties of the AlCrCoCuFeNi-HEA powder 48
Table 4.4: Densities of AlCrCoCuFeNi-HEA samples processed at different conditions. 52
Table 4.5: Average hardness of samples a, b, c, d, e, and f 61
Table 4.6: The untreated result of as-bult samples a3, b3, c3, d3, e3, and f3. 65
Table 4.7: Roughness profile of the electropolished samples a1, b1, c1, d1, e1, and f1. 69
Table 4.8: Presents the roughness profile of CBF samples a2, b2, c2, d2, e2, and f2 72
Table 4.9: The average mass change per surface area 78

List of Abbreviations

AM	Additive Manufacturing
3D	Three-Dimensional
LBAM	Laser-based additive manufacturing
HEAs	High Entropy Alloys
DED	Direct Energy Deposition
LENS	Laser Engineering Net Shaping
LMD	Laser Metal Deposition
SLM	Selective Laser Melting
FCC	Face-Centered Cubic
BCC	Body-Centered-Cubic
HCP	Hexagonal Close Packed
EP	Electropolishing
CBF	Centrifugal Barrel Finishing
BF	Barrel Finishing
Ra	Average Roughness
Rz	Mean Roughness Depth
ASTM	American Society for Testing
CAD	Computer-aided design
EBF^3	Electron Beam Freeform Fabrication
WLAM	Wire Laser Additive Manufacturing
WAAM	Wire and Arc Additive Manufacturing

SLS	Selective Laser Sintering
SEM	Scanning Electron Microscope
EDS	Energy-dispersive X-ray spectroscopy
DARPA	Defence Advance Research Project Agency
SPM	Scanning Probe Microscopy
AFM	Atomic Force Microscopy
SCE	Saturated calomel electrode
LSV	Linear sweep voltammetry
XRD	X-ray diffraction
MPS	Major principal stress
UYS	Unconfined yield strength
AIF	Effective angle of internal fraction
FF	Flow function
MCS	Minor consolidation stress
BD	Bulk density

Chapter 1
Introduction

This chapter serves as an introductory section, with a broad overview of the research, highlighting process development of AlCoCrCuFeNi high entropy alloys (HEA), and addressing the aim, objectives, delineation, research problem, hypothesis statement, and the significance of the study.

1.1 Background

Additive Manufacturing (AM) also known as three-dimension (3D) printing, is a technology that is used to produce complex shapes in a layer-by-layer technique (Ingrassia *et al*., 2017). AM has become the new breeding space of ground-breaking technologies used across material science fraternities to produce innovative solutions to complex problems (Murr, 2014; Protomatic, 2015; Kok, 2018;). With the advancement of AM over the years, its technologies have been the centre of attention. This is attributed to its attractive characteristics such as reduced cost and energy, rapid production of intricate components, high reliability and a higher level of design freedom. This is contrary to conventional methods such as subtractive and formative manufacturing techniques, which involve material removal through drilling, grinding or casting into moulds (Conner, 2014; Pereira, 2019).

Numerous AM techniques have been used to develop process parameters of metallic materials in the laser-based additive manufacturing (LBAM) field. These methods can be classified into three categories: powder feed, powder bed fusion and wire feed process (Shiratori, 2016). In all LBAM methods, parameter optimisation is essential to avoid detrimental effects forming defects such as porosity, cracks, unmelted powder, high dilution and thermal fatigue (Rahman *et al*., 2019). The most studied and optimised process parameters are powder flow rate, scanning speed, laser power, layer thickness, hatch spacing and gas flow rate (Mahamood and Akinlabi, 2017).

Direct Energy Deposition (DED) technique in additive manufacturing has attracted numerous manufacturing industries such as the automotive, aerospace, and medical fields. This is mainly because of its ability to produce excellent mechanical bonding with the substrate, low porosity products, and high cooling rates and allows for the building of geometrically complex parts (Sexton *et al.*, 2002; Freire *et al.*, 2020). The DED has been successful over the years in producing metallic compounds and alloys, including high entropy alloys (Dezaki *et al.*, 2022).

Yeh *et al*. (2004) defined HEAs as alloys that contain at least five principal elements in an equiatomic or near equiatomic composition in the range of 5 – 35 at. %. They form face-centred cubic (FCC), body-centred-cubic (BCC), hexagonal close-packed (HCP) or a mixture of the three rather than complex phases and intermetallic compounds (Mishra and Shahi, 2018). These alloys have become the centre of attraction due to the attractive characteristics they possess such as high strength, high hardness, great fatigue resistance, excellent wear and oxidation resistance (Chuang *et al*., 2011; Gorr *et al*., 2015; Wen *et al*., 2009). The attractive characteristics are due to the four core effects of HEAs; sluggish diffusion effects, high-entropy effects, cocktail effects, and lattice distortion effects (Zhang *et al*., 2014).

The continual development of HEAs is required due to the constant need for improved materials to conform to the standards of recent technological and manufacturing demands. Such can be achieved by improving mechanical properties and adjusting the phase structure of the alloys. There are various methods used to improve mechanical properties of HEAs such as element addition, controlling the solidification process, thermo-mechanical alloying, heat treatment, or parameter optimisation (Li, 2016). For example the preliminary study by Dada *et al.*, (2021a) found that increasing the scanning speed of AlCoCrFeNiCu resulted in the formation of a BCC phase with very low energy densities and improved hardness properties. Mahamood and Akinlabi (2017) established that a higher laser powder flow rate produced improved Ti6Al4V microhardness.

Frequently used additive manufacturing methods for HEAs are powder feed and powder bed fusion methods (Cui, 2017). In a powder feed system, the powder is melted by the laser (with single or multiple nozzles) to form a melt pool (Parry *et al*., 2016). A powder feed system also known as Direct Energy Deposition (DED) contains Laser Metal Deposition (LMD) and Laser Engineering Net Shaping (LENS) (Thompson *et al.*, 2015; Dobbelstein *et al*., 2019). In powder bed fusion the powder is melted by high energy (single or multiple nozzles) laser or electron beam in a layer-by-

layer fashion (Parry *et al*., 2016). Powder bed fusion includes Selective Laser Melting (SLM) (Zhou *et al*., 2019).

Additive manufacturing has produced noteworthy, finished products which have captured interest in industries. However, the average surface roughness (Ra) of the as-built products usually ranges from 5 - 20 µm, which does not meet the industrial requirements (Wall *et al*., 2009; Raines *et al*., 2010; Strano *et al*., 2013b). The surface quality of AM produced components is substandard because of the layer-by-layer manufacturing process. As a result, post-processing treatment is required to improve the surface quality of the finished product. Various post-processing treatments have been used, which include electrolytic polishing, laser polishing, machining, ultrasonic polishing, chemical polishing also known as electropolishing (EP) and centrifugal barrel finishing (CBF) (Habibzadeh *et al*., 2014; Lyczkowska *et al*., 2014).

This research focuses on EP and CBF methods to reduce the surface roughness of DED-produced high entropy alloys. Both polishing methods have shown significant surface roughness reduction output. Aksu *et al*. (2016) used EP to produce a smooth surface on Fe-Ni-Co alloy in an acetic acid-perchloric acid electrolyte.

Huang *et al*. (2008) established that more than 50 vol.% of $HClO_4$ provided better anodic dissolution on Inconel 718 alloy and produced a bright surface on the sample. The advantage of this process is that it can be applied to complex shapes or sizes, since no contact is made between the workpiece and the cathode. (Rodriguez *et al*., 2020; Landolt *et al*., 2003). However, some chemicals tend to adversely attack the finished surface. For instance, Chen *et al*. (2005) found that 304SS is prone to pitting in a chloride environment.

Low-surface manufactured alumide® jewellery was polished using the CBF method. The polishing process resulted in a smooth attractive metallic lustre surface (De Beer *et al*., 2012). Polishing can be applied to complex shapes, sizes, or materials, as it uses a ceramic media and polishing liquid to achieve the desired surface. However, the process of polishing requires the operator to be highly involved in the manual loading and unloading of the sample(s).

Based on the environment that the components are subjected to during application, such as high temperature and corrosion, it is crucial to understand the high-temperature oxidation of the HEA samples after polishing. High-temperature oxidation is the exposure of metals or alloys at high

temperatures in the presence of oxygen (Parimin *et al*., 2022). High-temperature oxidation has been used to determine the service life and performance of metals or alloys (Sheng *et al*., 2013). Conventional alloys such as Ni-based alloys have been used for high-temperature oxidation because of their ability to resist oxidation at elevated temperatures (Parimin *et al*., 2022). The alloy forms a Cr_2O_3 oxide scale which contributes to the formation of the protective behaviour in high temperatures.

The HEAs are slowly replacing the use of conventional alloys in high-temperature oxidation environments due to the alloys having the ability to accommodate higher concentrations of the elements that are necessary to form a protective oxide scale (Arshad *et al.*, 2022) and their microstructural stability at high-temperature environments (Butler and Weaver, 2016b).

This study focuses on:

- The development of process parameters of AlCoCrCuFeNi-HEA
- The post-surface finish of AlCoCrCuFeNi-HEA using EP and CBF methods to polish the samples.
- Lastly, to investigate the high-temperature oxidation behaviour of AlCoCrCuFeNi-HEA at different laser scan speed and laser power.

This work will contribute to the limited body of knowledge in the study of the surface finishing of additively manufactured high entropy alloys.

1.2 Aim

This research aims to analyse the effect of laser processing parameters during DED AlCoCrCuFeNi-HEA and improving the surface finishing of produced samples by using centrifugal barrel finishing and electropolishing post-processing methods. The research further investigates the influence of different laser scanning speed and laser power on the high-temperature oxidation properties of DED AlCoCrCuFeNi-HEA.

1.3 Objectives

The primary aims of this study were achieved by addressing the following objectives:

- To produce AlCoCrCuFeNi-HEA samples using direct energy deposited samples with optimised laser parameters.
- To evaluate microstructural and mechanical properties of produced samples.
- To study the effect of laser parameters on the surface properties of AlCoCrCuFeNi-HEAs before and after surface finishing.
- To improve the post-surface finish of the as-built samples using centrifugal barrel finishing and electropolishing of AlCoCrCuFeNi high entropy alloy.
- To determine the effect of laser processing parameters on the high-temperature oxidation behaviour of AlCoCrCuFeNi high entropy alloy.

1.4 Research question

- What effect will the process parameters have on mechanical properties of laser-deposited AlCoCrCuFeNi-HEA?
- How will electropolishing and centrifugal barrel finishing improve the surface roughness?
- What effect does high-temperature oxidation have on the AlCoCrCuFeNi-HEA at different scan speed and laser parameter parts?

1.5 Delineation

All samples were produced using AlCoCrCuFeNi-HEA powder. This study focused on the process parameter development of AlCoCrCuFeNi-HEAs samples using the DED technique and the development of the post-surface finish at different process parameters using EP and CBF methods. Furthermore, the evaluated the effect of different laser processing parameters on the high-temperature oxidation behaviour of AlCoCrCuFeNi-HEA.

1.6 Research problem

Previously, additive manufacturing processes have raised concerns regarding the microstructural properties of the as-built components. Currently, extensive research has been conducted to address these ongoing challenges in the development of process parameters namely, laser power, scanning speed, powder flow rate and gas flow rate (Yeh *et al*., 2004; Otto *et al*., 2013; Chikumba *et al*., 2015). However, there is still a need for substantial improvement in the surface texture and integrity of AM products. This need has stimulated interest among researchers (Rodriguez *et al*., 2020). The AM powder-based layer-by-layer deposition process often results in a notable increase in the surface roughness quality which usually ranges from 5-20 µm (Guo *et al*., 2018; Strano *et al*., 2013). The standard acceptable Ra tolerance ranges from 0,8-1,6 µm, this is commonly found in industries where precision and high-quality finish is crucial (Blanco *et al*., 2020). Some examples of industries that require high tolerances include the aerospace, automotive and medical devices (Strano *et al*., 2013; Guo *et al*., 2018).

Surface roughness is the result of AM being an interconnected procedure. It is therefore, difficult to achieve a good surface quality when producing alloys using AM. The challenge with poor surface finish in AM components is that it can affect the mechanical properties, corrosion, and fatigue life of a component. Conventional alloys such as Ni-based alloys have been widely used in high-temperature applications because of their ability to possess superior oxidation resistance properties at elevated temperatures (Parimin *et al*., 2022).

Parimin *et al*. (2022) reported that 800H Ni-based alloy is heat resistant where during high-temperature oxidation the formation of Cr_2O_3 oxide scales forms as a protective layer. However, in recent years, HEAs have garnered significant attention due to their enhanced oxidation performance at elevated temperatures. Lu *et al*., (2021) studied the oxidation behaviour of AlCoCrFeNi-HEA at 1100◦C. The investigation revealed that the HEA demonstrated exceptional resistance to oxidation, forming protective scales with a low oxidation rate. This characteristic suggests that HEAs possess the ability to improve both performance and durability in high-temperature applications. Lu *et al*. (2021) and Parimin *et al*. (2022) research serves to highlight

the promising prospects of HEAs, where HEAs serves as an effective overlay coating that exhibit remarkable resistance to oxidation.

1.7 Hypothesis

Two hypotheses are addressed in this investigation:

1. Post processing

   It is expected that the process parameters of the laser-deposited AlCoCrCuFeNi-HEA will yield dense samples with optimum mechanical properties. Furthermore, post-processing treatment will achieve reduced surface roughness, thus producing industrial-acceptable outputs.

2. Oxidation performance

   The varying of scan speed and laser power will have an influence on the high-temperature oxidation properties of DED AlCoCrCuFeNi-HEA, potentially forming protective oxide scales and inducing oxidation resistance alloy.

1.8 Significance of this study

The significance of this study resides in its potential to introduce improved material and production processes that will have a substantial impact in the aerospace industry that leads to ground-breaking advances. Thereby, providing an improved performance and limiting the high-cost fabrication and maintenance of existing parts.

1.9 Outline of the dissertation

Chapter 1 focuses on the process development, post-manufacturing methods and high-temperature oxidation performance of AlCoCrCuFeNi-HEA. The aim, objective, research objective, research question, delineation, research problem, hypothesis statement and the significance of the study are highlighted in this chapter.

Chapter 2 presents a comprehensive literature review on the additively manufactured processes, the high entropy alloy concepts, different post-processing methods and the high-temperature oxidation process.

Chapter 3 provides details of the methodologies that were carried out and implemented to address the research aim and objectives.

Chapter 4 presents the results obtained from the implemented methodologies. Results include the characterisation of powders, effect of process parameters on microstructural, mechanical, surface properties, and oxidation of HEAs.

Chapter 5 summarised the findings in Chapter 4 and highlights recommendations for future work.

Chapter 2
Literature review

This chapter provides a thorough examination of existing literature, presenting a complete analysis of several significant subjects. The topics encompass a comprehensive assessment of additive manufactured processes, an exploration of high entropy alloy concepts, an analysis of various post-processing procedures, and high-temperature oxidation.

2.1 Additive Manufacturing Technology

Additive manufacturing (AM) or '3D printing', is a manufacturing technology that uses a layer-by-layer process to produce a desired component, the parts are built in a layer-by-layer technique using three-dimension (3D) computer-aided design 'CAD' (Abdulhameed *et al*., 2019). According to the American Society for Testing (ASTM), AM is a layer-by-layer technology used as an alternative to subtractive approaches that extract material using abrasive methods (Frazier, 2014). A step-by-step AM process illustration is shown in **Figure 2.1**.

The process starts with the desired object being digitalised in CAD software. The CAD model is converted from an STL file to tessellate the 3D shape and slice it into digital layers, with set parameters loaded the printer builds (near) net shaped object (Zhai *et al.*, 2014). The fabrication of the object can be achieved by employing various printing materials, including plastic filaments, liquid resin, powders, and paper. AM processes have been used in industries such as aerospace, automotive, and medical centers (Hassen *et al*., 2020).

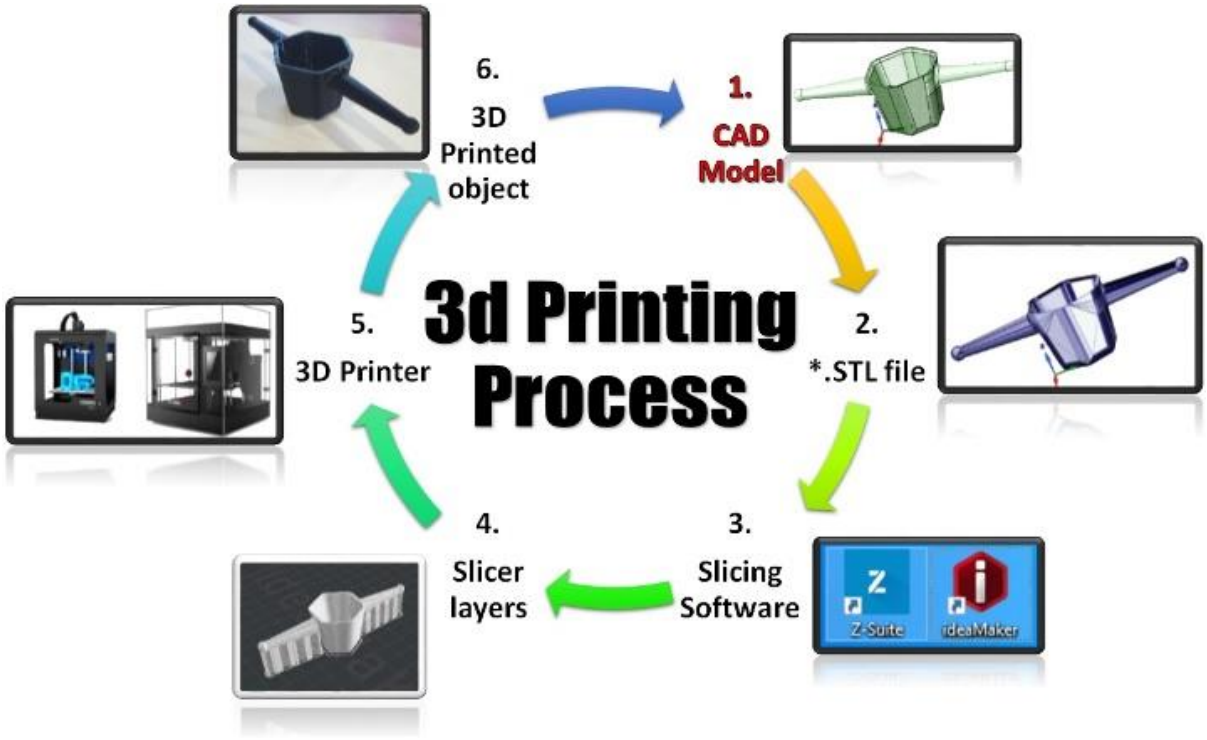


Figure 2.1: Additive manufacturing process illustration (ReCreate3D Printing)

2.1.1 Additive Manufacturing Applications

The adoption of AM has been widely observed across various industries due to its ability to facilitate the efficient fabrication of intricate components with superior structural integrity and integrated designs. This technology enables the production of lightweight parts by utilising minimal raw materials. (Najmon *et al.*, 2019). There is a constant need for the development of structural components that possess specific characteristics, such as being lightweight and cost-effective (Sreehitha, 2017). AM has achieved remarkable results in bringing these requirements to life.

In the biomedical industry, the AM facilitates the development of plastic and resin models for commercial enterprises such as orthopaedics, oral application, or facial reconstruction (Debroy *et al*., 2018). In the transportation industry, there are developments underway that could withstand tough environments such as heat and speed (Mehta *et al*., 2012). Where the development of

advance materials, such as carbon composites, heat-resistant alloys, and specific coatings, are facilitating the enhancement of vehicles and infrastructure's ability to endure high temperatures whilst upholding their structural integrity (Blakey-Milner *et al*., 2021a).

In the aerospace industry, the fuel nozzle in the engine was produced using AM. The nozzle was found to be 25% lighter and five times more durable than its counterpart produced using casting methods (Hassen *et al*., 2020). Military aircraft and space vehicles are some examples of components that are developing in their AM structural components (Kobryn *et al*., 2006). The U.S. Defence Advance Research Project Agency (DARPA) located in Arlington, VA, is conducting a project which aims to use mathematical and computational analogues to produce AM parts with improved complexity of design (Crouse, 2021).

The AM technology has brought digital flexibility and efficiency to manufacturing operations. The ability of the technology to produce complex parts in a one-step process has shown outstanding advantages namely; the ability to produce cost-efficient and carbon footprint reduction results that cannot be achieved by traditional techniques such as subtractive manufacturing and formative manufacturing (Serres *et al*., 2011; Conner *et al*., 2014; Nalli *et al*., 2020).

For example, it has been estimated that $2.5 million could be saved in fuel costs when there is a 50-80% AM metal weight reduction on an aircraft (Zhai *et al*., 2014). Lighter planes with low fuel consumption are a paramount factor in the aerospace industry (Mazumder, 2017) because the industry requires cheaper, faster and safer air travel. The research conducted by Serres *et al.* (2011) examined the environmental consequences associated with AM techniques. The research findings provided evidence that the utilisation of AM technology resulted in a significant reduction of 70% in the overall environmental impact when compared to conventional manufacturing techniques, suggesting that the integration of AM fosters a more environmentally manufacturing practise.

There has been a consistent demand for AM parts yearly in industries such as aerospace, biomedical, defence, automotive, and many more. The use of AM in different sectors is shown in

Figure 2.2. The electronics are the leading sector that is using AM, followed by the automotive industry.

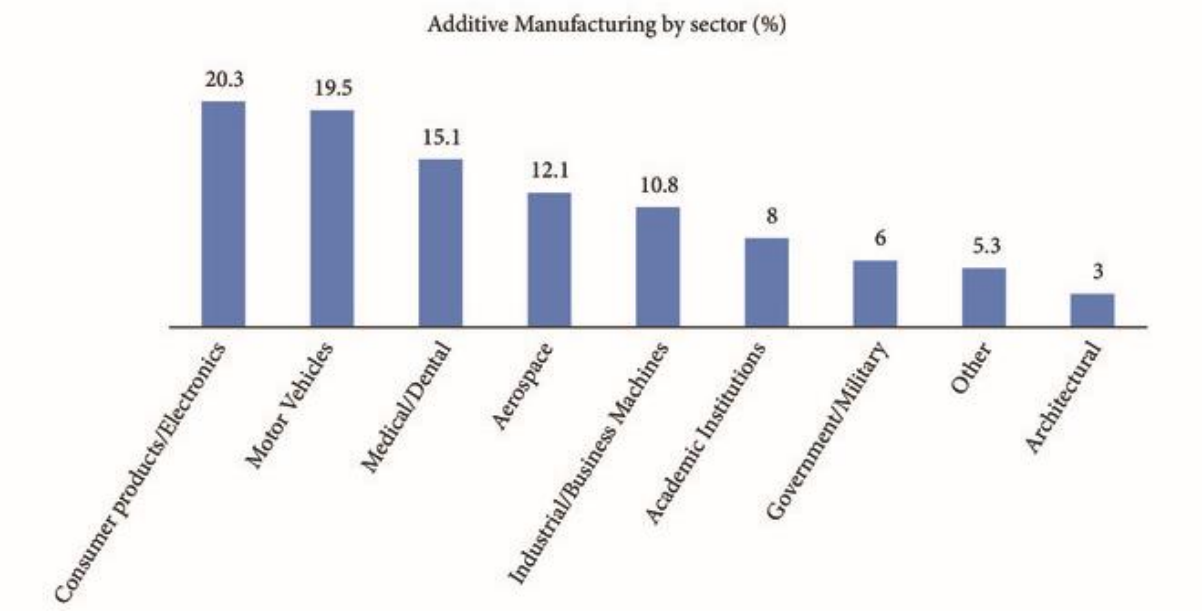


Figure 2.2: Additive manufacturing industrial role in different sectors (Singh *et al.*, 2020).

Campbell *et al.* (2018) reported that 1768 AM metals were sold in the year 2017 alone. This is an 80% increase from the previous year, when the amount was 983 AM metals. Powder-based AM outputs are typically metals or alloys that are used for industrial applications, therefore, factors such as cycle time and product cost are of essence to remain competitive (Mazumder, 2017). Puma-Araujo *et al.* (2016) reported that AM has an 80% reduction in the manufacturing time of multi-layered printed circuit board in the electronic industry.

The AM technology further promotes the production of a customised metal component and enhances the possibility of more complex features without drastically increasing the costs. Although AM offers various advantages, it also comes with limitations, including the potential for porosity, cracks, surface irregularities, and reduced surface quality during production. (Aboulkhair *et al.*, 2019). Through the comparative analysis of current literature on AM applications and conventional alloys, this study aims to enhance the scholarly comprehension of the implications

and advantages associated with the implementation of the AlCoCrCuFeNi-HEA alloy using DED technique.

2.2 Laser deposition process

Additive manufacturing can be classified into three main categories according to the feedstock material used (i.e. liquid-based, solid-based, and powder-based). **Figure 2.3** shows the different classifications of AM processes. This research focuses on the Laser-based additive manufacturing (LBAM) technique using a powder-based deposition method to produce metal samples.

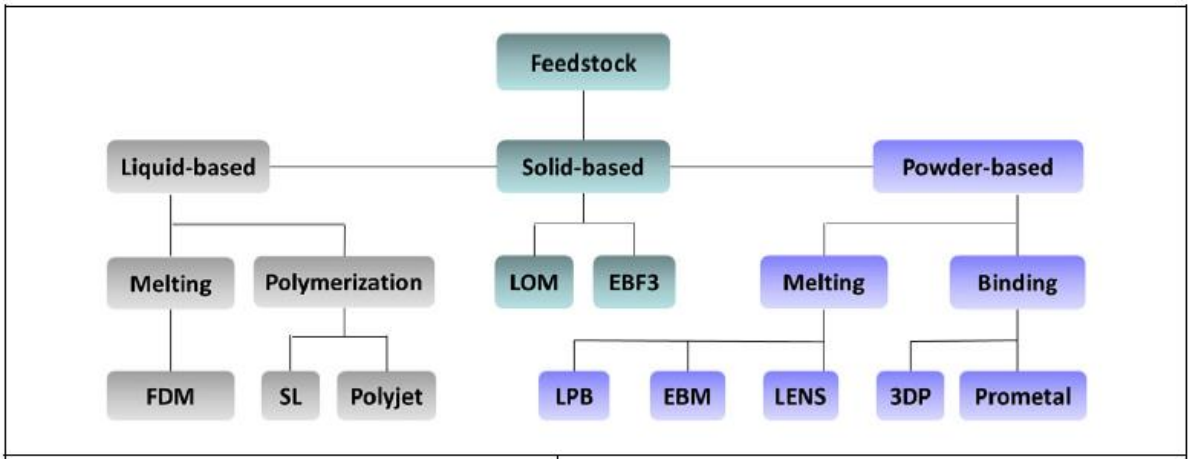


Figure 2.3: Classification of AM categories (Wong, Hernandez, 2012).

The LBAM is divided into wire feed system (wire-laser additive manufacturing (WLAM)), powder bed fusion system (selective laser melting (SLM)), powder blown system (direct metal deposition (DMD) and laser engineering net shaping (LENS)), and as shown in **Figure 2.4** (Thompson *et al*., 2015; Dobbelstein *et al*., 2018; Zhou *et al*., 2019).

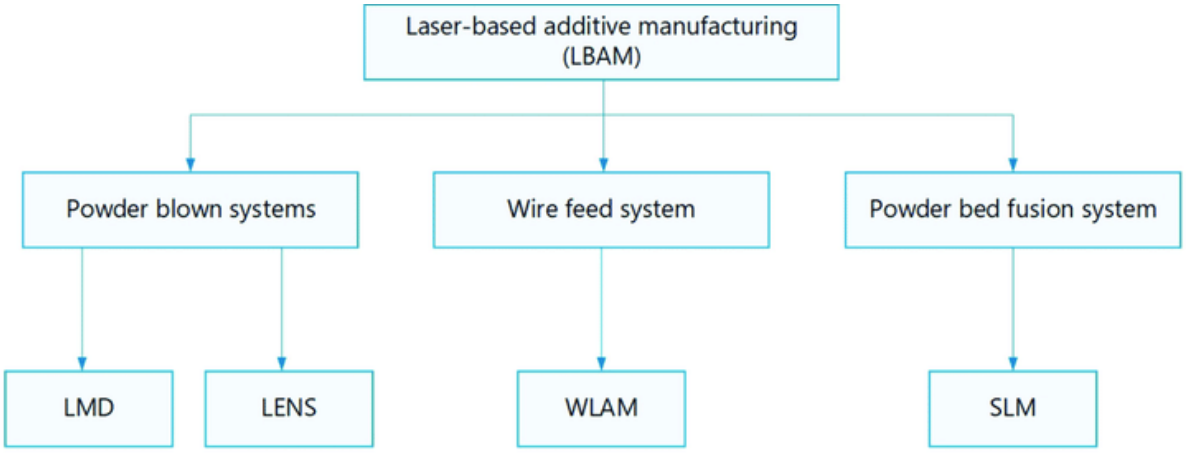


Figure 2.4: LBAM manufacturing process divided into three categories (Thompson et al., 2015).

2.2.1 Wire feed system

The wire feed additive manufacturing uses solid wire feedstock to fabricate components instead of powders. Electron beams are used as a heat source in a high vacuum environment (Zhai *et al*., 2014). A metallurgical bond is formed by the melting of the wire into a melt pool onto a substrate (Heralic, 2012). The framework branches into the following techniques; electron beam freeform fabrication (EBF^3), wire laser additive manufacturing (WLAM), wire and arc additive manufacturing (WAAM) (Karunakaran *et al*., 2010; Ding *et al*., 2015).

The wire feed AM system is beneficial due to large component production with moderate complexity such as stiffened panels. The production process is not hazardous to the operator because of the non-use of powder and the deposition rate is higher than that of a powder-based process (Ding *et al*., 2015; Gateway, 2016). The wire feed process has several limitations in the sample production, these limitations include a loss of tolerances, the potential for a staircase effect in samples, distortion caused by excessive heat input, and the production of poor surfaces (Ding *et al*., 2015; Gateway, 2016).

2.2.2 Powder-bed fusion

Powder-based fusion system consists of a vacuum building compartment (printer), a powder chamber in the company of a coating roller used for spreading the powder across the stage, a delivery piston, and a fabrication piston (Zhai *et al*., 2014; Murr, 2015). The compartment is filled with inert gas to protect the molten material from corrosion (King *et al.*, 2015). The PBF is either fused with an electron, thermal, or laser heat source to melt and fuse the material to form a 3D product.

Singh *et al.* (2020) and Zhai *et al.* (2014) provided an explanation of the PBF printing method as follows: Before the fabrication process a powder delivery piston moves up and the fabrication piston moves down a layer so that the powder can be spread and lightly compacted by the roller. The laser beam is then driven over it to melt a particular powder under the guidance of the scanning system. Then the 3D CAD model is converted into an STL file and is loaded into the printer, the powder chamber is filled with powder. A heat source is used to fuse the powder while the coating roller spreads a layer of powder along the platform as per 2D cross-sectional data from the STL file. Then the newly formed powder layer is supplemented upon the previous layer. This process takes place repeatedly until the product is formed.

Examples of laser-fused techniques are Selective Laser Sintering (SLS), Selective Laser Melting (SLM), and Electron Beam Melting (EBM). SLM and EBM qualify for metal fusion and SLS qualifies for plastic fusion (Debroy *et al*., 2018). Attractive characteristics of PBF include low-cost production, a wide range of material choices to choose from, no powder wastage, and no support structures needed during fabrication as powder acts as a support structure (Zhai *et al*., 2014). However, the process is time-consuming and has a history of high porosity, poor surface finish, and high power usage (Kumar and Jain, 2020).

2.2.3 Direct Energy Deposition

Direct Energy Deposition (DED) is an AM process that uses heat input in the form of electron beams, lasers, or plasma arcs, to join materials together (Lee, 2008; Sing *et al*., 2020) According to the ASTM F3187-16, DED is defined as a technique that involves the application of focused thermal energy that is used to fuse material through the process of melting during deposition. The feedstock material used in DED can be either metal powder or wire (Lee, 2008; Sing *et al*., 2020). **Figure 2.5** shows a schematic representation of the DED process.

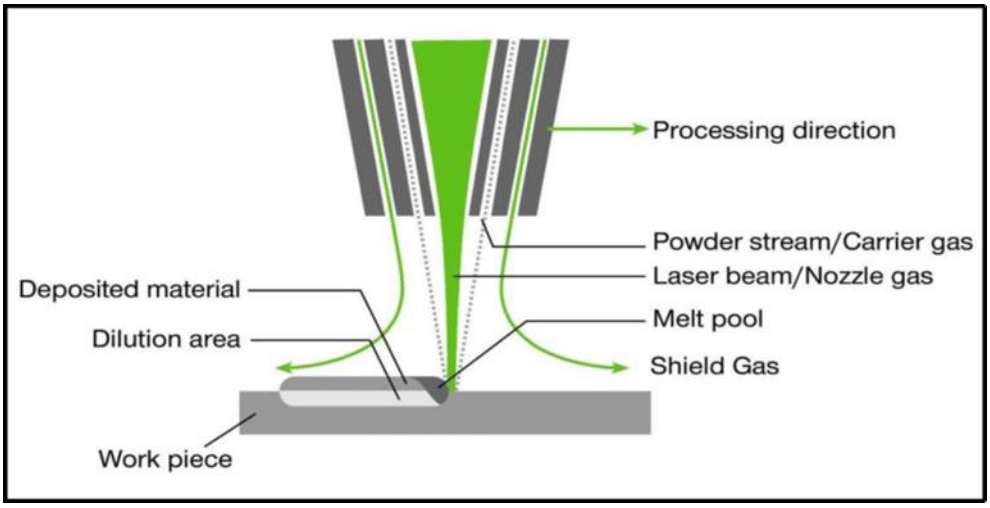


Figure 2.5: Schematic representation of the Direct Energy Deposition (Sibisi *et a*l., 2020)

The system uses the powder delivery nozzle technique where the powder is administered into the laser-induced melt pool either using single or multiple nozzles (Parry *et al*., 2016). Using multiple nozzles allows the prospects of mixing different powders. The robot often contains inert gas blown together with the powder from the nozzle by that shielding the melted region thus reducing the oxidization rate (Gokuldoss *et al*., 2017).

The advantages of DED technique are excellent bonding between the clad and base material, high precisions, large production of parts with high complexity level to improve workflow, parts

containing low porosity, and less penetration of heat on the substrate (Frazier, 2014; Gibson, 2015). Nonetheless, some challenges need to be addressed, specifically in the area of post-processing and the exploration of synthesised characteristics that require further investigation (Gibson, 2015).

The optimisation of process parameters during the DED fabrication technique of metals has significant importance in ensuring that the components meet the standard demands by industries such as aerospace. It enhances the performance of materials, reduces defects, ensures cost efficiency, and enables the customisation of components for specific applications, making it a fundamental process during manufacturing (Blakey-Milner *et al*., 2021b). Mahamood and Akinlabi. (2017) investigated the influence of parameter optimisation on LMD Ti6Al4V. The research highlights the need to determine the optimised process parameter settings to achieve the required product. The authors suggest optimising processing parameters can result in enhanced results with regards to the mechanical properties of components produced using the LMD technique.

Bhardwaj *et al.* (2019) conducted a study to examine the microstructure and mechanical properties of a titanium-molybdenum alloy that is specifically designed for bio-implant applications. The investigation utilised the DED laser AM process. The findings demonstrated a successful deposition procedure characterised by low levels of porosity. DED parts are free from distortion with low porosity in contrast to other AM processing techniques such as PBF and WAAM. The system also allows large quantities of powder usage which requires high energy density thus leading to an accelerated building rate (Yusuf and Gao, 2017).

Dada *et al.* (2020a) optimised AlCoCrFeNiCu and AlCoCrFeNiTi HEAs on the Kuka robot at CSIR National Laser Center under preheating conditions. The alloys showed potential in coating and structural application along with the production of minimal cracked samples. This is due to the alloy's properties exhibiting effective performance, durability, and resistance to cracking. Higher hardness was due to the preheating temperature introduction at the second stage. This is because the preheating process has the potential to impact the internal structure and distribution of stress within a material, resulting in enhanced qualities of hardness (Ding *et al*., 2018). Ding *et al.*

(2018) investigated the effects of preheating the substrate when fabricating $12CrNi_2$ using the DED process. The researchers observed that the use of preheating to the substrate resulted in notable advantages, such as increased sample hardness and enhanced mechanical properties, specifically in terms of tensile stress.

This research focuses on the laser-based DED technique, which involves the use of powder to achieve the melting and bonding process onto a substrate. This study will explore the various aspects and parameters associated with this technique, encompassing the laser power, scanning speed, and powder properties. By investigating these factors, the study acquires more comprehension of the procedure and its potential application, leading to advancements in AM and the development of high-quality, functional components. Furthermore, the study evaluates mechanical properties, microstructural attributes, and operational efficacy of the produced components to evaluate the overall efficiency and dependability of laser-based DED employing powder.

2.3 High entropy alloys

The material research community is constantly yielding towards the development of materials to provide better properties and functions than the ones that are currently being used in industries such as biomedical, aerospace, energy, and manufacturing. This has led to the development of HEAs (Yeh *et al*., 2004, Yeh *et al*., 2007). Yeh *et al.* (2007) have described HEAs as metallic materials that consist of five or more principal elements in equiatomic or close to equiatomic atomic ratios with an atomic percentage between 5 – 35 at.%.

The HEA possesses attractive properties such as a high strength-to-weight ratio, thermal resistance, creep strength, and corrosion resistant (Chikumba and Rao, 2015). Conventional alloys possess limitations concerning specific attributes, such as reduced specific weight and high density. These factors possess adverse ramifications concerning their utilisation within the structural application (Zhao *et al*., 2004; Otto *et al*., 2013). For example, nickel alloys have been used in load-bearing applications for many years because of their ability to withstand high temperatures up to 1100˚C. However, these alloys have high densities which are unable to satisfy

the load-bearing requirement (Zhao *et al*., 2004; Chikumba and Rao, 2015). HEAs are potential substitute for nickel alloys in load-bearing applications owing to its capacity to provide high-temperature performance, decreased weight, enhanced mechanical qualities, and resistance to corrosion. These advantages provide HEAs as the potential option for a wide range of load-bearing applications in which conventional nickel alloys may experience limitations (Dewangan *et al*., 2022a). Dada *et al* (2021b) conducted an analysis of the microstructural and corrosion behaviour of AlCoCrFeNiCu and AlCoCrFeNiTi. The study revealed that even though Ti-based HEA displayed high corrosion resistance to Cu-based HEA, the resistance of both alloys was higher than that of traditional alloys.

Given that there are multiple elements present in the alloy one would assume it may be postulated that it embodies a formula conducive to possible challenges. However, the outcomes has left researchers astounded and this is due to the four core effects explained by Tsai and Yeh, (2014) and Gačnik. (2017) as the high-entropy effect, sluggish diffusion, severe lattice distortion, and cocktail effect. It is crucial to note that the fundamental consequences of the four core effects have a significant influence on the strength and ductility of phases, which is mainly due to solution hardening (Dewangan *et al*., 2022b). The four-core effect is briefly explained in **Section 2.3.1.**

2.3.1 The four-core effect

High-Entropy Effect forms few phases due to higher mixing entropy. It is responsible for lowering the free energy of solid solution phases and facilitates their formation at higher temperatures (Tsai and Yeh, 2014), thus favouring the formation of simple solid solutions such as face-centered cubic cell (FCC), body-centered cubic cell (BCC), and hexagonal closed-pack cell (HCP) (Gačnik, 2017). For instance, melting pure metal is due to the higher entropy of the liquid state relative to the solid-state, according to Richard's rule (Tsai and Yeh, 2014).

Figure 2.6 illustrates the X-ray Diffraction (XRD) spectra formation of simple structures established from binary, ternary, quaternion, quinary, senary, and septenary alloys. **Figure 2.6**

displays BCC and FCC phases; with negligible intermetallic phase on the septenary alloy (Tsai and Yeh, 2014).

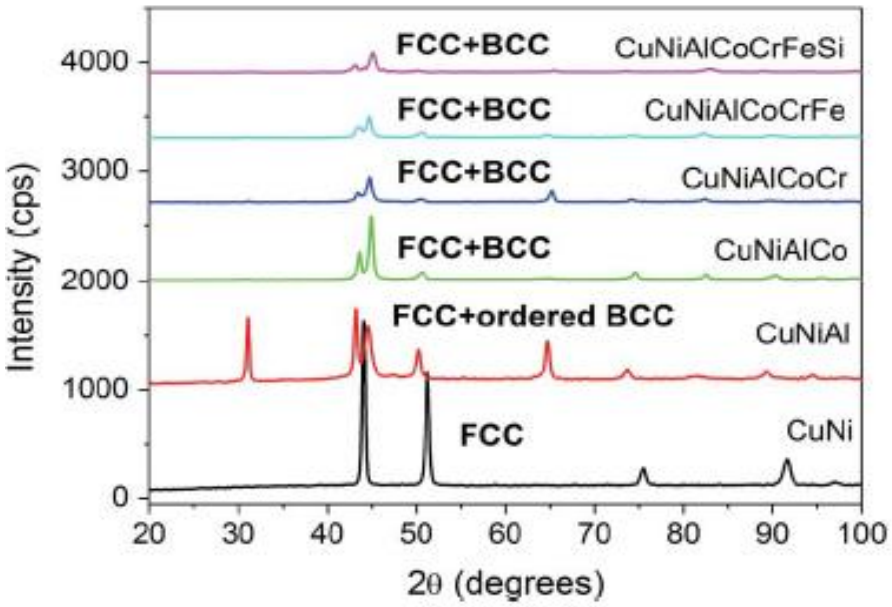


Figure 2.6: XRD patterns of the addition of elements in the series of alloys (Tsai and Yeh, 2014).

The number of phases that can be stabilized at high temperatures is given by Gibbs free energy in **Equation 2.1**:

$$G = H - T S \qquad \textbf{(2.1)}$$

Where G [kJ] is the Gibbs free energy, H [kJ]is the enthalpy, T [K]is the temperature, and S [J/K] entropy of the system (Tsai and Yeh, 2014). Gibbs free energy is the calculation of energy that can do work performed by a thermodynamic system at constant temperature and pressure (Gačnik, 2017).

Lattice Distortion Effect: HEAs are composed of multi-elements. These elements could be of different sizes which can lead to the distortion of the lattice (Gačnik, 2017). Larger elements take up space so much that they end up pushing neighbouring elements and causing compression to the lattice. The small elements have extra space around and it causes tension in the lattice thus inducing the stress-strain domain. **Figure 2.7** demonstrates this phenomenon (Gačnik, 2017, Tsai and Yeh, 2014).

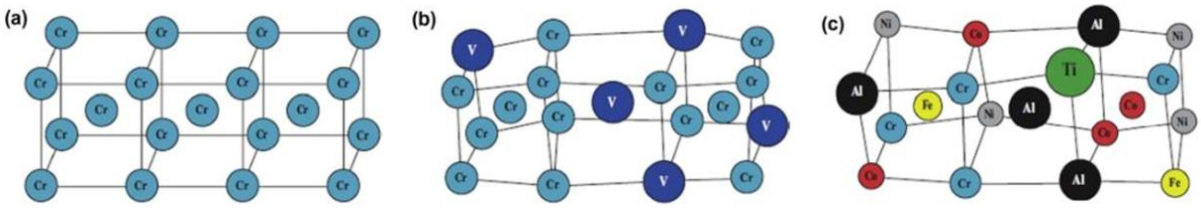


Figure 2.7: BCC lattice that contains a) Cr b) Cr and V c) Cr, Ni, Fe, Co, Al, Ti (Gačnik, 2017).

Figure 2.7 represents a multi-element BCC lattice structure with different atomic size elements a) contains Cr, the lattice is not distorted because it contains a single element, b) and c) contain Cr, V, and Cr, Ni, Fe, Co, Al, and Ti respectively at different atomic sizes. The stress-strain effect is present due to the element's different sizes and the effects of different bonds between them. Stronger bonds lean towards smaller bonding distances thus the lattice increase leads to an increase in free energy (Gačnik, 2017).

Sluggish Diffusion Effect: The face transformation kinetics and diffusion in HEAs are very slow than those in their conventional counterparts (Cheng *et al*., 2006). This is due to two points: firstly, the surrounding of atoms changes with movement subsequently leading to different bonding and therefore different local potential. An atom would be trapped when jumping into a state with a low-energy site because the chance of jumping out is low. Whereas jumping into a high-energy site gives a high chance of jumping back to the original site (Tsai and Yeh, 2014). A seven-bound model was used to illustrate the local energy fluctuation on diffusion shown in **Figure 2.8**.

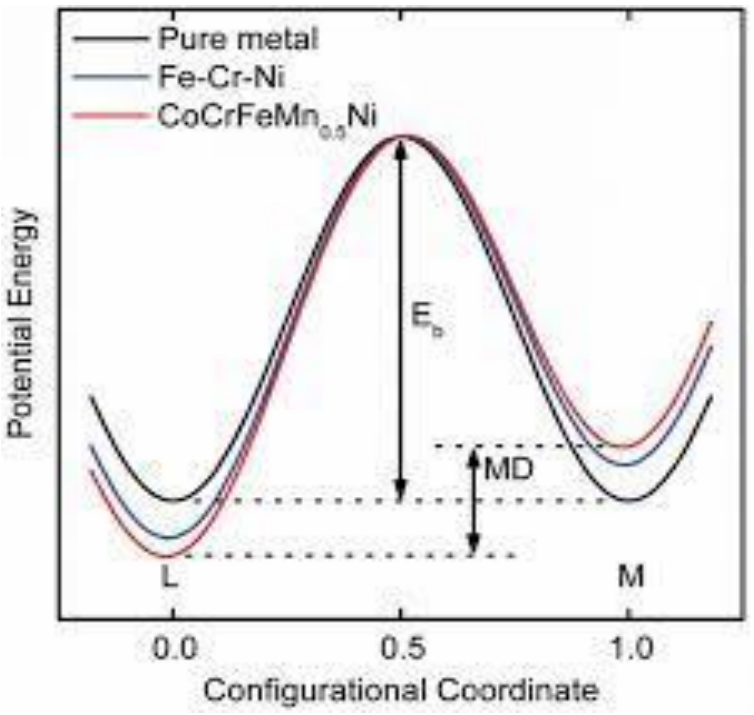


Figure 2.8: Potential energy changes when the Ni atom migrates (Tsai *et al*., 2013).

When Ni atoms diffuse in Co-Cr-Fe-Mn-Ni alloy the mean potential energy difference between the lattice site becomes 60.3 meV which is 50% higher than Fe-Cr-Ni alloy. This difference drives the atoms to occupy the low-energy level longer. The diagram represents a lattice potential energy as a function of the distance between the two lattice sites for pure metal, $CoCrFeMn_{0.5}Ni$ and Fe-Cr-Ni where L is the position of the initial atoms and M is the position of the final atoms. Pure metal's potential energy will remain the same through atomic migration. Secondly, the HEA rate of diffusion differs with each element; some elements are less active and have lower potential energy. For phase transformation to occur there ought to be movement amongst the elements hence the slow movement of elements that affects the diffusion process (Tsai *et al*., 2013).

Cocktail Effect: HEAs are considered as a composite because it contain different elements thus there is a higher property contribution than expected by the rule of mixture between the interaction of the elements (Costas, 2018). The properties of HEAs come from the interaction between the elements and lattice distortion (Yeh, 2016, Tsai and Yeh, 2014). For instance, the addition of light

elements such as Al decreases the density of an alloy. However, the addition of Al could lead to the hardening of the alloy. **Figure 2.9** illustrates the hardness of $Al_xCoCrCuFeNi$ alloy when Al is added to the alloy. The graph indicates that an increase in Al content increases the hardness of $Al_xCoCrCuFeNi$ alloy. This is due to hard BCC phases that are formed resulting from the strong cohesive bonding between Al and the other elements along with the large atomic size elements (Tsai and Yeh, 2014).

A brief overview emphasises the significance of comprehending the four-core effects in the characterisation of DED AlCoCrCuFeNi-HEA. The four-core effects play a vital role in determining the characteristics of the material, and understanding their influence is essential for accurately assessing and improving the performance of AlCoCrCuFeNi-HEA. This research investigates the relationship between these effects and the specific attributes of AlCoCrCuFeNi-HEA, thereby enhancing our comprehension of the behaviour of HEAs and their prospective uses.

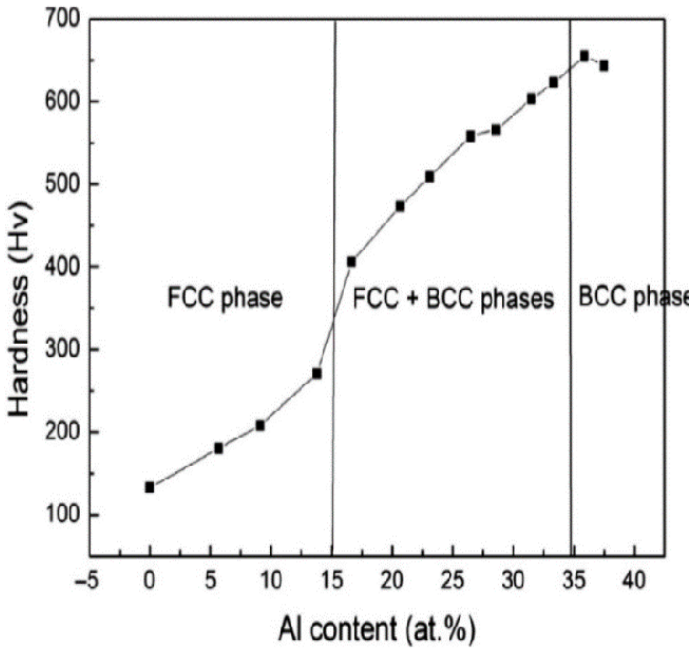


Figure 2.9: The hardness of AlxCoCrCuFeNi alloy as Al content increases (Costas, 2018).

2.3.2 High entropy alloy applications

Presently, studies have been devoted to showcasing the development of HEAs that possess the capability to withstand harsh circumstances such as elevated temperatures and surroundings susceptible to hot corrosion. These alloys are anticipated to not only withstand such environments but also provide remarkable mechanical performance (Dewangan *et al*., 2022b).

In the aerospace industry HEAs are used in high-temperature applications such as turbine engine where high strength, low densities, oxidization, and wear resistance play a pivotal role in the reduction of fuel consumption and surface protection (Chikumba and Rao, 2015). HEAs exhibit considerable potential candidates alternatives to Ti and Fe alloys (Huang, 2009). In the transportation industry, heat and velocity are fundamental components. The industry necessitates the use of materials that can function well under high temperatures, have low densities, and demonstrate exceptional strength. These characteristics possess considerable promise in the context of energy-efficient applications, notably within the transportation and energy sector (Yeh *et al*., 2004; Miracle *et al*., 2014). HEAs favour the desired properties in contrast to traditional alloys such as Al-alloy, which are good candidates for low-density application but they fail to operate in high temperatures (Miracle *et al*., 2014).

Coating parts is a popular application used for protection and novel improvement of conventional materials through modification of functional properties (Li *et al*., 2019). Environmental degradation of the surface subjected to high temperature, abrasion, fatigue, erosion, gas, and hydro-abrasiveness leads to surface wear damage causing a reduction of the service life (Dmitriyev *et al*., 2005). The application of coatings onto the surface of a component can be achieved through various methods and techniques, including thermal spraying, DED, and plasma arc. This process involves the deposition of a significant layer of materials that are specifically designed to provide resistance against corrosion and wear (Glicksman, 2010).

The study aims to investigate and establish potential functional structures and advanced coating materials designed specifically for aerospace applications, particularly in high-temperature conditions such as gas turbine components. By directing attention towards these exceptional

circumstances, it is the objectives of this study to devise solutions that possess the ability to endure high-temperatures and oxidation resistance.

2.4 Post-surface Treatment

The surface roughness that occurs during the process of AM, is commonly associated with the steady accumulation of the layer-by-layer powder deposition, which falls between the Ra range of (5 – 20) µm. This range is insufficient in addressing the requirements set by industrial applications (Wall *et al.*, 2009; Raines *et al*., 2010; Strano *et al*., 2013b). Therefore, a post-processing treatment is required to improve the surface quality of the finished product.

Various post-processing procedures can be utilised to improve the surface quality of a sample fabricated using the DED technique. The methods include shot peening, electrolytic polishing, laser polishing, machining, ultrasonic polishing, chemical polishing (also referred to as electropolishing or EP), sandblasting, and centrifugal barrel finishing (also known as barrel finishing or BF) (Löber *et al*., 2013; Habibzadeh *et al*., 2014, Lyczkowska *et al*., 2014).

Kaynak and Kitay (2019) conducted a study that investigates the effects of post-processing by machining, vibratory finishing, and drag finishing on the surface quality of the AM sample. It was found that machining displayed outstanding results compared to vibratory finishing and drag finishing, obtaining high surface quality. However, there was a noticeable limitation when it came to samples with complex shapes, and the need to fixture the parts after polishing.

2.4.1 Electropolishing

Electropolishing is an electrochemical polishing process that uses anodic dissolution to remove a thin layer of material from a metallic workpiece, reducing the surface roughness by levelling peak-

to-valleys with the aim of surface finish improvement (Han and Fang, 2019). Best Technology Inc. described the polishing process as follows; the workpiece which serves as a positively charged anode connected to a positive polarity of a DC power supply is immersed in a temperature-controlled electrolyte solution. The direction of electric current is from the anode to the cathode, with the anode being connected to the positive polarity and the cathode being connected to the negative polarity. Consequently, a reduction reaction occurs, resulting in the oxidation and dissolution of metal ions present on the surface of the workpiece into the electrolyte, often consisting of acids or alcohols as shown in **Figure 2.10**. Amongst other electrolytes that have been used and produced an improved surface finish on alloys are, a mixture of perchloric acid with alcohol solution, perchloric acid with hydrochloric acid, and lastly, perchloric acid and chromium trioxide (Adelkhani *et al*., 2009, Zaraska *et al*., 2014).

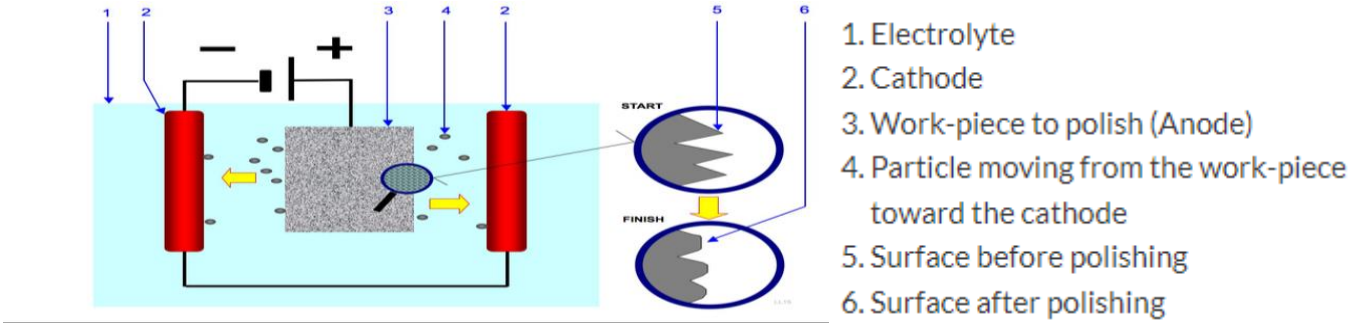


Figure 2.10: An electropolishing diagram with labelling (Han and Fang, 2019).

Advantages of the EP process is that it can polish complex geometric shapes. It is an easy operating non-contact system that is damage-free (Sheasby *et al*., 2001; Han and Fang, 2019). Bahtiar, (2016) conducted a study to investigate the effect of EP on Ti samples using ethylene as the electrolyte. The as-built samples demonstrated a surface roughness measurement of 118.8 nm. A polished surface with a smooth mirror-like finish and a roughness of 5 nm was obtained by subjecting the sample to a voltage of 6 V for a duration of 30 min at a temperature of 20°C. Similarly, applying a voltage of 10 V to the surface for a duration of 30 minutes at a temperature of 20°C resulted in the formation of a smooth and reflective surface, as evidenced by a measured roughness value of 5.7 nm. Urlea and Brailovski (2017) investigated the effect of electropolishing Ti-6Al-4V using perchloric acid (60%) and glacial acetic acid (Fisher Chemical, Certified ACS)

as the electrolyte in a volumetric ratio of 1:9. The results demonstrated a significant enhancement in the surface quality of the Ti-6Al-4V. There was a substantial reduction in the attained surface roughness, with the minimum values observed at Ra = 1 µm and Rz = 4.5 µm. This improvement is significant compared to the initial roughness values of Ra = 112.5 µm and Rz = 56.95 µm, respectively.

Conversely, some chemicals tend to leave an impact on the finished surface. Jiao *et al,* (2019) conducted a study on the corrosion behaviour of Cu-Al-Mn shape memory alloy during electropolishing, the macrographs displayed several pitting on the surface of the alloy. Consequently, the outcome led to a surface that exhibited a deficiency in adequate polishing.

2.4.1.1 Polarization curve study

The current density/voltage diagram also known as a polarization curve shown in **Figure 2.11** is used to determine the potential of the current value flowing through the EP system. The diagram contains four major regions: the etching region, oscillation region, polishing region, and gas evolution region. Region A-B is the area where etching occurs, and grain boundaries are attacked. A passive layer is formed beyond region B and a metal surface is exposed to a newly formed diffusion layer which is important for the polishing phase. Region C-D depicts the designated domain for polishing, with the potential for conducting polishing activities beyond D. However, due to the occurrence of enhanced gas exposure, particularly oxygen, there could be an appearance of "zebra stripes". In some cases, the oxygen occurrence can help remove excess material on the surface (Pircher *et al*., 2003).

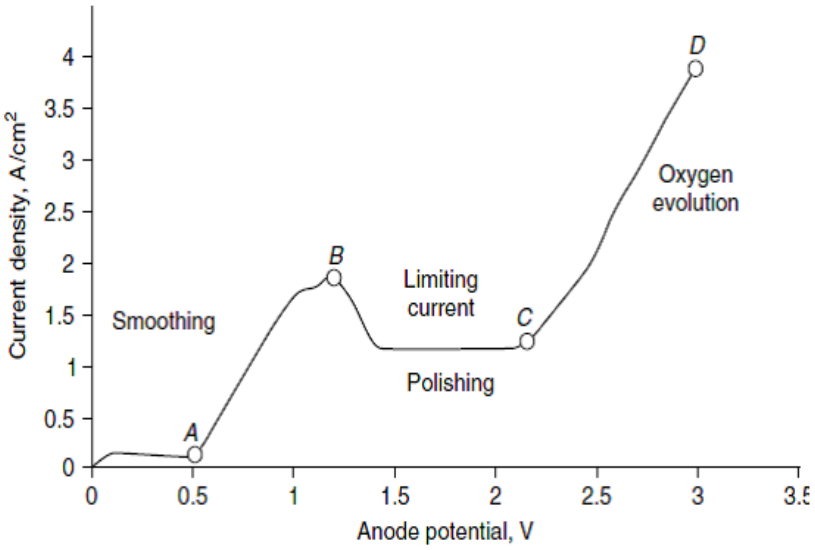


Figure 2.11: Polarization curve used in electropolishing system (Pircher *et al*., 2003).

2.4.2 Centrifugal Barrel Finishing

Barrel finishing is a surface-improving procedure that usually requires media, water, and a polishing liquid. The process is usually performed in an octagonal rotating barrel. The contents in the barrel move upwardly at a predetermined speed by rotation. Thus, the removal of a layer slides down (Boschetto *et al*., 2020). When the process parameters adequately satisfy the motion requirements there is a relative velocity that takes place between the part and the media in the region that is known as the active layer, thus causing the delicate abrasive breakdown of the part surfaces either by rounding of corners, grinding, descaling, deburring, deflashing and polishing (Boschetto *et al*., 2020). The interaction between vertical vibration and rotational motion within the barrel enables the achievement of a polished and seamless surface. As the abrasive particles traverse complex sample regions, they generate abrasion, which enables the deliberate micro-removal of material (Khan *et al*., 2020).

Boschetto *et al.* (2020) conducted a study to analyse the barrel finished samples of additively manufactured Ti6Al4V blades and Inconel718 manifold components. The authors found that an

external surface roughness reduction took place. The initial Ra of the blades was 13 – 14 µm and the final Ra was 2.5 µm corresponding to an 85% reduction in 69 hours.

One of the notable benefits of the BF technique lies in its capacity to generate visually appealing appearance while utilising cost-effective equipment (Pereira, 2019). Khan *et al.* (2020) examined the BF wire arc additive manufactured part and found that the process exhibits great potential in the removal of rust, deburring, and descaling of the surface. De Beer *et al.* (2012) polished low-surface manufactured Alumide® jewellery in a tumbler using abrasive media, obtaining a smooth attractive metallic lustre surface.

Despite the advantages presented by polishing method, there are limitations brought by the CFB method. The technology tends to produce samples that affect the surface quality of the sample thus causing high residual stresses and cracks. Moreover, the operation is skills dependent and labour intensive (Aboulkhai *et al*., 2019).

This research investigates the effects of laser parameters on the surface characteristics of the AlCoCrCuFeN-HEA, both before and after surface treatment. Moreover, the objective of the research was to improve the post-surface finish of the as-built samples using two distinct techniques: centrifugal barrel finishing and electropolishing. The investigation of these methodologies was undertaken to enhance the surface characteristics and properties of the AlCoCrCuFeN-HEA, with the potential to enhance its performance and suitability across diverse industrial sectors.

2.4.3 Surface roughness measurement

Scanning Probe Microscopy (SPM) is a high-resolution surface reconstruction imaging that uses a physical probe to determine the surface morphology of a sample with a nanoscale tip (Yadhuraj

and Kumari, 2016). SPM includes the following variations: Magnetic Force Microscopy which determines the magnetic measurements, Atomic Force Microscopy (AFM) and Scanning Electron Microscopy which determines the surface morphology, Scanning Thermal Microscopy determines thermal measurements and Scanning Near Field Optical Microscopy for optical measurements (Yadhuraj and Kumari, 2016). SPM has however reported leaning towards an oversight in operation, where the operator may skip the processing of data due to limited knowledge (Maurya and Chauhan, 2011).

The replacement of the physical probe had been successful over the years thus the development of improved novel surface roughness measurement tools such as Gwyddion software. The software allows basic operations outlining precipitations, edge detection, shading, 3D data display, facet levelling, roughness measurement, extraction of profiles, and many more. This makes the software more versatile as it can read 80 different file types for example SPM data, and it is easily integrated into data acquisition (Yadhuraj, Kumari, 2016).

2.5 High-Temperature Oxidation

The surface quality often deteriorates over time due to environmental factors such as oxygen in air, abrasion, and temperature (Huang, 2022). Therefore, in recent years high-temperature oxidation has become the standard performance index in determining the durability, high-temperature oxidation performance, and service life performance of alloys (Sheng *et al*., 2013; Wang *et al*., 2021). High-temperature oxidation is a phenomenon that occurs when metals or alloys are exposed to oxygen gas at high temperatures (Parimin *et al*., 2022). The exposure of metals causes a reaction with oxygen and forms metal oxides thermodynamically. The metal oxides develop and envelope the metal surface. The formation of the oxide scale leads to segregation between the environment and the metal (Parimin *et al*., 2022).

Isothermal oxidation tests investigate the oxide growth of metals during high-temperature exposure. The determination of oxide scales involves the generation of oxide nuclei during

unfolding of the metal at high temperatures. Subsequently, the nuclei undergo a gradual expansion process, ultimately resulting in the formation of a continuous oxide layer. The oxide layer progressively increases until it reaches optimum protection. After a certain thickness of oxide has been attained, the oxidation rate begins to decrease due to the formation of fully developed oxide scales (Parimin and Hamzah, 2020a; Parimin and Hamzah, 2020b).

The influence of high-temperature oxidation greatly affects material selection in modern industry. Numerous industrial activities, such as the generation of electric power using gas turbine, heat-treatment procedures, as well as mineral and metallurgical processing, are carried out at temperatures over 500°C (Gleeson, 2010). Over the years Ni-based alloy has been widely used for high-temperature applications such as power plants, nuclear reactors, and chemical industries due to the oxidation-resistant property it possesses at high temperatures (Cao *et al*., 2017; Xu *et al*., 2018; Jiang *et al*., 2019; Parimin *et al*., 2022;).

The Ti6Al4V alloy is extensively used in various industrial sectors, such as marine, aeronautical, chemical industries, power generation, biomedical devices, sport and entertainment facilities, and transportation, owing to its remarkable combination of high strength-to-weight ratio, exceptional corrosion resistance, and favourable biocompatibility, among other advantageous properties. However, with the limited wear resistance and inadequate high-temperature oxidation resistance pose significant constraints on the practical utilisation of this material in scenarios involving wear and oxidation (Hong *et al*., 2022).

The investigation of high-temperature oxidation in HEAs is of utmost importance owing to their remarkable properties that exceed those of conventional alloys. The AlCoCrFeNi-HEA has attracted considerable interest due to its exceptional mechanical properties (Wang *et al*., 2009; Chou *et al*., 2009; Pouraliakbar *et al*., 2021). Niu *et al.* (2019) fabricated AlCoCrFeNi-HEA using the selective laser melting method. The authors found that the alloy is composed of a mixture of soft FCC and hard B2 phases after being exposed to high temperatures. The HEA composition resulted in the production of high strength and good ductility.

Sistla *et al.* (2015) fabricated AlFeCoCrNi-HEA using the direct metal deposition method. The exposure at high temperatures led to the formation of σ phase transition with improved mechanical properties. The microstructure and high-temperature oxidation of AlCoCrFeNi-HEA were investigated by (Butler and Weaver, 2016) The oxidation process of AlCoCrFeNi-HEA was conducted at a temperature of 1050°C in air within a tube furnace for 100 hours. The researchers discovered that the process of isothermal oxidation facilitated the development of Cr_2O_3, Al_2O_3, and $NiCr_2O_4$ films, together with a distinct AlN phase. The study showed the ability to selectively oxidize the constituents of compositionally complicated alloys, resulting in the development of protective oxide layers.

Butler *et al*. 2015 investigated the oxidative behaviour of the HEA $Al_2Co_{4.5}Cr_4.5Fe_{4.5}Ni_{4.5}$ and $Al_4Co_5Cr_5Ni_5Si$, at a temperature of 1050°C. It was observed that the weight gain of the alloy exhibited a significant increase. The results suggest that the surface layer predominantly consisted of Cr_2O_3. Furthermore, an inner layer exhibited Al_2O_3, concomitant with the existence of AlN inclusions. This study presented actual evidence supporting the protective features and continuous nature of the resulting layer of HEAs.

In summary, the existing body of research suggests that HEAs exhibit notable resistance to oxidation when subjected to high temperatures, making them a preferable choice for a wide range of applications including jet engines, the nuclear industry, and the oil and gas sectors (Dewangan *et al*., 2022b). In addition, AlFeCoCrNi-HEA possesses the advantage of being able to modulate their efficiency by making alterations in the chemistry of HEAs, a capability that is lacking in conventional alloys. Therefore, this study employed the AlFeCoCrNi-HEA to examine the oxidation behaviour at elevated temperatures, considering different combinations of scan speed and laser power. The research conducted aimed to identify and optimise the ideal scan speed and laser power settings to minimise the occurrence of high-temperature oxidation. The significance of this holds great importance in practical contexts.

2.6 Summary

This section focuses on the fundamental principles of additive manufacturing and the operational procedures employed in the production of high entropy alloys using the direct energy deposition manufacturing process. The introduction of high entropy alloys and their unique qualities that differentiate them from traditional alloys have been discussed. Although additive-manufactured high entropy alloys have appealing characteristics, they do exhibit restrictions in terms of post-processing. The employment of centrifugal barrel finishing and electropolishing techniques additively manufactured high entropy alloys has been examined. Moreover, the investigation into the oxidation behaviour of high entropy alloys at elevated temperatures has been comprehensively explained, utilising knowledge gained from prior scholarly investigations.

Chapter 3
Methodology

This chapter provides a comprehensive analysis of the methods used to address the aims and objectives of the research. This chapter addresses the fabrication, examination, and evaluation of AlCoCrCuFeNi-HEA to acquire knowledge on the properties, composition, structure, and characteristics of the alloy.

3.1 Material

Pre-alloyed high entropy alloy powder prepared via a solid-state alloying process was used to produce alloys that were investigated in this study. The AlCoCrCuFeNi high entropy alloy (HEA) powder has a particle size distribution ranging between 32-140 µm with purity above 99%. The powder was commercially purchased from F.J. Brodmann and Co., L.L.C suppliers and was said to contain 16.6 wt% of Cr, Al, Cu, Co, Ni, and Fe. The samples were fabricated on a Ti-6Al-4V base plate with dimensions of 100 mm × 100 mm × 30 mm.

3.2 Powder analysis

The powder analysis of AlCoCrCuFeNi-HEA was conducted at the Council for Scientific and Industrial Research (CSIR). The analysis of powder in this research adhered to the ASTM B822 standards. Particle size distribution was determined by laser granulometry in Bluewave Micro-tract S3500. The Jeol JSM-6010PLUS/LA Scanning Electron Microscope (SEM) incorporated with the Energy-dispersive X-ray spectroscopy (EDS) was used to analyse the chemical composition of the powder. Shear testing of the powder took place to determine the flowability of the powder using a FT4 device. To achieve accuracy and a thorough comprehension of the material's response to different degrees of stress, the tests were performed three times and involved

a range of normal loads (3, 4, 5, 6, and 7 kPa). This methodology aids in determining consistent shear stress readings and improves the accuracy of the obtained data. Analysing the material's reaction under different levels of stress offers a comprehensive understanding of its behaviour.

3.3 Deposition process

A Kuka robot depicted in **Figure 3.1** with 3kW IPG continuous fibre laser power was used to deposit the AlCoCrFeCuNi-HEA powder, in an argon-controlled system to protect the surface from oxidising. The laser was continuously cooled with a chiller to avoid overheating during the process. A 1.5 bar GTV powder feeder system that uses multi-hoppers was used to control the powder feed rate during processing. The furnace was preheated to 600ºC before samples were deposited on the base plate.

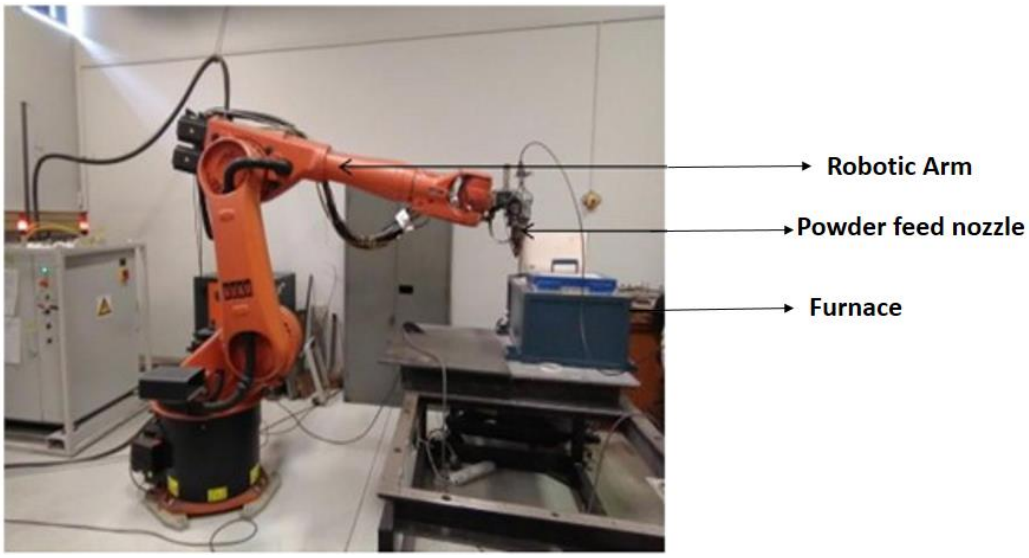


Figure 3.1: 3kW IPG Kuka robot with furnace (Dada *et al.*, 2020b).

3.3.1 Process parameters

The beam diameter of 2 mm and powder feed rate at 2.5 rpm were kept constant while the laser power and scanning speed were varied from 1200 W to 1400 W and 0.48 mm/s to 0.72 mm/s,

respectively. Process parameters that were used in this study are summarised in **Table 3.1**. The technique that was used for cladding is an orthogonal scanning strategy.

Table 3.1: Laser process parameters of AlCoCrCuFeNi-HEA.

Sample name	Laser power (W)	Scan speed (mm/s)	Beam diameter (mm)	Powder feed rate (rpm)
a	1200	0.48	2	2.5
b	1200	0.6	2	2.5
c	1200	0.72	2	2.5
d	1400	0.48	2	2.5
e	1400	0.6	2	2.5
f	1400	0.72	2	2.5

Note: Samples were done in triplicate where sample a = a_1, a_2, a_3

b = b_1, b_2, b_3

c = c_1, c_2, c_3

d = d_1, d_2, d_3

e = e_1, e_2, e_3

f = f_1, f_2, f_3

3.4 Sample preparation

The 25 mm × 25 mm × 15 mm AlCoCrCuFeNi-HEAs samples were built on the Ti-6Al-4V baseplates as shown in **Figure 3.2**. The substrate was sand-blasted and cleaned with acetone before processing and after processing the excess powder on the samples was cleaned using a wire brush.

The samples were wire cut from the baseplate. The samples were cut in half using the struers labotom-5 discom-2 cut-off machine and mounted in a black resin with carbon filler using the AMP50 automatic mounting press. The samples were polished on the struers grinding machine using a SiC paper starting from P 320µm, P 1200µm, and P 4000µm respectively. The samples were polished to achieve a mirror surface finish by using a colloidal silica OP-S suspension for 3 min 30 s.

The polished samples were cleaned with a soap suspension, rinsed, and dried in ethanol for metallographic observations. Marble's reagent which is a mixture of 4 g of copper sulphate, 20 mL of hydrochloric acid and 20 mL of water was used as the etchant to attack the grain boundaries and expose the microstructure.



Figure 3.2: DED samples produced using the KUKA robot.

3.5 Characterisation of as-built and processed samples

Samples were analysed and characterised using density measurement, optical microscope, scanning electron microscope, Energy-dispersive X-ray spectroscopy, and X-Ray diffraction (XRD). Hardness test was conducted to evaluate properties of HEAs produced under varying processing conditions.

3.5.1 Density Measurement

The OHAUS® AX324 analytical balance was used to determine the density measurements of AlCoCrCuFeNi-HEA according to ASTM B962-17.

The density of the samples was measured following the Archimedes principle and **Equation 3.1.**

$$\rho_{measurement} = \frac{m_1}{m_2} \cdot \rho_{OH} \qquad \textbf{(3.1)}$$

Where $\rho_{measurement}$ [g/cm^3] is the measured density of the alloy,

m_1 [g] is the mass of the sample in air,

m_2 [g] is the mass gain of alcohol when the sample is immersed in ethanol and

ρ_{OH} [cm^3] is the density of alcohol.

The theoretical density of AlCoCrCuFeNi-HEA was measured using **Equation 3.2** (Guo, 2022).

$$\rho_{mix} = \frac{\sum_{i=1}^{n} C_i A_i}{\sum_{i=1}^{n} C_i A_i / \rho_i} \qquad \textbf{(3.2)}$$

Where the ρ_{mix} [g/cm^3] is the theoretical density,

C_i is the atomic percentage of element *i*,

A_i is the atomic weight of element *i* and

ρ_i is the density of the element *i*

3.5.2 Optical microscope

The metallographically prepared and etched samples were characterised for microstructural characteristics such as dendritic structures, grain size, and defects using an Olympus BX51M optical microscope (OM). To obtain an overview of the whole samples, microstructural images were taken at various positions using magnifications of 5X, 10X, and 20X. This was guided by ASTM F728-81.

3.5.3 Scanning electron microscope

The Jeol JSM-6010PLUS/LA SEM with EDS was used to analyse the chemical composition and the morphology of the pre-alloyed powder, as-built sample, post processing (electropolishing and centrifugal barrel finishing) and Oxidized samples.

3.5.4 XRD analyses

Phases identification of as-built, post-processed and Oxidized samples were analysed using XRD PANalytical from Tshwane University of Technology. The crystallographic phases were distinguished using a monochromatic Cu (k-alpha) radiation over a scanning range of $20° < 2\theta < 90°$, current of 45 mA, voltage of 40 kV, and the step size of 0.0170°.

3.5.5 Hardness measurement

Microhardness tests were carried out on the surface of the material. The Zwick/ Rowell micro-Vickers hardness tester was employed to quantify the hardness of the specimen, using ASTM E384-22. The current load used was 300g with a dwell time of 10 seconds. For each sample, 25 indentations with 200μm spacing were made on the samples in the vertical direction to the build orientation.

3.6 Post-processing

Two post-processing methods were adopted in this investigation, namely the electropolishing and centrifugal barrel finishing.

3.6.1 Electropolishing

3.6.1.1 Electrochemical analysis

Linear sweep voltammetry (LSV) was performed using a computer-controlled Autolab Potentiostat (PGSTAT302) from Tshwane University of Technology to determine the anodic polarization of AlCrCoCuFeNi-HEA, as depicted in **Figure 3.3**. A three-electrode cell was used to carry out the experimental test to select an electropolishing region using 3.5 wt% NaCl test solution at room temperature. The HEA samples were subjected to a polishing area of 1 cm^2 using a saturated calomel (SCE) and platinum electrodes were used as reference and counter electrode, respectively. Polarization was conducted by varying potential from -10V to 10V at a scan rate of 10 mV/s. To achieve a reproducible measurement, potential was swept in the cathodic direction to avoid pitting of the electrode (Kumar *et al*., 2021).

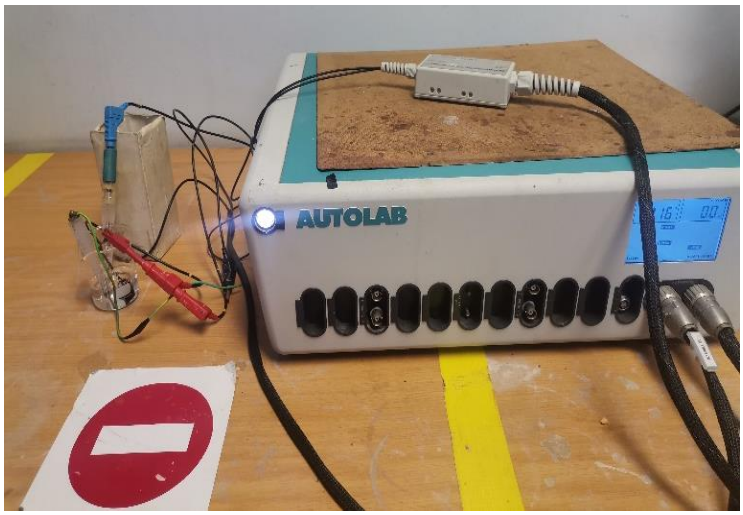


Figure 3.3: Auto-lab Potentiostat (PGSTAT302).

A Struers LectroPol-5 electrolytic polishing and etching device from the University of Pretoria shown in **Figure 3.4** was used to polish AlCoCrCuFeN-HEA samples. The electropolisher comprised of a round opening of 0.5 cm^2. A solution of 80% methanol and 20% perchloric acid was used as the electrolyte. The electrolyte solution was filled into the plastic container of the electropolisher and the experiment was performed at room temperature. The parameters used in this study are shown in **Table 3.2**. After polishing the samples were washed with ethanol and dried.



Figure 3.4: Struers LectroPol-5 electropolishing machine.

Table 3.2: EP optimum process parameters.

Sample	Laser Power (W)	Voltage (V)	Time (sec)	Agitation (rpm)
a_1	1200	-0.5	30	20
b_1	1200	-0.5	30	20
c_1	1200	-0.5	30	20
d_1	1400	-0.5	60	20
e_1	1400	-0.5	60	20
f_1	1400	-0.5	60	20

3.6.2 Centrifugal Barrel Finishing

An industrial barrel finishing machine shown in **Figure 3.5**, CB320-CBF from CSIR at the National Laser Center (NLC), was used in this investigation. The tumbling barrel was loaded with 10 mm × 10 mm angle-cut ceramic, water, and a small amount of LC-13 polishing liquid, all occupying 50 % (11kg) of the barrel volume. Samples a_2, b_2, c_2 were first subjected to ceramic media for 14 hours, and samples d_2, e_2, f_2 were polished with ceramic media for 3 hours, zirconia balls for 2 hours and plastic media for 2 hours as outlined in **Table 3.3.**

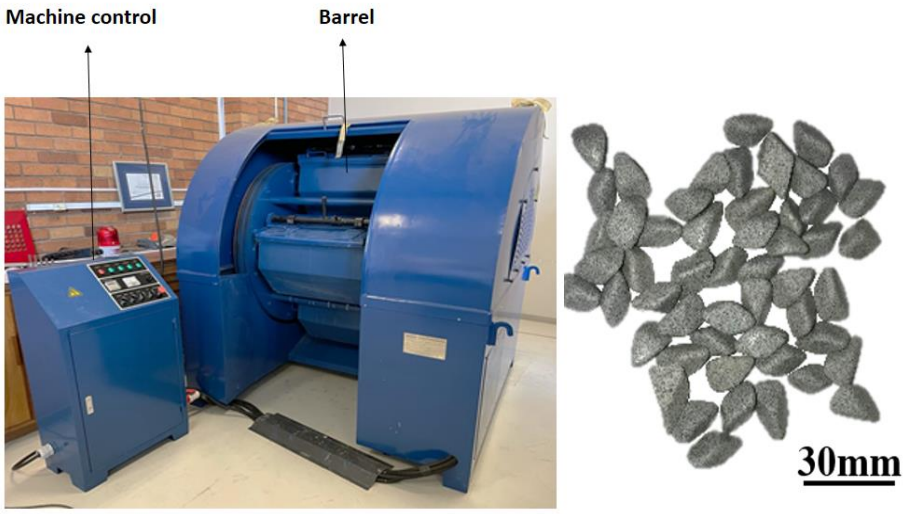


Figure 3.5: CB320-CBF machine and ceramic media used to polish the samples.

Table 3.3: CBF process parameters.

Sample	Laser Power (W)	Rotation speed (rpm)	Time (hrs)
a_2	1200	85	14
b_2	1200	85	14
c_2	1200	85	14
d_2	1400	85	7
e_2	1400	85	7
f_2	1400	85	7

3.6.3 Surface analysis

The surface finish of the untreated and treated samples were measured before and after polishing using a Surtronic® S-100 Series – Surface Roughness Tester. The surface roughness measurements were taken at three different areas on each sample. The surface morphology was examined using a JEOL-JSM-6010/LA plus SEM. A Gwyddion 2.9.32 software used the SEM images to determine the topography and roughness profile of the samples.

3.7 High temperature oxidation

High-temperature oxidation tests were conducted inside an ULTRA-FURN furnace. Six samples that were produced under varying laser and scanning speed conditions were placed in a pre-heated furnace in static air at a temperature of 1000ºC for 100 hrs. Prior to oxidation testing the samples surfaces were polished using 1200-grid SiC paper on all sides and weighed on the analytical balance explorer™ semi-micro OUAUS® weighing mass balance. After 100 hrs the samples were removed from the furnace and cooled down to room temperature. Oxidized samples were weighed on the OUAUS® weighing mass balance. The morphology and phases of the oxide scale was characterised by SEM and XRD, respectively.

3.8 Conclusion

This chapter presents a detailed experimental procedure for AlCoCrCuFeNi-HEA fabrication and characterisation process. Post-processing methods and oxidation tests were described, with the outcomes presented in the next chapter.

Chapter 4
Results and discussion

This chapter presents the results based on the outcome of the methodology obtained in accordance with the research objectives. The evaluation and interpretation of the microstructural and mechanical properties, post-processing and oxidation results obtained from the Laser Direct Energy Deposited AlCrCoCuFeNi-HEA are presented and discussed in this chapter.

4.1 Powder analysis

This section focuses on the examination of powders, comprising a comprehensive look into the chemical composition, morphology, particle size distribution, and powder rheology. This analysis collectively contributes to the characteristics and behaviour of the powder.

4.1.1 Chemical composition

The chemical composition of AlCrCoCuFeNi-HEA powder was determined using SEM with energy dispersive spectroscopy (EDS). **Table 4.1** presents the results of the EDS analysis of the AlCrCoCuFeNi-HEA powder. The analysis revealed a lower weight percentage of Cu and Ni. Additionally, the presence of oxygen in oxide form was observed on the surface of the powder. The chemical composition of the powder as determined by EDS analysis was different from the composition given by the supplier.

Table 4.1: Chemical composition of AlCrCoCuFeNi-HEA powder (wt. %).

	Al	Cr	Co	Cu	Fe	Ni	O
Supplier Composition	16.67	16.67	16.67	16.67	16.67	16.67	16.67
EDS Composition	19.10	15.95	25.16	2.29	33.06	2.61	1.84

4.1.2 Morphology and Particle Size Distribution

The SEM was used to determine the morphology of the as-received AlCrCoCuFeNi high entropy alloy (HEA) powder. The SEM image in **Figure 4.1** shows the as-received AlCrCoCuFeNi-HEA powder, displaying a particle size distribution that ranged from 44-105 μm, with a heterogeneous morphology, as evidenced by the presence of coarse particles in **Figure 4.1**(a). Fine particles in **Figure 4.1**(b), and irregular particle shapes in **Figure 4.1**(c) and (d) were also observed. The powder also contained oxides and satellites on the surface, observed in **Figure 4.1**(a) to (d). **Figure 4.1**(e) to (f) showed particles of varying irregular shapes across all sizes, with a relatively low proportion of spherical particles. The irregularly shaped particles were more pronounced in larger particles.

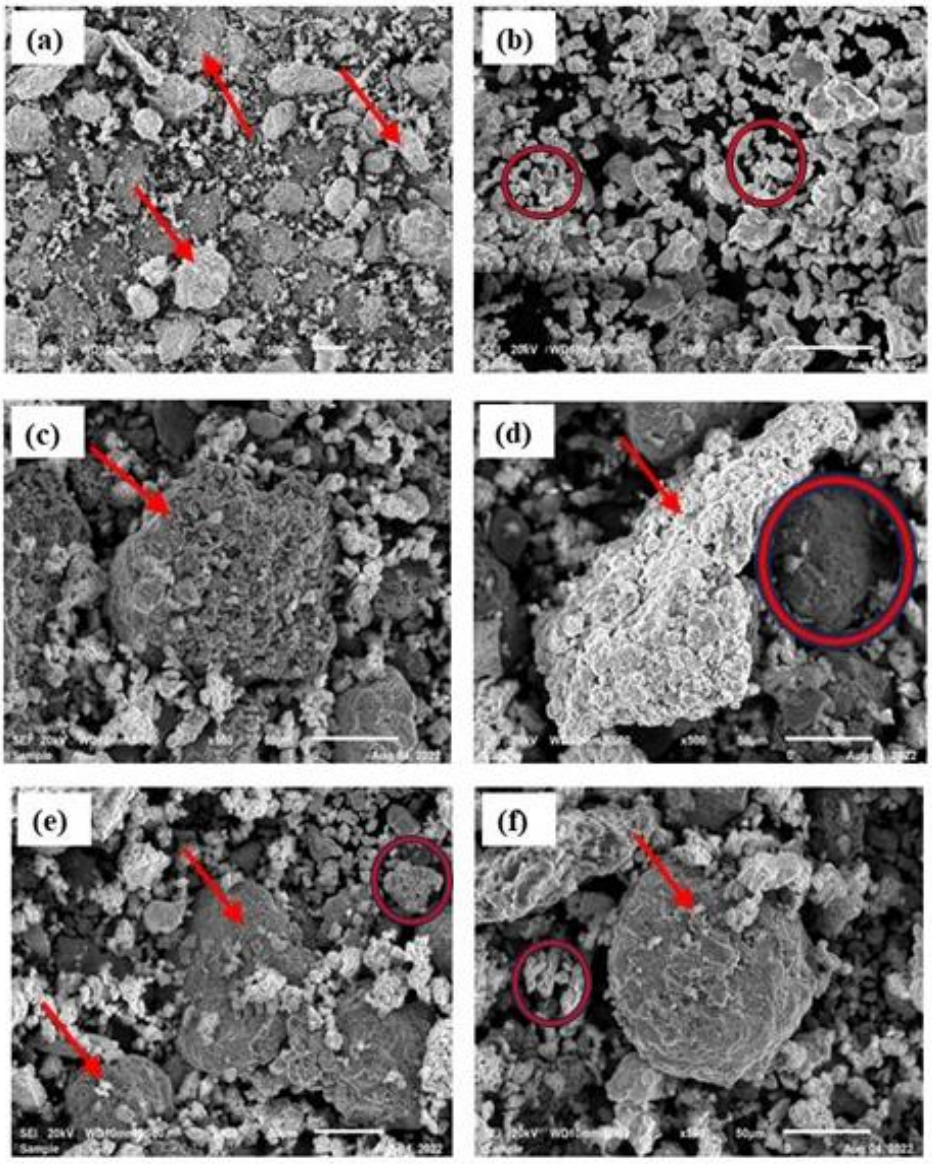


Figure 4.1: SEM micrograph of AlCrCoCuFeNi-HEA powder sample (a) 500×, (b) 500×, (c) 500×, (d) 500×, (e) 500×and (f) 500× at different areas of the same powder.

The AlCrCoCuFeNi-HEA powder was determined by the laser granulometry in the Bluewave Micro-tract. The particle size distribution results are presented in **Tables 4.2**, and graphically illustrated in **Figure 4.2**. The particle size was found to be in the range of 19.36-207.80 μm in percentile 10 and 95, which is different from the 44-105 μm provided by the supplier. According to the results presented in **Table 4.2,** the $d_{50}/d_{10} > 10$ and $d_{90}/d_{10} \leq 19$ this indicated that the particle

size distribution of AlCrCoCuFeNi-HEA powder did not meet the Karapatis criteria (Vock *et al*., 2019, Gelnar *et al*., 2018).

The particle shape and size distribution in the powder-based manufacturing process is an important aspect as it determines the properties of the parts built such as mechanical strength, and surface finish (Tshabalala *et al*., 2018). Meeting the criteria fulfils the condition of space-filling in between coarse particles by fine grains to form an effective layer (Nziu *et al*., 2014). Fine particles are prone to agglomeration while larger particles are the source of rough surfaces (Machio *et al*., 2018).

Table 4.2: Characteristics values for the particle size distribution.

Metal powder	**d_{10} (µm)**	**d_{50} (µm)**	**d_{90} (µm)**	**d_{50}/d_{10}**	**d_{90}/d_{10}**
AlCrCoCuFeNi	100.0	98.99	97.98	0.9899	0.9798

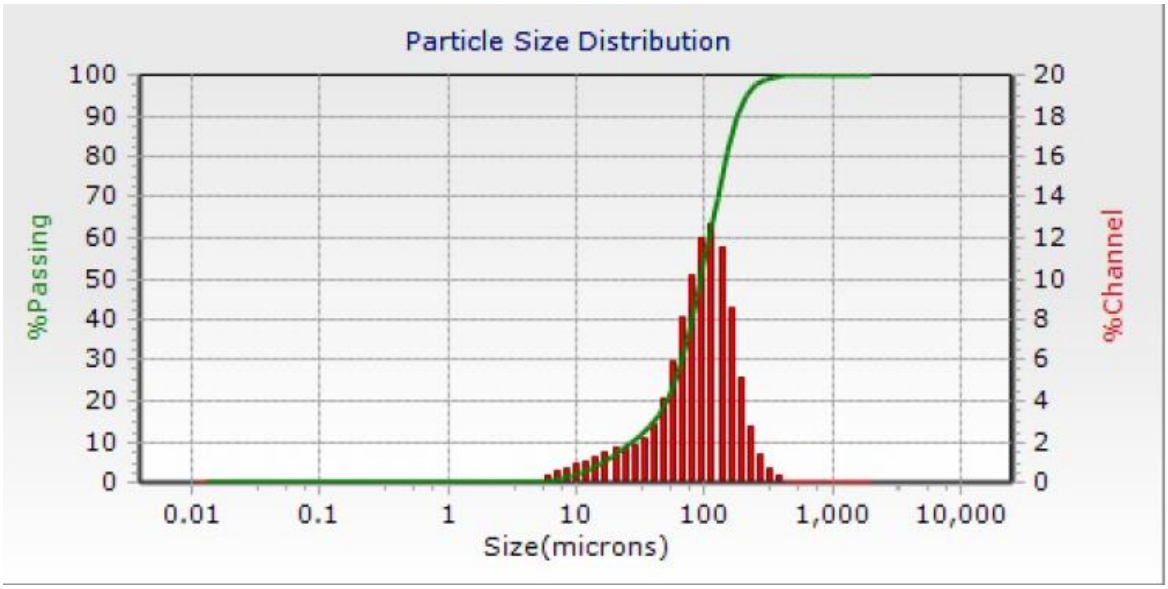


Figure 4.2: Particle size distribution of AlCrCoCuFeNi-HEA powder.

4.1.3 Powder rheology

The powder flow properties of the as-received powder was measured to evaluate if the powder possessed the required properties for building parts using AM technique. **Figure 4.3** constitutes the powder yield locus schematic diagram of AlCrCoCuFeNi powder where **Table 4.3** represents the linear angle of internal friction of AlCrCoCuFeNi powder. **Figure 4.3** represents the data points plotted in two-dimensional coordinate system with points that are defined by the schematic diagram of powder yield locus containing: major principal stress (MPS), unconfined yield strength (UYS), effective angle of internal fraction (AIF), cohesion, flow function (FF), minor consolidation stress (MCS), bulk density (BD) and linear angle of internal friction corresponding to the shear stress as presented in **Table 4.3**. The measurements were repeated three times (R01, R02 and R03) for accuracy and repeatability as shown in **Appendix A, Table A1**. The line tangent to the yield locus is the basis of the parameters obtained during the shear test. The data interpretation and analysis were the same as the results that were obtained from the Jenike shear tester (Markusson, 2017; Tshabalala *et al*., 2018). The internal friction angle aligns with the homogenous structural layer alignment of powder particles. Zegzulka *et al*. (2020) found that the ideal bulk formed by spheres corresponds to the 30˚ angle internal friction.

Table 4.3: Shear cell test properties of the AlCrCoCuFeNi-HEA powder.

Powder	**Cohesion (kPa)**	**UYS (kPa)**	**MPS (kPa)**	**MCS (kPa)**	**FF**	**Denisty (ρ)**	**AIF º**	**BD (g/ml)**
R(average)	0.43	1.63	15.33	3.89	11.75	8.67	33.90	2.80

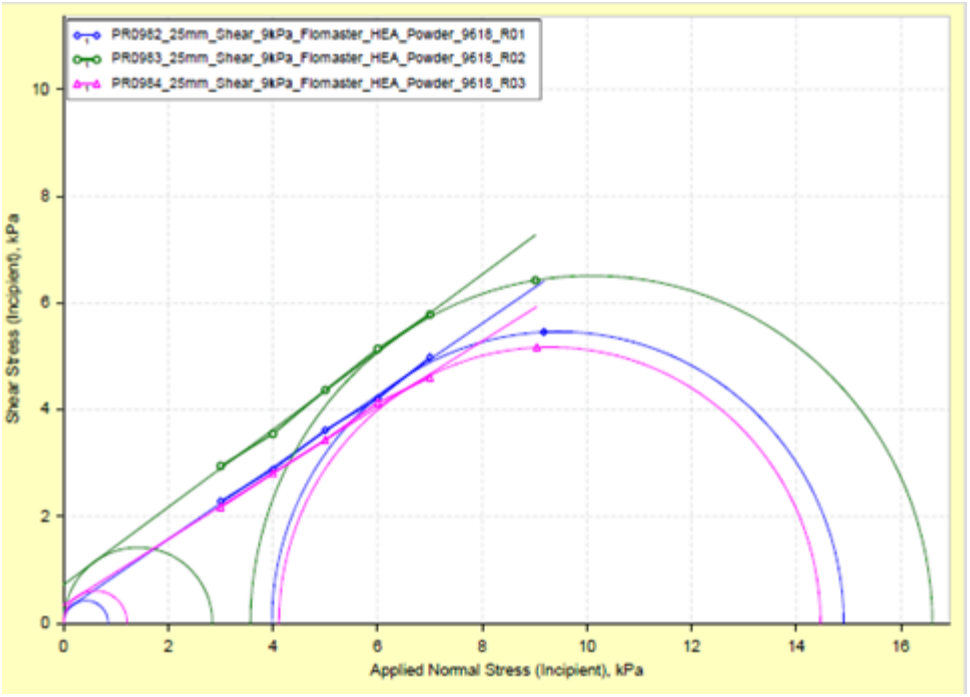


Figure 4.3: Powder yield locus schematic diagram of AlCrCoCuFeNi powder.

Figure 4.4 shows the unconfined yield strength on major principal stresses. **Figure 4.4** conveys an exponential increase, where an increase in total energy increases with the tip speed. Zegzulka *et al.* (2020) found that a high linear slope translates to a flow resistance which indicates a free-flowing powder in accordance with the low value that is close to zero. The internal angle of friction in this study was found to be > 32˚, which is ideal for the flowability of the powder in direct energy deposited (DED) methods. The average UTS value is above 1 kPa, which illustrates that a higher force is needed to make the bulk solids to flow. Tshabalala *et al.* (2018) stated that the flow function (FF) should be greater than 10 for a free-flowing powder. From the results presented in **Table 4.3** the FF factor for the powder was 11.75. Thus, this indicates that the powder would flow.

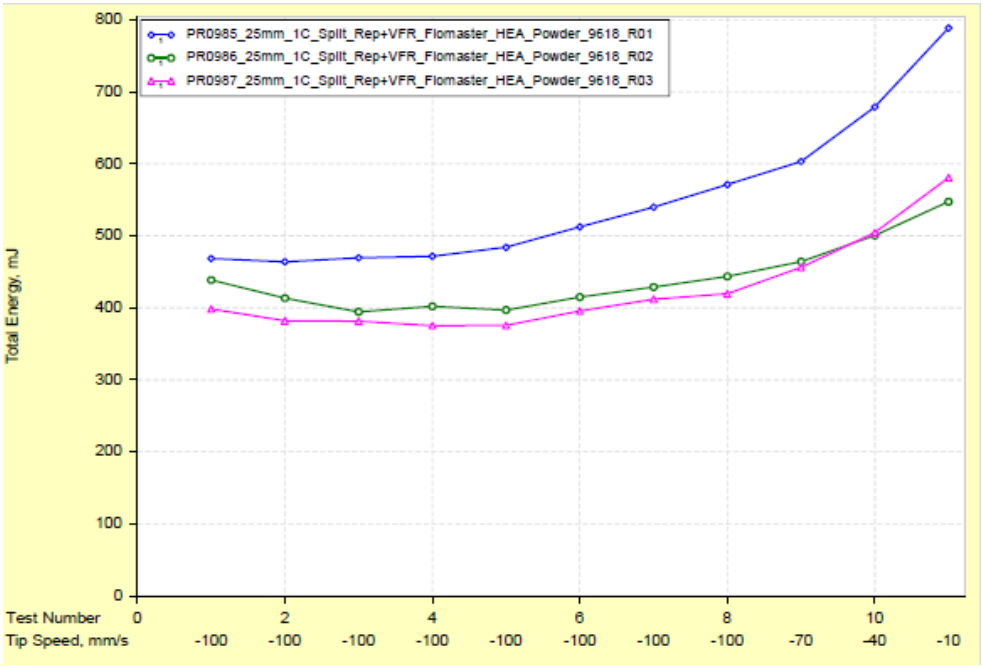


Figure 4.4: Unconfined yield strength on major principal stress.

4.2 Process development of the samples

This study focused on the DED fabrication of 25 mm × 25 mm × 15 mm samples and the laser processing parameters were derived from the optimum parameters obtained from the work that was carried out by Dada *et al*. (2021b). Producing samples presented in **Figure 3.2** of Chapter 3 was challenging. During the fabrication process powder agglomerated in the polyurethane powder feeding tube. This is due to the fine particles sizes that was observed in the powder composition and the particle size distribution which failed to fulfil the Karapatis criteria. The purpose of establishing the criteria is to guarantee optimal powder flowability. The criteria states that the particle size distribution ratio should satisfy $d_{50}/d_{10} \geq 10$ (Karapatis, 2002)

From the results, it was observed that increasing the scan speed and laser power resulted in the formation of irregular layers, causing the samples to have uneven surfaces and rough textures. Spranger *et al*. (2018) experienced challenges during the fabrication of laser-deposited Ti-6Al-4V

cylindrical specimens with multiple tracks overlapping. The authors found that during fabrication, there was a high deposition rate on the edges and a symmetrical built-up in the near areas which caused irregularities in the configuration because of the increasing scanning speed.

In this study, the use of a 15 mm thick baseplate contributed to the formation of unevenness on the surfaces of the samples. Similar challenges are reported by Yu *et al*. (2012). From author's study, it was noted that a 10 mm thick base plate accumulated heat, which resulted in prolonged cooling times, subsequently forming defects on the structure of the samples.

4.2.1 Density using Archimedes Principle

The density of AlCrCoCuFeNi-HEA was determined using the OHAUS® AX324 analytical balance. Each sample was measured three times to increase accuracy. The measured densities are shown in **Appendix B Table B1.** The densities processed at different laser parameters are shown in **Table 4.4**.

The results show that the measured density of AlCrCoCuFeNi-HEA samples increase with increasing scan speed and laser power. Higher scanning speed have an impact on the heat input and solidification rate of the material. Increasing scanning speed at high laser power does not provide enough time for the melting and solidification process to occur. As a result, the density of the material may decrease due to incomplete fusion or insufficient time for the atoms to be organize in the desired manner (Chowdhury *et al*., 2022).

When the laser power increases, the volumetric energy density of AlCrCoCuFeNi-HEA samples increased. As the laser power is increased, a greater amount of energy is delivered into the material, leading to an increase in the ability of the material to absorb energy. Materials that have a higher capacity to absorb laser energy have higher volumetric energy density as the laser power increases

(Liu *et al.,* 2022). However, excessive heating causes the low-melting components within the alloys to vaporize (Huang *et al*., 2022).

Table 4.4: Densities of AlCrCoCuFeNi-HEA samples processed at different conditions.

Sample	Laser power (W)	Scan Speed (mm/s)	Layer thickness (mm)	Hatch spacing (mm)	Measured density (g/cm^3)	Energy density (J/mm^3)	Theoretical density (g/cm^3)	Relative density (%)
a	1200	0.48	0.5	1	6.75	5000	6.85	98.5
b	1200	0.6	0.5	1	6.92	4000	7.05	98.1
c	1200	0.72	0.5	1	6.95	3333	7.15	97.1
d	1400	0.48	0.5	1	6.82	5833	7.00	97.4
e	1400	0.6	0.5	1	6.54	4667	6.56	98.7
f	1400	0.72	0.5	1	6.44	3889	6.63	98.9

Materials properties and characteristics of components produced by AM processes are influenced by the density. Li *et al*. (2022) illustrated that the energy density (*E*) parameter determines the behavioural influence on the DED part. This suggests that the change in the energy density parameter can exert a significant influence on the behaviour of the DED process, potentially affecting various features such as material deposition, fusion, heat-affected zones, or other characteristics inherent to the DED technology. The volumetric energy density (J/mm^3) is given by **Equation 4.1** (Liu *et al*., 2022).

$$Ev = \frac{P}{hvt} \qquad \textbf{(4.1)}$$

Where:

P [W] is the laser power,

h [mm] is the hatch spacing,

v [mm/s] is the scan speed and

t [mm] is the powder layer thickness.

Enneti *et al*. (2018) investigated the effect of parameters on the densification of tungsten using selective laser melting (SLM) technique. From the study, it was found that the densification of tungsten was influenced by the scanning speed. Increasing the scanning speed at high laser power resulted with produced samples having higher relative densities.

The interaction between the scan speed and laser power impacts the way heat is distributed throughout the material. An intricate balance is required to ensure that the energy supplied is sufficient to effectively fuse the material while avoiding excessive energy that may result in insufficient solidification (Chowdhury *et al*., 2022).

During fabrication, high laser power dispenses an immense amount of energy density which in turn fully melts the alloy powder particles to create metallurgical bonding, consequently leading to a progressively higher relative density (Sun *et al*., 2020). This phenomenon also explains the decrease in relative density at lower laser power emanates from the energy density not being high enough to fully melt the powder particles.

4.2.2 Microstructural analysis

The optical microscope was used to analyse the microstructure of AlCrCoCuFeNi-HEA samples. **Figures 4.5-4.10** represent the microstructure of AlCrCoCuFeNi-HEA samples produced under different laser power and scanning speed. The microstructure was observed from the top, middle and the bottom section of the samples.

Figure 4.5 shows the top (a), middle (b) and bottom (c) view of microstructure of sample a, which was produced at the laser power of 1200W and scanning speed of 0.48 mm/s. Image (d) and (e) are a higher magnification of the top-middle and bottom respectively. The microstructure is composed of equiaxed grains and fine dendrites (d(A) and e(B)) which appear to be getting finer when moving to the bottom. Visible cracks can be observed along the grain boundaries of the microstructure shown in Figure 4.5 d(i) and e(ii).

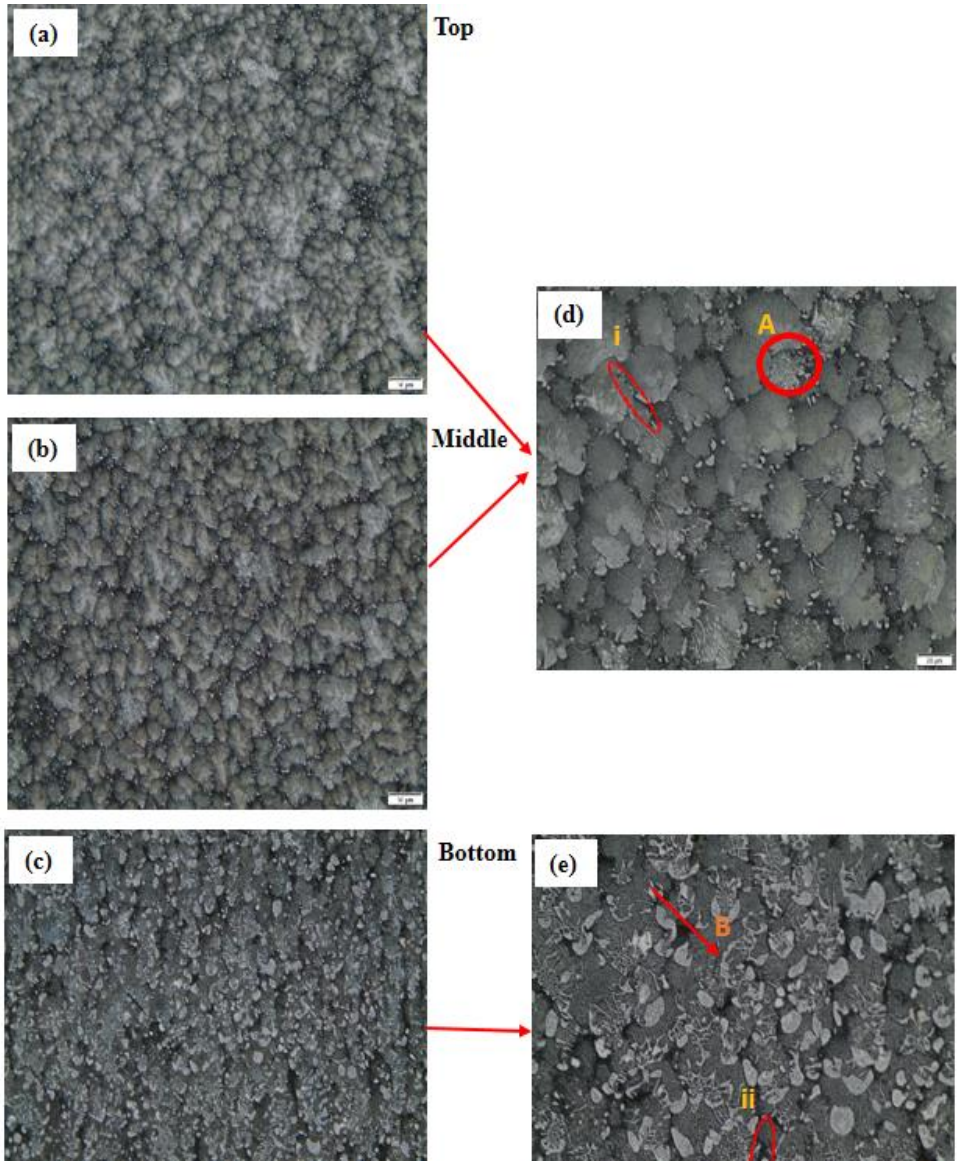


Figure 4.5: Optical microscopic images of sample a, produced at 1200W, 0.48mm/s.

Figure 4.6 shows the top (f), middle (g) and bottom (h) microstructures of sample b produced at 1200W when the scanning speed was increased to 0.6 mm/s. A decrease in grain sizes was notable when moving towards the bottom. The microstructure shown in Figure 4.6(j) is the bottom section of the sample at higher magnification. The microstructure at higher magnification showed fine dendrites in the interior of the equiaxed grains. Cracks were observed in the middle section of the

sample, highlighted with a red circle in Figure 4.6 (i). Figure 4.6 (i) represents Figure 4.6(g) at higher magnification, cracks can be observed at the grain boundaries in i(iii).

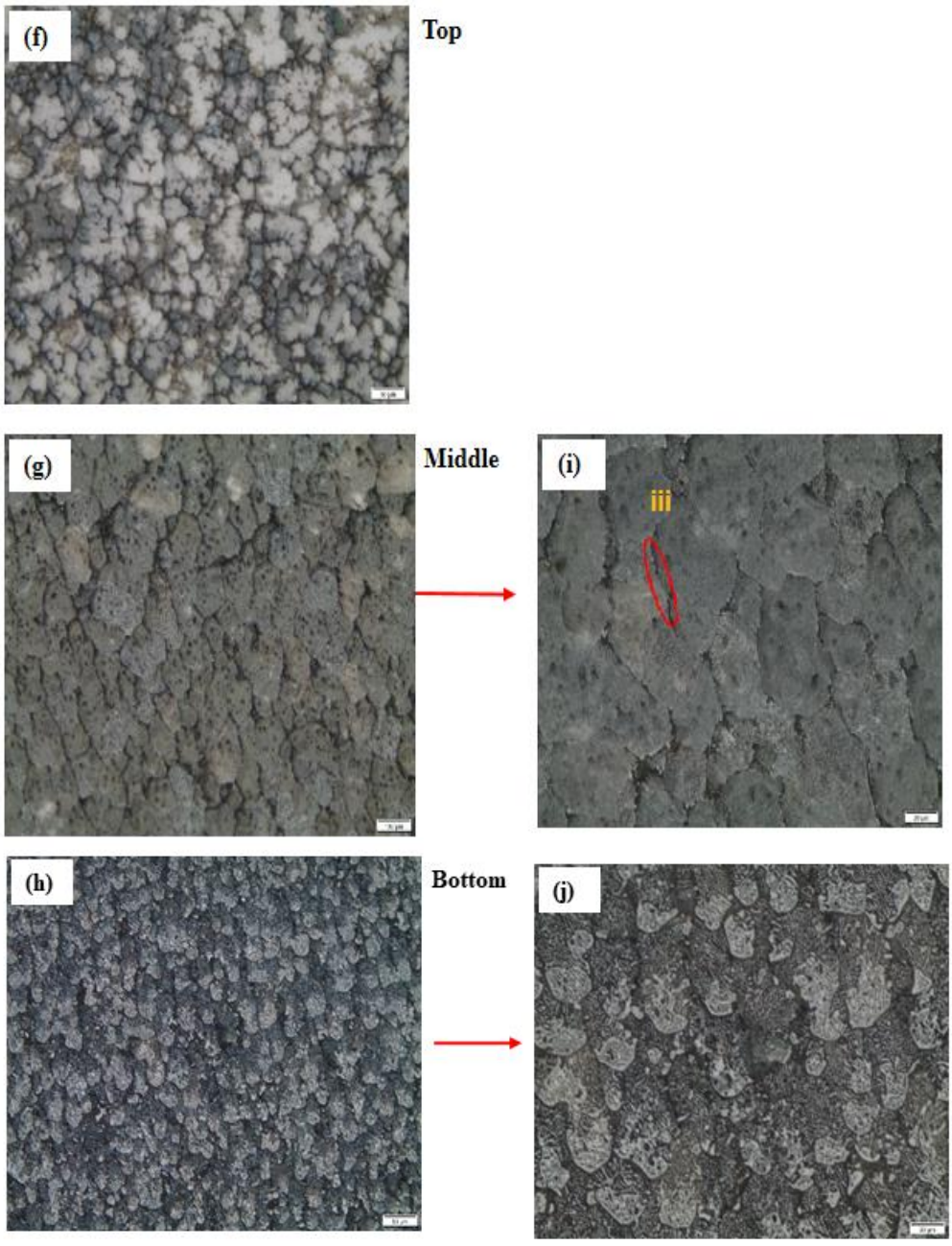


Figure 4.6: Optical microscope images of sample b, produced at 1200W, 0.6mm/s.

Figure 4.7 shows the microstructure the top (k), middle (l) and bottom (m) view of sample c produced at 1200W, with the scanning speed of 0.72 mm/s. The microstructure observed in (k) (l) and (m) contains equiaxed grain, which decreases in size when moving downwards.

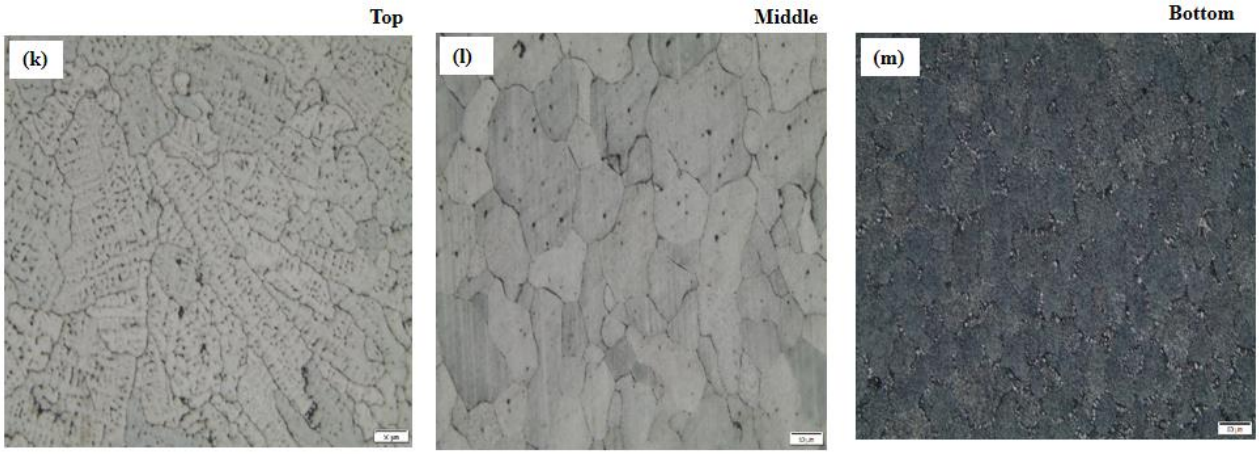


Figure 4.7: Optical microscope images of sample c, produced at 1200W, 0.72mm/s.

Figure 4.8 shows the top, middle and the bottom microstructures of sample d labelled n, o, and p respectively. The microstructure is characterised by equiaxed grains. An evident increase in grain size was observed when moving towards the bottom.

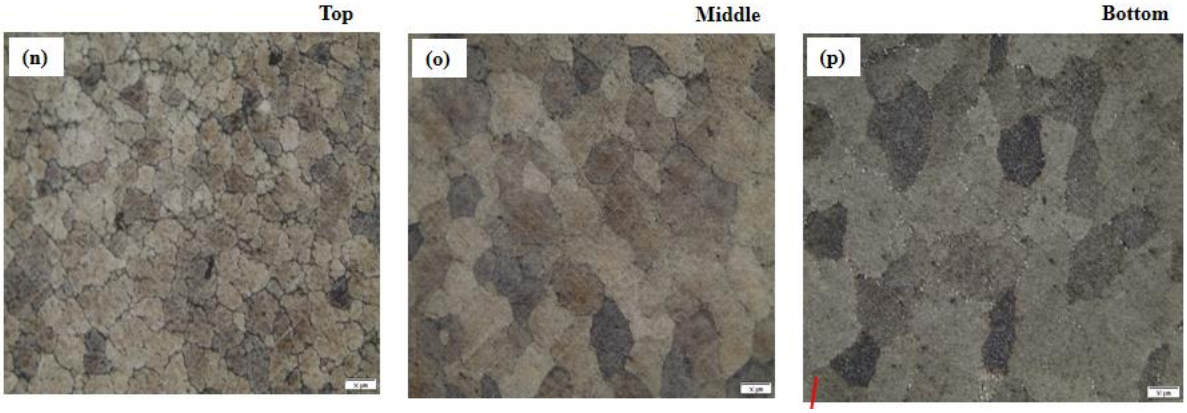


Figure 4.8: Optical microscope images of sample d, produced at 1400W, 048mm/s.

Figure 4.9 shows the top (r), middle (s) and bottom (t) microstructure of sample e produced at 1400W and a scanning speed of 0.6 mm/s. The characteristic microstructure of the samples was predominantly equiaxed grains. Figure 4.9 (u) represents the bottom microstructure of sample e at higher magnification. The figure shows dendrites that are constructed in a net-like structure (Zhou *et al*., 2008). The bottom of the sample u(v) contains cracks along the grain boundaries.

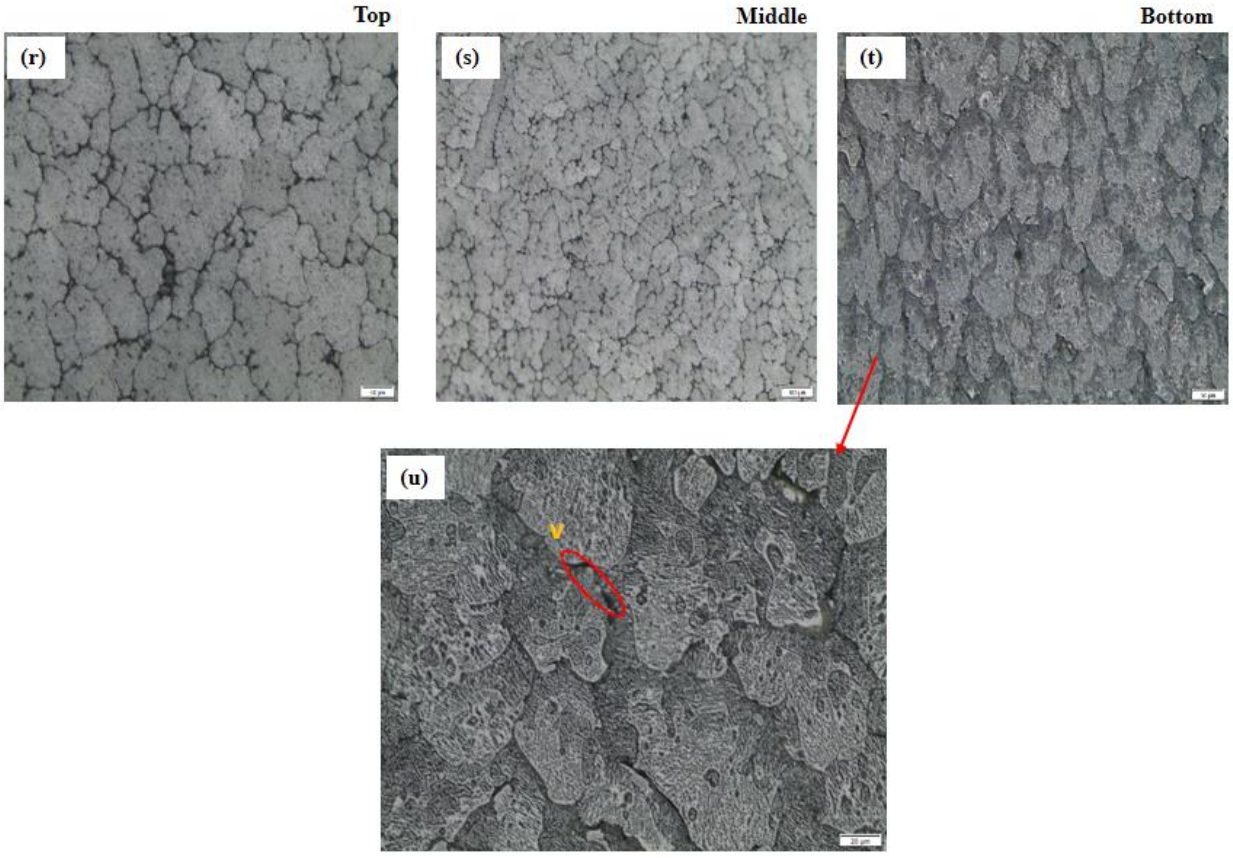


Figure 4.9: Optical Microscope images of sample e, produced at 1400W, 0.6mm/s.

Figure 4.10 shows the top (v), middle (w) and bottom (x) microstructure of sample f produced at the laser power and scanning speed of 1400W and 0.72 mm/s respectively. The microstructure is characterised by equiaxed grains across the sample.

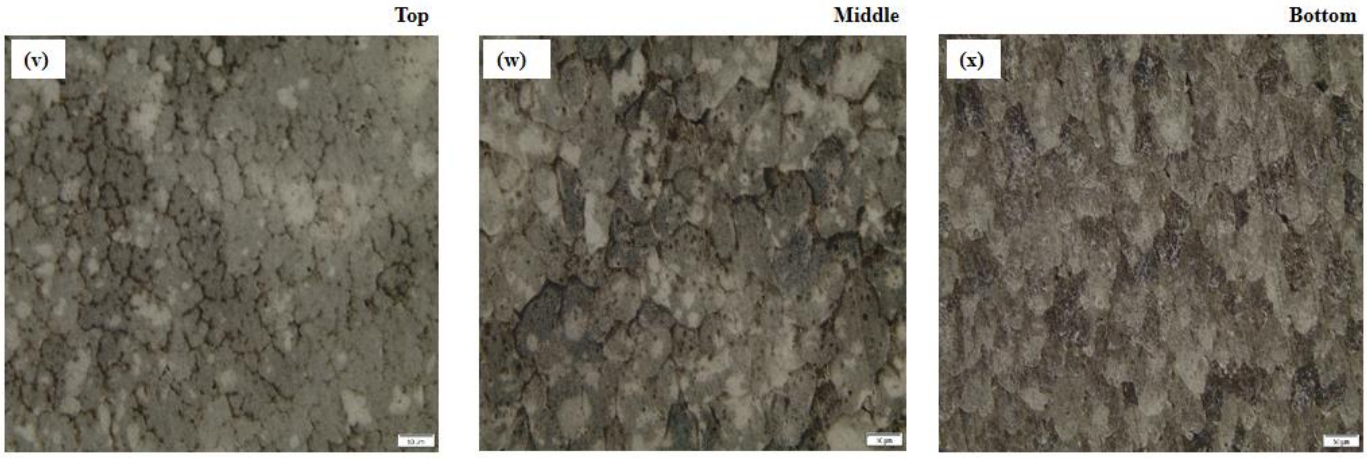


Figure 4.10: Optical Microscope images of sample f, produced at 1400W, 0.72mm/s.

The obtained results show distinct differences in microstructure and grain size when the laser power and scanning speed is varied. Samples a, b, and c that were produced at 1200W have fine equiaxed grains at the bottom. The correlation between laser power and grain size is commonly attributed to the cooling rate of the material during laser processing. Lower laser power leads to a decrease in the amount of energy input, which results in fast cooling rate. The rapid cooling limits the duration for atomic reorganisation and the grain growth. Consequently, the reduced time available for grain growth results in the development of finer microstructures. Liu *et al.* (2023) investigated the impact of laser power on the microstructures and characteristics of Al-4.82 Mg-0.75. The authors conclude that lower laser power resulted in the formation of fine grains (Liang *et al*., 2018; Liu *et al*., 2023).

Increasing the scanning speed when the laser power is relatively low results with low heat being accumulated in the material, which subsequently leads to the formation of fine grains (Chen *et al*., 2022).

Samples d, e, and f which were produced at a higher laser power of 1400W were characterised by the presence of larger equiaxed grains in (p), (t), and (x) respectively. Increasing laser power and

increasing scanning speed leads to slow cooling rates which results with grain growth taking place (Chen *et al.*, 2022; Prasad *et al*., 2020).

Preheating the substrate influences thermal dynamics in the additive manufacturing process, particularly the cooling rates in different material regions. Slow cooling rates at sections that are in contact with the substrate are due to preheating, which leads to the formation of a coarse microstructure (Zhou *et al*., 2019).

The intergranular cracks that were observed in the microstructures were more pronounced at higher laser power. Liu *et al*. (2022) reported that crack morphology on the AM part is due to the temperature gradient and large residual stresses. Gong *et al*. (2014) observed that the solubility of the gas when the metal is in the molten state causes embrittlement that subsequently leads to the formation of the cracks along the grain boundaries (Prasad *et al*., 2020).

In the context of aerospace applications, 1200W is the preferred laser power setting because of the tendency to form finer grains with improved properties (Bhat *et al*., 2018).

4.2.3 Phase analysis

X-ray diffraction (XRD) was employed to analyse the phases of AlCrCoCuFeNi-HEA. The XRD pattern of the DED AlCrCoCuFeNi-HEA in its as-built state is shown in **Figure 4.11**, with peaks showing a solid solution of BCC and FCC phases. **Figure 4.11** (b) shows the enlarged (200) peak at a 2θ angle. Sample a, produced at lower laser power is comprised predominantly by BCC phases, whilst the alloy produced at a higher laser power has FCC phases. Intermetallic compounds were not observed. The formation of solid solutions in HEAs at high temperatures is more stable than intermetallic compounds, this is as a result of the large entropies of mixing found in the multi-principal elements (Tung *et al*., 2007).

The formation of solid solution crystal structure is prompted by the rapid heating and solidification of laser deposition, which is found to be favourable in improving the solubility limit of each element in HEA (Zhang *et al*., 2020). The atomic radius of each element differs thus leading to an

increase in solid-liquid interface energy during solidification, the lattice distortion occurs over a long range during the diffusion of atoms (Chen and Yan, 2016).

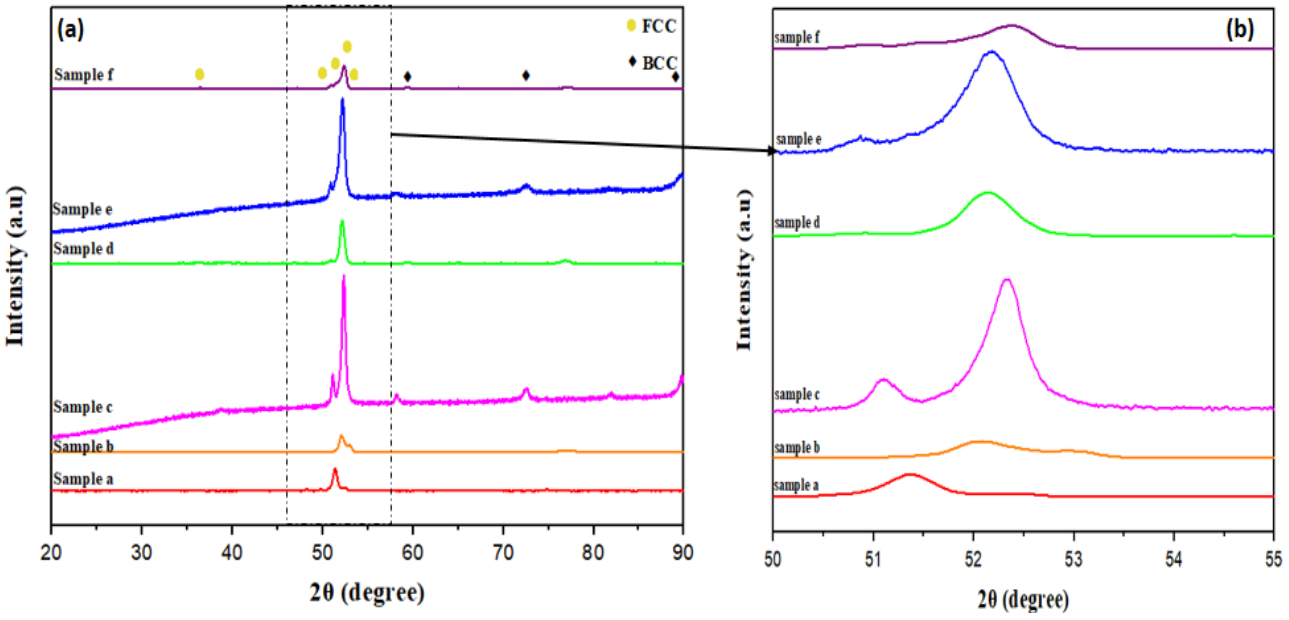


Figure 4.11: X-ray diffraction pattern of as-built AlCrCoCuFeNi HEA: (a) at different laser power and scan speed, (b) enlarged (200) peak.

The AlCrCoCuFeNi-HEA contains high entropy state. The hybrid high entropy of this effect reduces the Gibbs free energy of the system, promoting the production of solid solutions instead of ordered compounds (Zhang *et al*., 2020). The BCC phases are predominantly found in the XRD patterns. Zhang *et al*. (2022) concluded that the presence of dominant BCC structure in HEAs is linked to an increased in hardness. The samples are characterised by a similar peak at (200), **Figure 4.11** (b) shows the peak shifts to a higher 2θ angle. The result of an increasing 2θ angle decreased the lattice spacing plane. This is due to the volume expansion of the microstructure which produces stress that affects the lattice parameter of the grain boundary (Yuting *et al*., 2019; Huang *et al*., 2022).

4.2.4 Hardness

A micro-Vickers hardness tester was used to measure the hardness of AlCrCoCuFeNi-HEA. The hardness profile of samples a, b, c, d, e, and f are shown in **Figure 4.12,** and summarised in **Table 4.5**.

It was observed that lower laser power resulted in higher hardness, this is the result of lower solidification rate and finer microstructures. Materials with finer microstructures, which are commonly identified by smaller grain sizes, tend to enhance hardness. The presence of smaller grains results in an increased number of grain boundaries inside the material. The presence of grain boundaries in a material hinders the movement of dislocations under the influence of applied stress (Ke *et al*., 2022).

A higher laser power resulted in lower hardness. An increase in laser power can potentially accelerate the process of solidification and result in the formation of larger grain sizes, ultimately leading to a reduction in hardness values. Liu *et al*. (2022) found that the hardness of the SLM fabricated Al-Mg-Sc-Mn samples decreased with an increase in laser power due to low solidification which formed fine grains in the microstructure.

The fabrication of DED AlCrCoCuFeNi-HEA resulted in higher hardness contrary to the AlCrCoCuFeNi-HEA that were fabricated by arc melting and casting methods. Tung *et al*. (2007) reported hardness values of 473HV in arc-melting of AlCoCrCuFeNi HEA, which is relatively low when compared to samples that were produced at 1200W and low scanning speed of 0.48 mm/s.

Table 4.5: Average hardness of samples a, b, c, d, e, and f.

	Sample a	**Sample b**	**Sample c**	**Sample d**	**Sample e**	**Sample f**
Average hardness	563HV	563HV	457HV	337HV	333HV	299HV

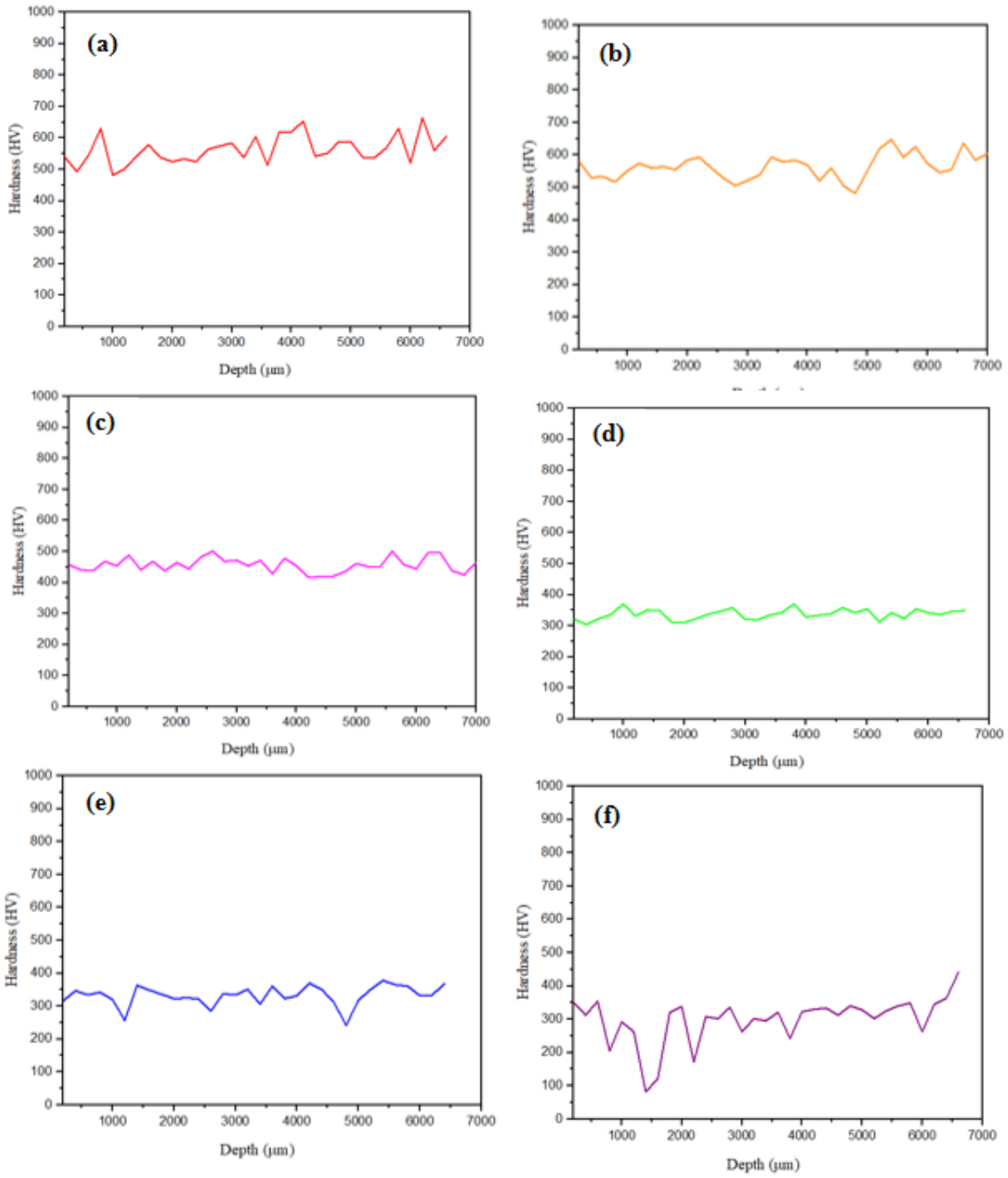


Figure 4.12: Hardness profile of samples a, b, c, d, e and f at different laser power and scanning speed.

The fast-cooling rate in DED fabrication techniques, result in s rapid solidification that promotes the formation of a fine-grained microstructure that contributes to higher hardness. In contrast, arc melting and casting result in a slower cooling rate, leading to the formation of a coarser microstructure and reduced hardness (Li *et al*., 2019). Additionally, DED allows for better control

over the process parameters, such as the energy input and cooling rate, which can be tailored to optimise the microstructure and properties of the material. On the other hand, arc-melting and casting methods have limited control over these parameters, which can result in variations in the microstructure and properties of the fabricated material (Jia *et al*., 2016).

These observations highlight the significant influence of process parameters, specifically laser power, on the hardness of processed materials. Lower laser power often promotes the formation of fine microstructures and increases the hardness of the material by creating more grain boundaries. Conversely, higher laser power often results in larger grain sizes and a decrease in material hardness.

Preheating facilitates attaining homogenous heating across the alloy during fabrication. This ensures better mixing of alloying constituents. The uniformity of the material can enhance the consistency of its microstructure, leading to an enhancement in hardness (Sonkusare *et al*., 2020). Ding *et al*. (2018) examined the effects of substrate preheating on the microstructure and characteristics of 12CrNi2 produced using laser cladding deposition. The study provided strong evidence in favour of the notion that proper preheating of substrate significantly improves the mechanical properties of the material. The study further showed that there was a gradual increase in hardness near-base layer to the surface layer.

4.3 Post-Processing

This section focuses on the surface polishing methods for the untreated as-built samples a_3, b_3, c_3, d_3, e_3, f_3.

4.3.1 As-built sample

Figure 4.13 displays SEM images taken from the top surface of as-built untreated AlCoCrCuFeNi-HEA. The untreated surfaces were affected by several defects, such as the balling effect. Yang *et al*. (2022) stated that the presence of inadequate inter-layer bonding can intensify the occurrence of the balling effect. In instances where there is inadequate bonding between adjacent layers, the

partially melted particles originating from the lower layers may not fully integrate with the freshly deposited material. The fused layers tend to produce delamination and porosity resulting from poor inter-layer bonding in combination with thermal stresses. Gu and Shen. (2009), observed that when a lower laser power is used, it results in a balling phenomenon where the balls formed have a coarser structure and reduced strength due to the low undercooling of the melt caused by the insufficient laser input.

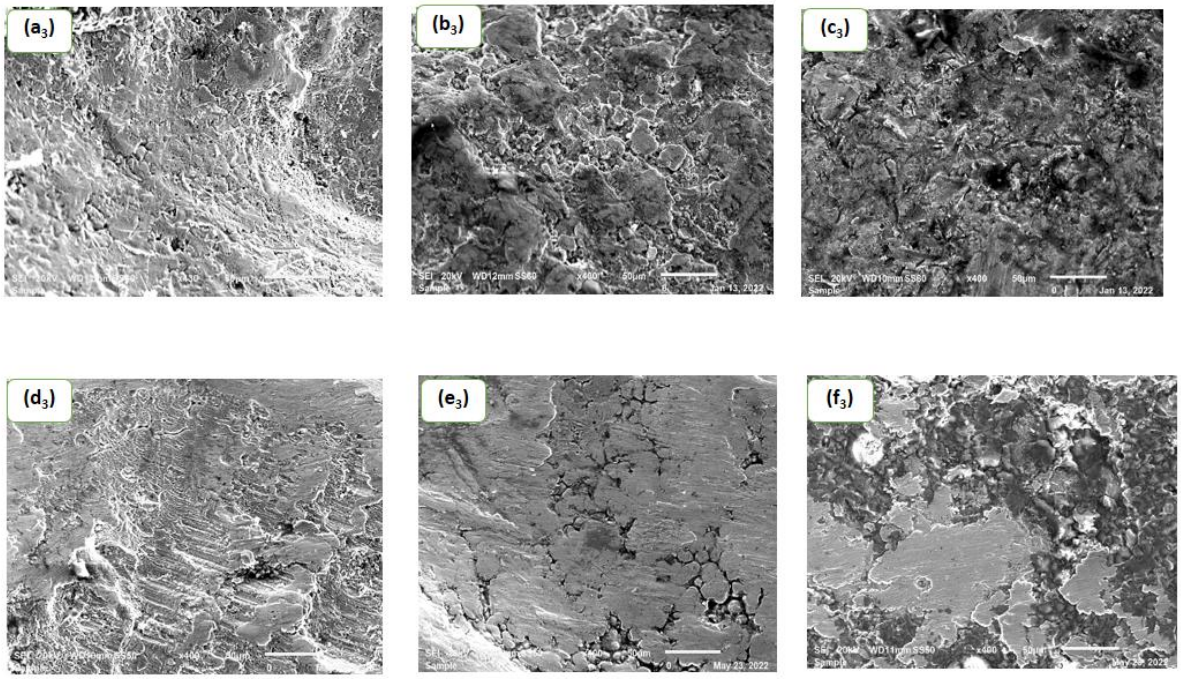


Figure 4.13: SEM images of untreated as-built samples a_3, b_3, c_3, d_3, e_3, and f_3.

Figure 4.14 represents the roughness profile of the untreated samples a_3, b_3, c_3, d_3, e_3 and f_3. The obtained results are tabulated in **Table 4.6**.

Table 4.6: The untreated result of as-bult samples a_3, b_3, c_3, d_3, e_3, and f_3.

Sample	Laser power (W)	Scan speed (mm/s)	Ra (µm)	Rz (µm)
a_3	1200	0.48	13.78	131.85
b_3	1200	0.6	13.17	159.55
c_3	1200	0.72	17.36	168.48
d_3	1400	0.48	6.15	58.69
e_3	1400	0.6	6.16	58.69
f_3	1400	0.72	5.09	56.52

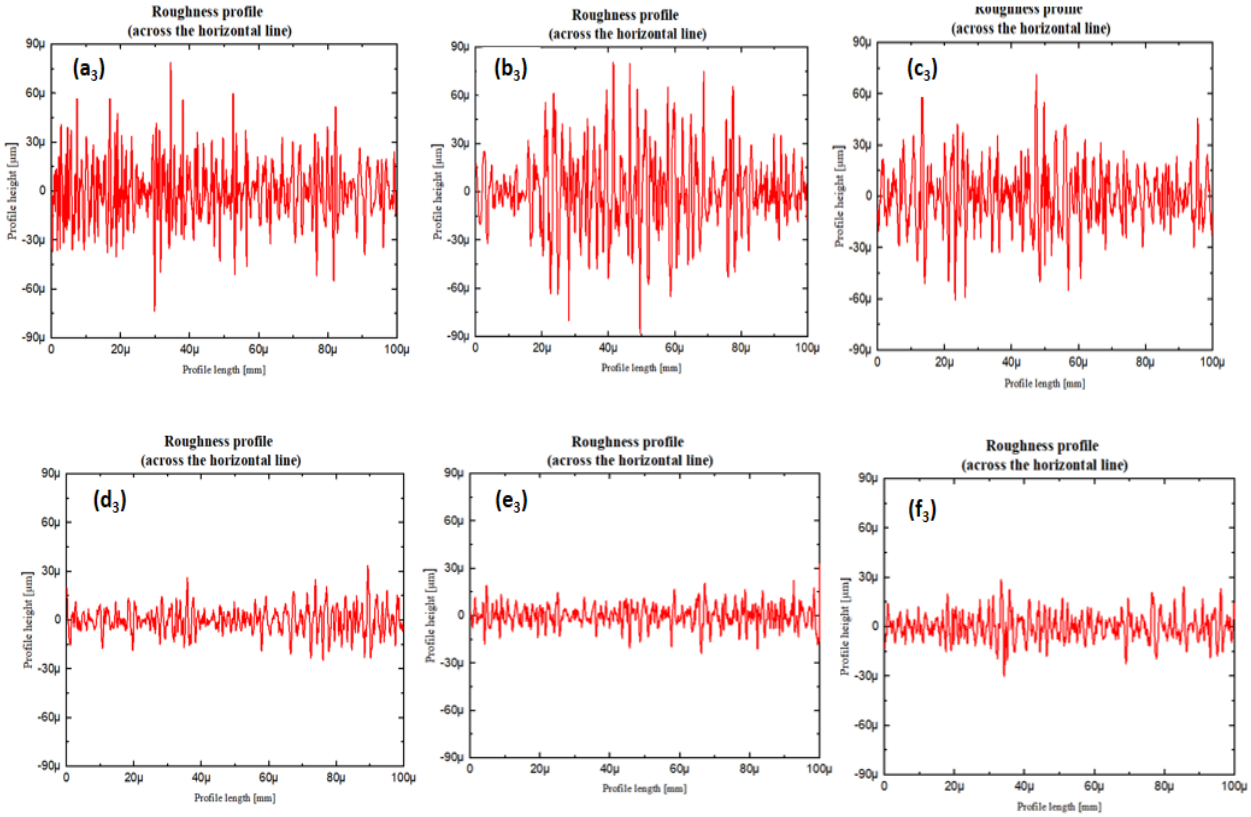


Figure 4.14: Roughness profile of the untreated as-built samples a_3, b_3, c_3, d_3, e_3, and f_3.

Figure 4.14 represents the roughness profile of the untreated samples a_3, b_3, c_3, d_3, e_3 and f_3. The obtained results are tabulated in **Table 4.6**.

High surface roughness was observed at 1200W. The high roughness was due to the formation of coarser and weaker balls that were formed because of insufficient energy input, a phenomenon known as balling effect. (Manakari, Parande and Gupta, 2016) stated that the presence of balling region is characterised by clustering of spherical particles, resulting in the formation of large-size melt pools, which can be attributed to a combination of low laser power, high scanning speed, and layer thickness. The irregularities on the metal surfaces are attributed to peaks-to-valleys.

A decrease in surface roughness was observed when the scanning speed was increased when the laser power was 1400W. High laser power and increasing scan speed may lead to changes in chemical composition, potentially affecting the efficacy of the electropolishing process. Some regions of the surface may experience reduced susceptibility to dissolution (Chaghazardi and Wüthrich, 2022).

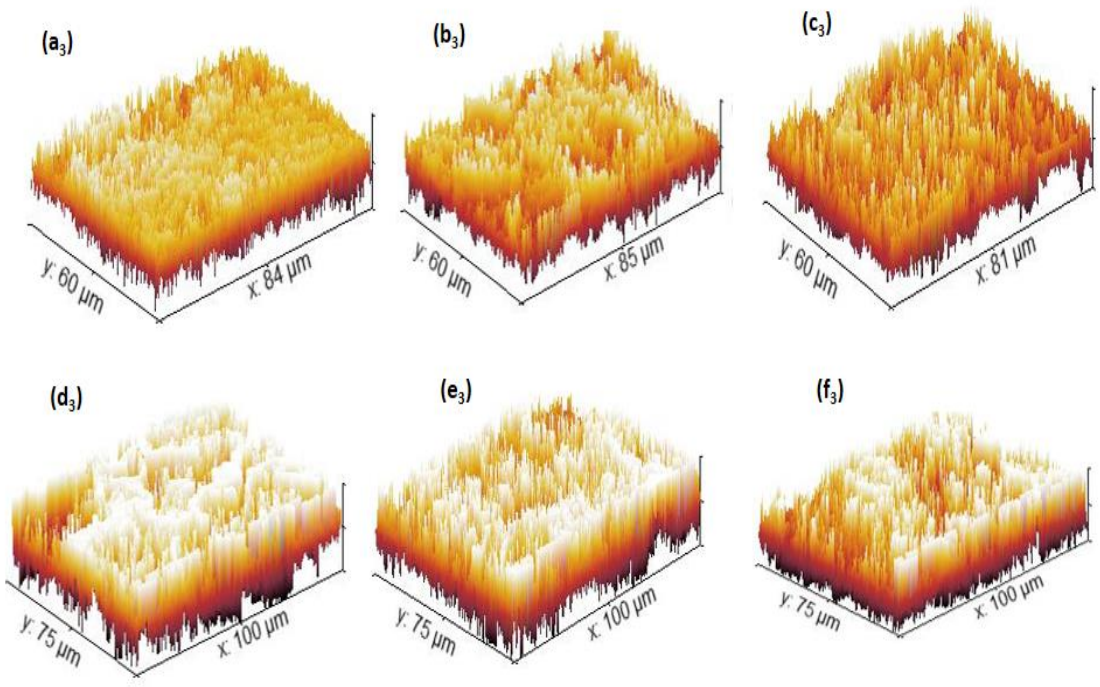


Figure 4.15: Three-dimension topographical representation of the untreated sample a_3, b_3, c_3, d_3, e_3 and f_3.

Figure 4.15 comprises of 3D topographical field of untreated samples a_3, b_3, c_3, d_3, e_3 and f_3. The untreated surfaces are characterised by very high peak-to-valley height as shown in **Table 4.6**. The

peak-to-valleys are a representation of the balling effect, irregular and rough surfaces produced in the DED fabrication process.

4.3.2 Electropolishing

This section focuses on the electropolished samples a_1, b_1, c_1, d_1, e_1, f_1 polished at 1200W and 1400W. The electropolishing of AlCrCoCuFeNi-HEA took place in the presence of 80% methanol and 20% sulfuric acid electrolyte using a Struers LectroPol-5 machine to polish the samples.

4.3.2.1 Polarization

Figure 4.16 represents the linear sweep voltammetry (LSV) curve, which is used to determine the anodic polarization behaviour on AlCrCoCuFeNi HEA.

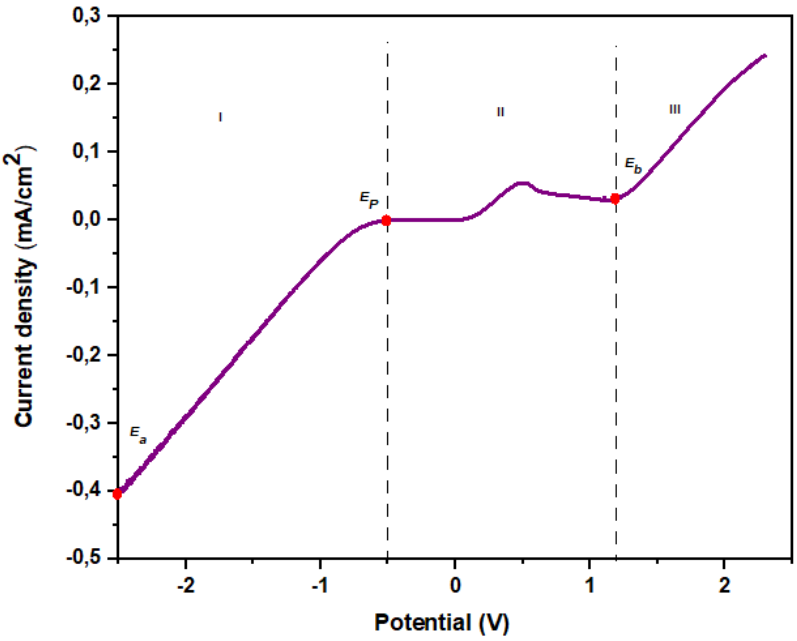


Figure 4.16: Linear sweep voltammetry graph of AlCrCoCuFeNi HEA.

The polarization curve consists of three regions. The region between -2.5V and -0.5V is the active region (I) were current increases with increasing potential. The potential at -3V is called activation

potential (E_a). The region between -0.5V to 1.24V is the passive region (II) where the current is stable for an increasing voltage. The voltage at -0.5V is termed passive potential (E_p). The region after E_p depicts a rapidly increasing current in the trans-passive region (III), this region is known as the gas evolution region where oxygen gas bubbles are evolved. The corresponding potential at 1.24V is called the breakdown potential (E_b). EP occurs in the passive region, where a viscous film with a higher resistance than that of the electrolyte is formed.

Figure 4.17 displays the SEM micrographs of the EP samples. Enhanced surface quality was reported following the implementation of EP. A delineated grain structure is seen in samples a_1, b_1, and c_1 but disappears with reduced polishing time thus, a change in microstructure can be observed. Sample d_1 exhibits smooth spherical equiaxed grains. Sample f_1 comprises of spherical equiaxed grains with embedded dendrites in-between sample e_1 and f_1 label (A) and (B) respectively, which are net-like structured and gullies along the grain boundaries of sample e_1 and f_1 label (D) and (E) respectively.

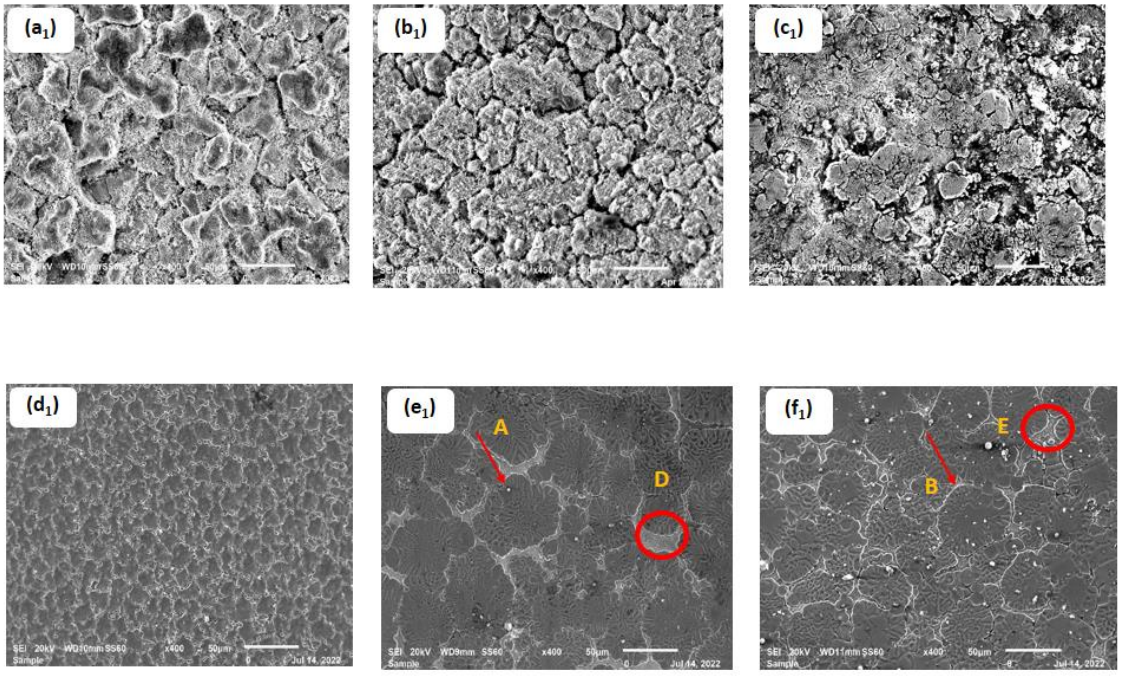


Figure 4.17: The electropolished SEM micrographs of AlCrCoCuFeNi HEA.

Table 4.7: Roughness profile of the electropolished samples a_1, b_1, c_1, d_1, e_1, and f_1.

Sample	Laser power (W)	Scan speed (mm/s)	Ra (µm)	Rz (µm)	Time (sec)	Agitation (rpm)	Temperature (°C)	Voltage (V)
a_1	1200	0.48	6.93	66.92	30	20	28	-0.5
b_1	1200	0.6	9.94	90.06	30	20	30	-0.5
c_1	1200	0.72	10.20	93.71	30	20	32	-0.5
d_1	1400	0.48	3.89	37.68	60	20	26	-0.5
e_1	1400	0.6	3.03	31.92	60	20	27	-0.5
f_1	1400	0.72	2.29	26.90	60	20	28	-0.5

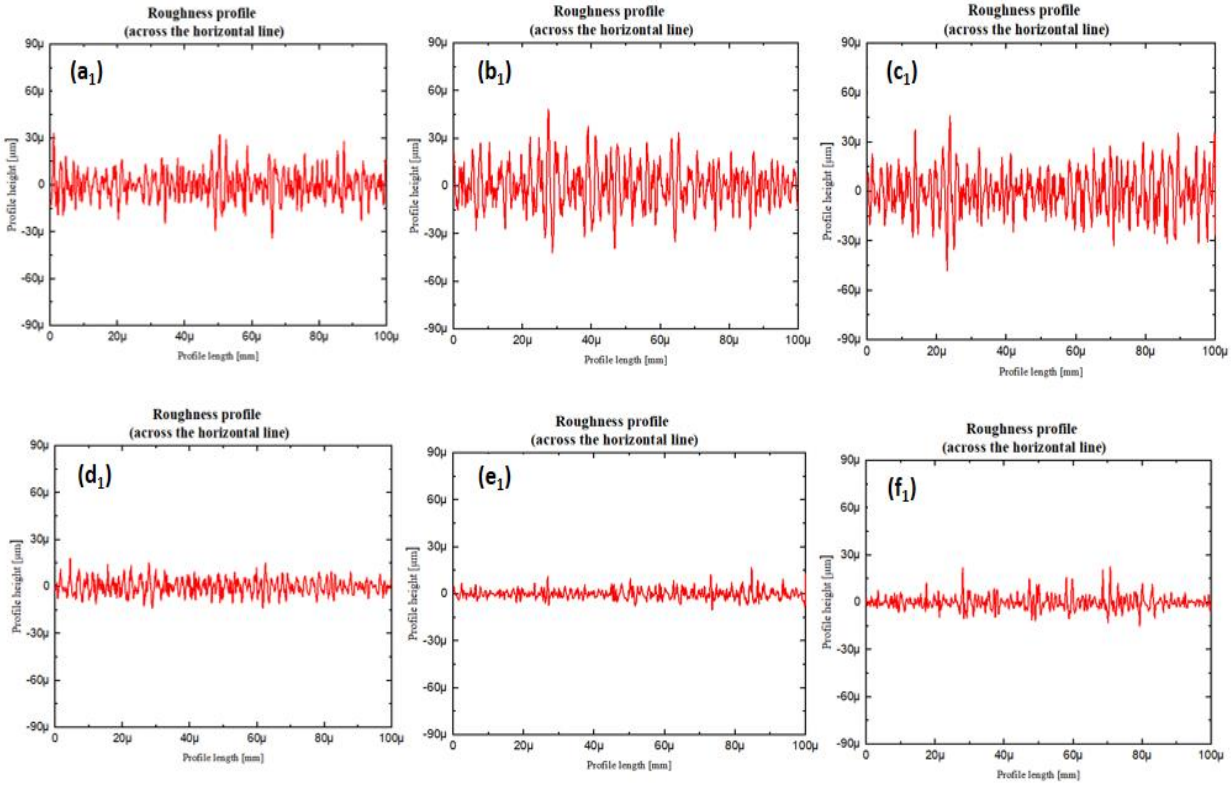


Figure 4.18. Roughness profile of the electropolished samples a_1, b_1, c_1, d_1, e_1 and f_1.

Figure 4.18 represents the roughness profile of the electropolished samples a_1, b_1, c_1, d_1, e_1 and f_1. The obtained results are tabulated in **Table 4.7**.

Increasing the scanning speed when the power was set at 1200W increases the measured average surface roughness and peak-to-valley increases. Elevated temperatures led to enhanced surface removal due to the accelerated electropolishing rate associated with higher temperatures (Aksu *et al.*, 2016). As temperatures increase, the conductivity of the electrolyte also increases, leading to a higher rate of anodic dissolution. (Kumar and Das, 2021; Kumar *et al.*, 2021).

Increasing the scanning speed when the laser power was set at 1400W led to a decrease in the average surface roughness and peak to valleys. At higher laser power, the lower hardness of AlCrCoCuFeNi-HEA leads to increased ductility due to increased temperatures. This can make it more difficult for the material to resist the mechanical forces required for surface removal (Tokarewicz and Grądzka-Dahlke, 2021).

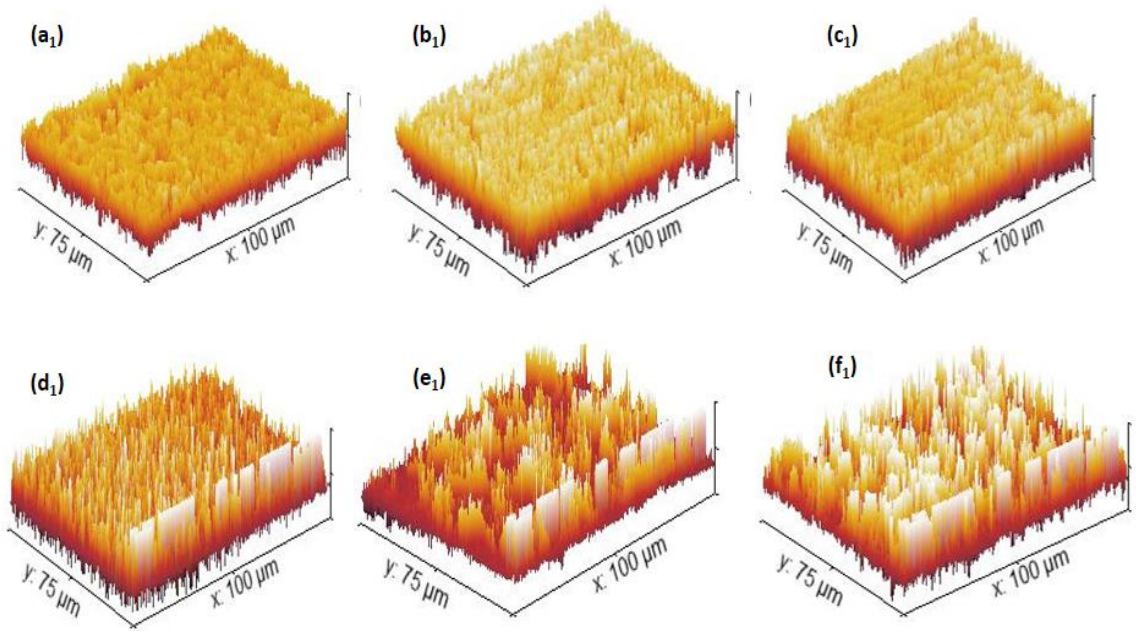


Figure 4.19: Three-dimension topographical representation of the electropolished sample a_1, b_1, c_1, d_1, e_1 and f_1.

Figure 4.19 presents 3D topographical images of samples a_1, b_1, c_1, d_1, e_1 and f_1. The surface removal in sample a_1 is 50.29 b_1 is 58.65%, c_1 is 75.48%, d_1 is 50.29%, e_1 is 45%, and f_1 is 49.19%. The laser power reduction bracket of 1200W exceeds that of 1400W. The sharp peaks on the as-

built which represented the balling effect, non-uniformed and rough surface were successfully removed, which lead to a roughness that is much lower than that of the as-built.

4.3.3 Centrifugal Barrel Finishing

This section focuses on the centrifugal barrel finished samples a_2, b_2, c_2, d_2, e_2, and f_2 polished at 1200W and 1400W. The centrifugal barrel finishing machine was used to polish the samples using ceramic media in the first samples a_2, b_2, c_2. Subsequently enhancing the polishing by using ceramic, plastic and zirconia media on samples d_2, e_2, f_2. Water, and a small amount of LC-13 polishing liquid was used to achieve a smooth shiny finish.

Figure 4.20 represents the micrographs of CBF samples a_2, b_2, c_2, d_2, e_2 and f_2. The barrel finishing process removed sloping plane on the sample caused by the balling effect. It could be seen that the finishing process removed the oxides effectively thus removing the spatters to a great extent. Ceramic media was only used during the polishing of samples a_2, b_2, c_2. Since the surface removal action is based on rubbing, and deburring, the media interaction with the sample was vigorous for a prolonged period. The polished samples contain embedded scratches on samples a_2, b_2, c_2 because of the period the samples were subjected to polishing.

The use of ceramic, plastic and zirconia balls was implemented in samples d_2, e_2, f_2 to improve the quality from the first set of samples (a_2, b_2, c_2). Ceramic media was applied for 3 hours, plastic media for 2 hours, and zirconia balls for the remaining 2 hours to make a total of 7 hours. The surface roughness for samples d_2, e_2, f_2 was smooth without deep scratches.

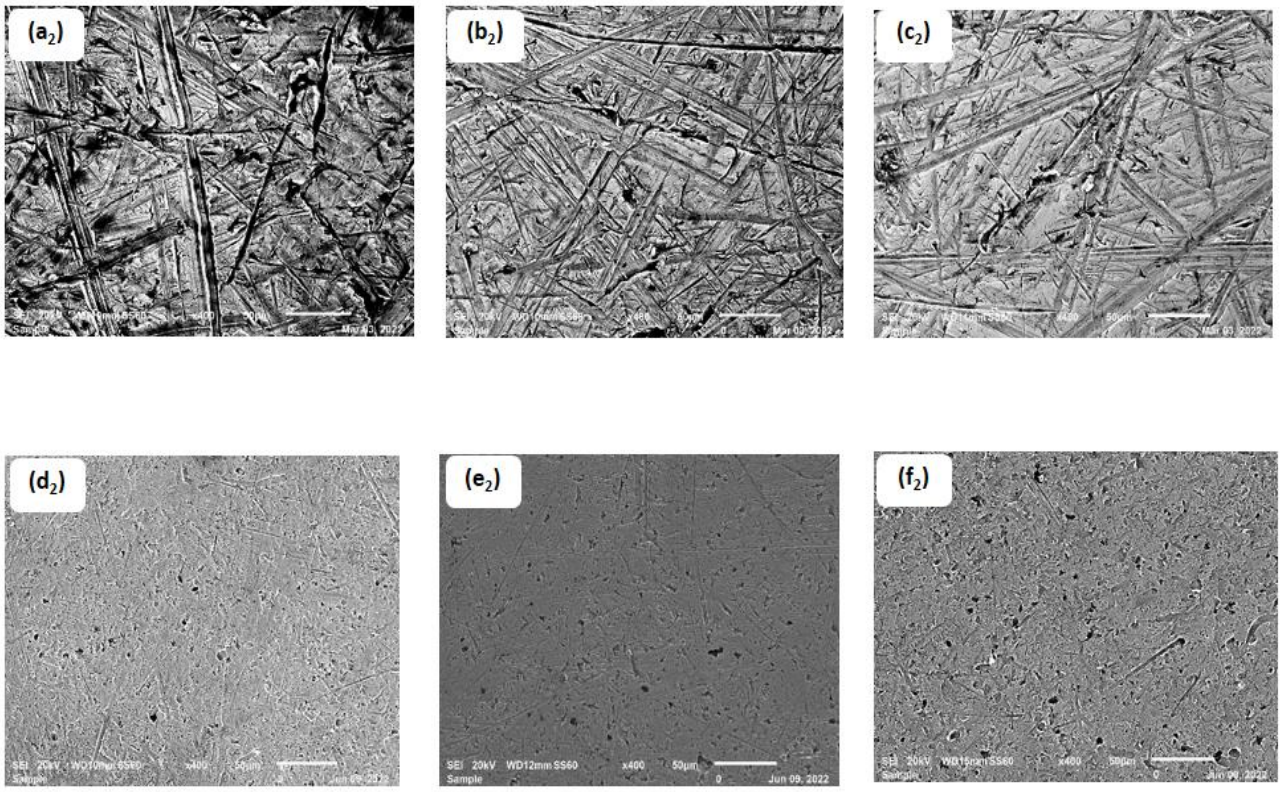


Figure 4.20: SEM images of centrifugal barrel finished samples a_2, b_2, c_2, d_2, e_2, and f_2.

Table 4.8: Presents the roughness profile of CBF samples a_2, b_2, c_2, d2, e2, and f_2.

Sample	Laser power (W)	Scan speed (mm/s)	Ra (µm)	Rz (µm)	Time (sec)	Rotation speed (rpm)
a_2	1200	0.48	7.63	83.34	14	85
b_2	1200	0.6	5.68	64.06	14	85
c_2	1200	0.72	5.59	74.49	14	85
d_2	1400	0.48	5.29	58.06	7	85
e_2	1400	0.6	2.66	24.5	7	85
f_2	1400	0.72	5.97	17.71	7	85

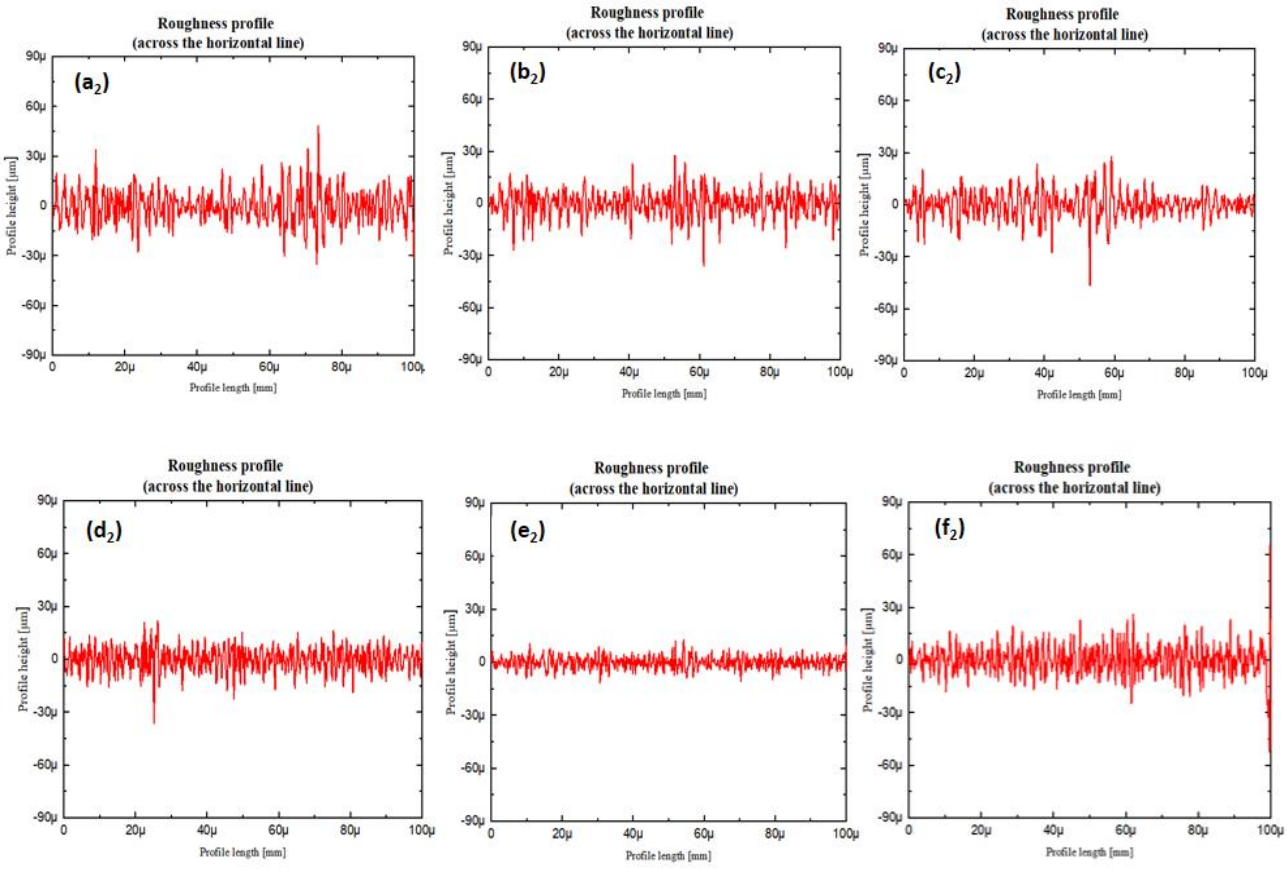


Figure 4.21: Roughness profile of the centrifugal barrel finished sample a_2, b_2, c_2, d_2, e_2, f_2.

Figure 4.21 shows the roughness profile of samples a_2, b_2, c_2, d_2, e_2, and f_2 using the CBF method, with the results are tabulated in **Table 4.8**.

The surface roughness decreased with increasing scanning speed when the power was 1200W. The decrease in surface roughness was due to lower laser power that has the potential to generate less heat during the laser processing of materials. As the scan speed increases, the duration of exposure to laser energy decreases, thereby resulting in a decrease in heat input and reduction of material melting. Consequently, this may give rise to a surface that is less responsive to subsequent mechanical processes such as barrel finishing, as it may not have undergone significant phase changing (Singh *et al.*, 2020). The embedded scratches that are found on the surface of the samples

are due to the rubbing and deburring of the ceramic media. Therefore, a less abrasive media was required for a smoother finish.

The degrees of improvement in surface quality for samples that were produced at 1400W laser power was influenced by the use of different media (ceramic, zirconia, and plastic) that were used for shorter periods. Each type of media has unique abrasive properties, which has an impact on the polishing outcome. The increased energy input has the potential to induce more substantial material removal, encompassing processes such as melting, vaporization, or polishing (Kaschel, Celikin and Dowling, 2020).

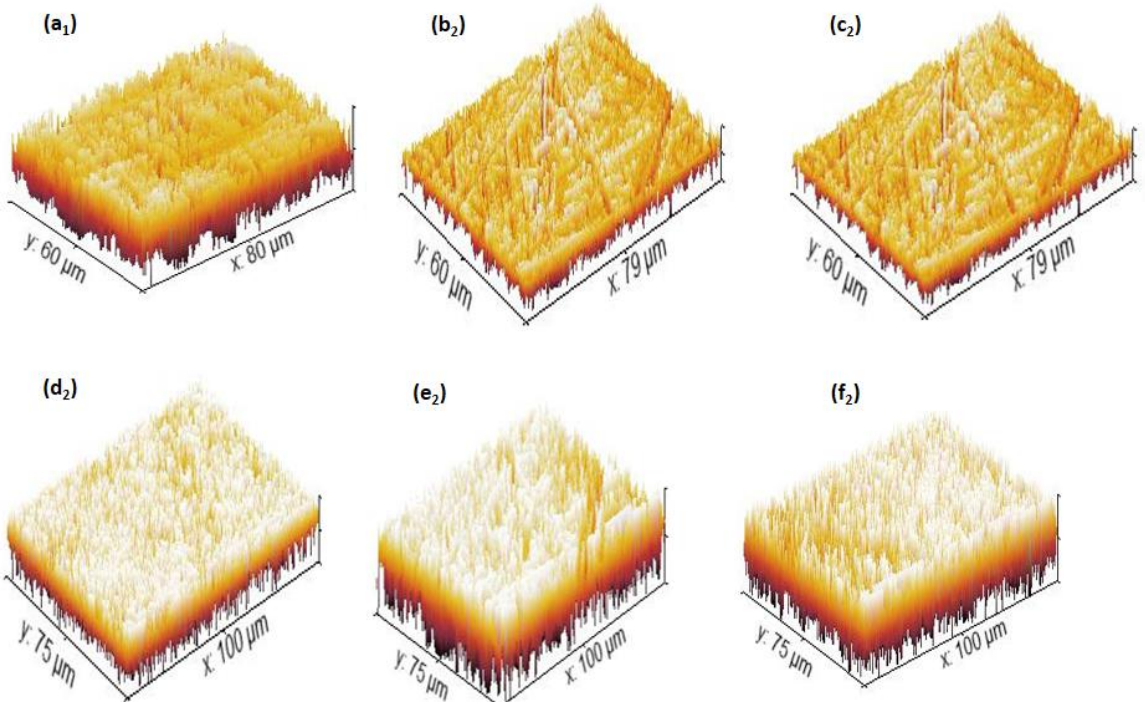


Figure 4.22: Three-dimension topographical representation of the CBF sample a_2, b_2, c_2, d_2, e_2 and f_2.

Figure 4.22 presents the post-polishing 3D image of the topographical field of a_2, b_2, c_2, d_2, e_2 and f_2. The average surface roughness percentage obtained after 14 hours were; a_3 to a_2 is 55.37%, b_3 to b_2 is 43.13% and c_3 to c_2 is 32.2%. After 7 hours of polishing a decrease of d_3 to d_2 is 86.02%, e_3 to e_2 is 43.18% and f_3 to f_2 is 90% is observed. The higher laser power exhibits a higher surface

percentage removal. Overall, there was success in the surface removal and the peak-to-valley value of the CBF sample was much lower than that of the as-built.

The overall unpolished and CBF polished samples used in the study are shown in **Figure 4.23**.



Figure 4.23: DED untreated as-built samples (i) (iii) and CBF treated samples (ii) (iv).

Therefore, the surface roughness resulting from varying laser process parameters, such as laser power and scan speed, can be impacted by the selection of media and the parameters of the CBF process.

In order to improve surface conditions, it may be beneficial to choose a suitable media. In this research, employing less abrasive media proves advantageous in mitigating the potential for embedding scratches that may arise from the use of ceramics. Plastic media can offer a more delicate polishing action.

The optimisation of surface polishing quality can be achieved by high laser power and increasing scan speed. The selection of these parameters attained a substantial surface finish, making AlCrCoCuFeNi-HEA ideal candidates for achieving the desired surface finish.

Electropolishing provided the most effective polishing method. The intricate relationship between laser processing and electropolishing is influenced by, temperature, material properties (such as hardness), and laser parameters processes (particularly, laser power and scan speed). These factors jointly influence the surface roughness of the material.

4.4 High-temperature oxidation

High temperature oxidation behaviour of DED-produced AlCrCoCuFeNi-HEA was determined using an ULTRA-FURN furnace. **Figure 4.24** shows the mass change of each sample before and after oxidation at different laser power and scanning speed. The samples were subjected to a temperature of 1000ºC for 200 hrs. The relationship between oxidation and mass change per surface area and time at high temperatures is presented in **Equation 4.2**:

$$\left(\frac{\Delta m}{A}\right)^n = kt \qquad \textbf{(4.2)}$$

Where Δm (kg) is the mass change,
A (m^2) is the surface area,
n is the exponential index,
K (m^2/s) is the kinetic constant and
t (sec) is the exposure time.

The average mass change per surface area is presented in **Table 4.9**. There is a significant mass gain at lower laser power, whereas a minimal to a negligible weight gain at high laser power is observed. At lower laser powers, there may be a greater increase in mass compared to higher laser powers. This phenomenon might be attributed to the incomplete melting or reaction of the powder particles as a result of the reduced energy input. Under these circumstances, a considerable proportion of the powder might not completely fuse or undergone a chemical reaction with the sample, leading to unreacted particles adhering to the surface or becoming embedded within the

material (Liu and Guo, 2020). The unreacted particles can be prone to oxidation when exposed to oxidising environment (Huang *et al*., 2022)0.

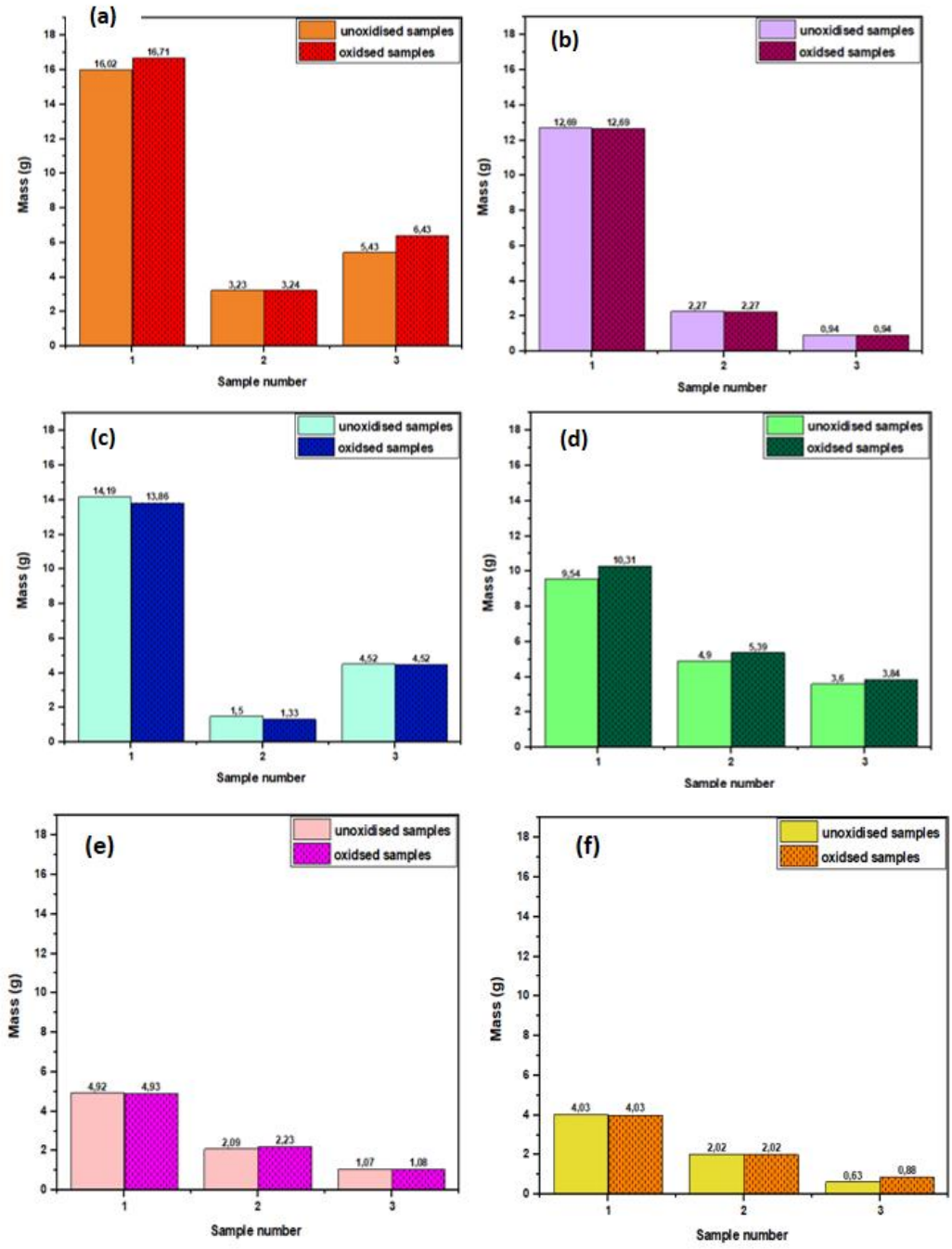


Figure 4.24: The mass change of samples a, b, c, d, e, and f at 1000˚C for 200h.

Table 4.9: The average mass change per surface area.

Sample ID	Average mass change per surface area (g/m^2)
a	0.6
b	0
c	1.7
d	0.5
e	0.01
f	0.01

Figure 4.25 represents the XRD pattern of AlCrCoCuFeNi-HEA at different scanning speed after oxidation. For all oxidation times FCC, BCC and Fe_2O_3 peaks were identified. The Fe_2O_3 oxide peaks intensified with an increase in laser power and scanning speed, indicating the growth of an external scale. Fe_2O_3 phases often form a non-protective oxide layer (Saha, 2020; Butler and Weaver, 2016a).

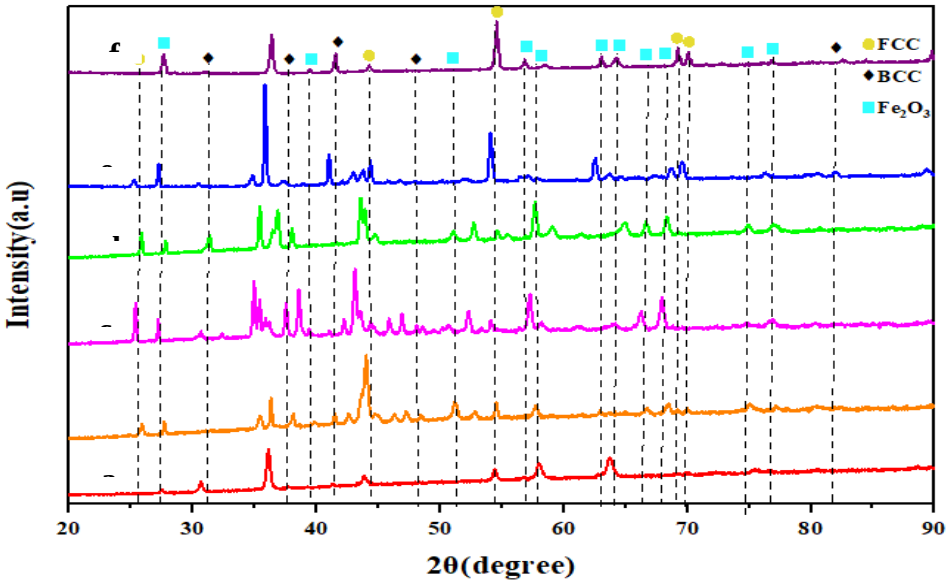


Figure 4.25: XRD spectrum of oxidized samples after 200 hours.

Figure 4.26 represents the surface micrographs of AlCrCoCuFeNi-HEA at different laser power and scan speed after 200h of oxidization. The oxide film in **Figure 4.26** displays surface morphologies that appear to have a compact structure with flake-like oxide films. Sample e and f

exhibit nodules with rough oxide crystallites. The oxide films was not tenacious at high laser power and scan seed (sample e and f).

Although the oxide layer provides a certain degree of protection by serving as a physical barrier between the metal and the surroundings, is often porous and can facilitate more oxidation beneath it. The ongoing process of oxidation beneath the oxide layer might result in the layer cracking or peeling off, which exposes new metal surfaces to the environment and leads to continuous corrosion (Yardley, 2017).

Cracks are distinguishable on the oxide surface, as indicated by the arrows. The phase analysis shows that the oxidation products in the oxide film was dominantly Fe_2O_3 oxide compounds because of the high Fe content in the powder. The following oxides Al_2O_3, Cr_2O_3 and Fe_2O_3 are mechanically, thermodynamically, and chemically stable. Yang *et al*. (2018) reviewed the oxidation behaviour of metallic materials and the application and mechanism of oxide coatings. In particular, the authors discuss the mechanical, thermodynamic, and chemical stability of various oxide coatings, including Al_2O_3, Cr_2O_3, and Fe_2O_3. The authors concluded that these oxides are stable and have been widely used as protective coatings under different conditions due to their properties.

The Al_2O_3, is renowned for its ability to create a protective oxide layer on aluminium and related alloys. The oxide layer functions as a protective barrier, preventing any additional oxidation or corrosion of the underlying material. It offers stability and protection against various environmental elements (Sukiman *et al*., 2012).Cr_2O_3, develops a thin, stable, and protective oxide layer. The presence of this layer offers exceptional protection against corrosion and oxidation in various environments, contributing to the durability and lifespan of the material (Peltier and Thierry, 2022). Fe_2O_3, has the ability to create a protective oxide layer under specific condition. However, the effectiveness of Fe_2O_3 scales in providing protection can differ based on the environmental condition. Their defensive capabilities may prove less efficient in some hostile environment, such as oxidation at high temperatures or when exposed to specific corrosive substances (Gurrappa, Malakondaiah, 2008).

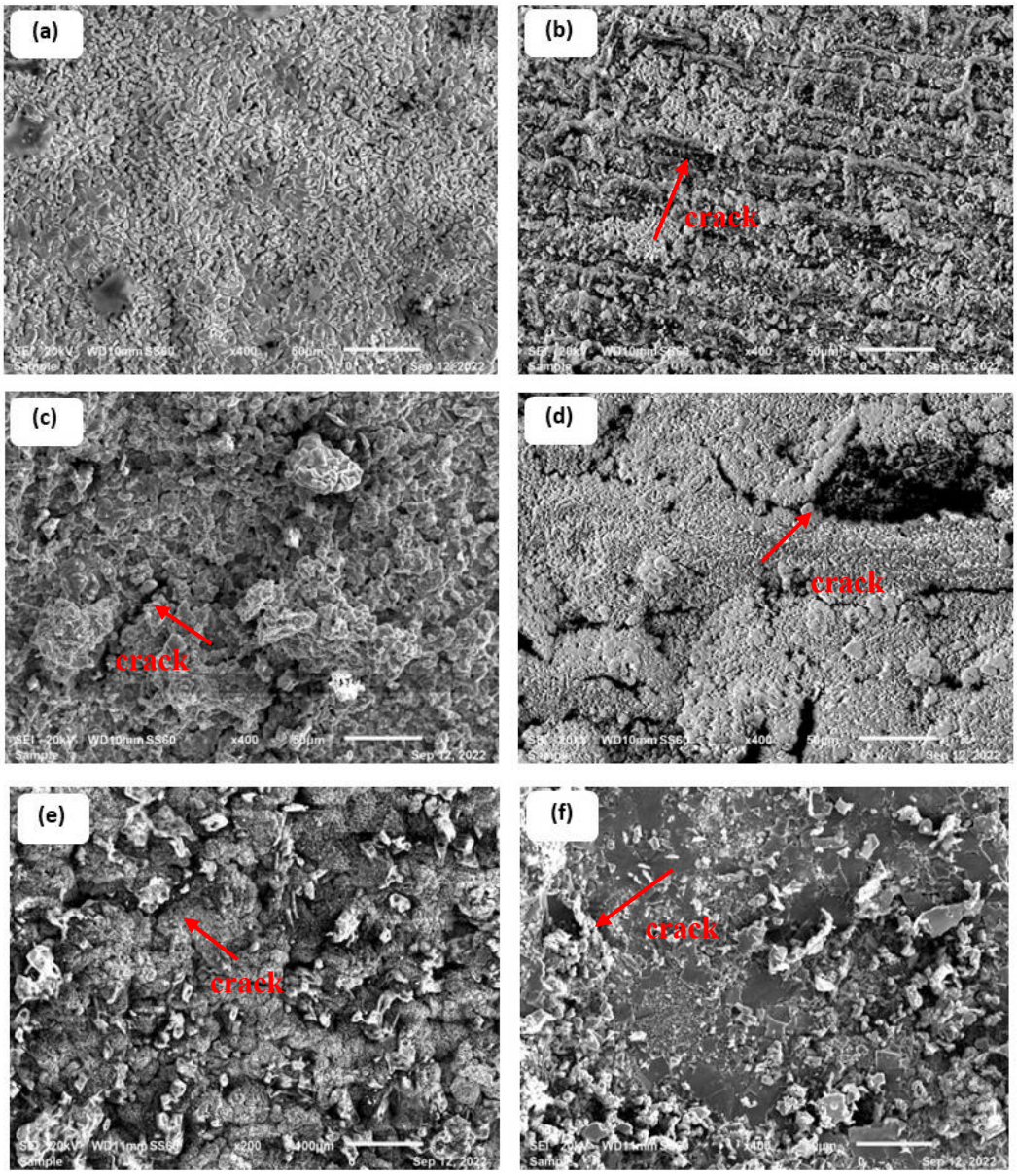


Figure 4.26: SEM surface images of AlCrCoCuFeTi-HEA after oxidising for 200h.

Therefore, the findings from the isothermal oxidation tests conducted on AlCrCoCuFeNi-HEA samples at a temperature of 1000°C for a duration of 200 hours. Highlights the non-protective characteristics exhibited by the predominant Fe_2O_3 oxide scale. The variation of laser power and scan speed during the fabrication process of materials has a significant impact on the formation of the alloy and its oxide scale. The findings of this study indicate that AlCrCoCuFeNi-HEA does

not demonstrates superior resistance to oxidation at elevated temperatures, this is due to the formation of oxide layer during the oxidation process.

Chapter 5
Conclusion and Recommendations

This chapter presents the characterisation of AlCrCoCuFeNi-HEA samples fabricated using DED techniques, utilising a range of analytical techniques. This study evaluated the fundamental characteristics of AlCrCoCuFeNi-HEA samples by determining the mechanical properties, post-processing methods, and high-temperature oxidation properties.

5.1 Conclusion

The parameter development using density found that lower laser power gave rise to a decreased relative density and higher laser power produced samples with relatively high densities for the DED AlCrCoCuFeNi-HEA.

The increase in scanning speed during the manufacturing process of the alloy resulted in rapid cooling, leading to the presence of both FCC and BCC phases in the as-built AlCrCoCuFeNi-HEA crystal structure.

AlCrCoCuFeNi-HEA display a combination of crystal structures, commonly incorporating BCC phases. The fine-grain microstructure in the alloy, combined with multiple elements in near-equimolar proportion can significantly contribute to their hardness. The inclusion of different crystal structures form grain boundaries which can enhance mechanical properties, such as hardness, potentially making them stronger than conventional alloys. The microstructures showed equiaxed grains with some cracking on the grain boundaries. The findings suggest that adjusting different process parameters during fabrication can potentially minimise the occurrence of intergranular cracks, therefore improving the overall integrity and quality of the material. Modifying these parameters could potentially regulate the formation of cracks and enhance the material structural integrity. Therefore, the overall study appears to have made significant progress

in adjusting parameters for the manufacturing of AlCrCoCuFeNi-HEA with properties suitable for aerospace applications.

Direct energy deposition is characterised by the significant role it plays in the production of complex parts. However, the surface finish remains a challenge. In this experimental study, centrifugal barrel finishing and electropolishing have been implemented to improve the surface finish of the direct energy deposited parts at different laser power and scan speeds.

The AlCrCoCuFeNi-HEA samples, which were electropolished at a laser power of 1200W for a duration of 30 seconds, exhibited a surface reducyion of 50.29% for sample a, 58.65% for sample b, and 75.48% for sample c. The surface removal at 60 sec on sample d is 50.29%, e is 45%, f is 49.19%. The best polishing results were achieved by sample c. This was not comparable to the required surface roughness values of 0.8 μm < Ra < 1.6 μm for application in the aerospace industry. However, there was great improvement in the surface roughness for AlCrCoCuFeNi-HEA. With an improvement in the electrolyte, time, and polishing media, a more ideal surface roughness can be achieved.

In centrifugal barrel finishing the samples were polished for 14 hours and 7 hours. At 14 hours, the polishing process has been found to produce an improved Ra surface finishing on the alloy where the total reduction Ra from a is 55.37%, b is 43.13%, and c is 32.2%. Conversely, there were embedded scratches due to the rubbing and deburring of the ceramic media therefore, in the second phase (7 hours) the use of a less abrasive media (plastic and zirconia balls) was implemented to counteract the embedded scratches that were caused in the first phase. An improved surface was observed with a total Ra reduction of d is 86.02%, e is 43.18%, and f is 90%. The best surface reduction obtained for the CBF method was sample f, the removal rate is sufficient for industrial applications.

This work has demonstrated that EP and CBF have the potential to be effective methods for improving the surface finish of additively manufactured AlCrCoCuFeNi-HEA alloys.

The study highlights the significance of the formation of oxide layers that act as a non-protective layer in high temperatures. Although oxidation takes place, the oxide layers that are primarily composed of Fe_2O_3 do not successfully protect the alloy from further oxidation in high temperatures. By manipulating the laser parameters throughout the manufacturing process, it is

possible to influence the composition and characteristics of both the alloy and the resulting oxide scales.

The following conclusions were made:

- The high entropy alloy 25 mm x 25 mm x 15 mm samples were successfully fabricated.
- The microstructure is predominantly composed of equiaxed grains, with noticeable intergranular cracking observed at higher laser power. `
- The presence of fine grains has a beneficial effect on the hardness of the material, as evidenced by hardness values ranging from 299 to 563 HV, notably higher at lower speeds.
- In centrifugal barrel finishing the removal fraction was influenced by the media selection, high laser power, and scan speed. The best polishing results were obtained at 1400W for 0.72mm/s.
- In electropolishing the surface removal is influenced by low laser power at high scan speed. The best polishing results were achieved at 1200W and 0.72mm/s for 30 sec using a Struers LectroPol-5 polishing machine.
- The centrifugal barrel finishing is the preferred post-processing treatment because of the exceptional surface quality and reduced imperfections which make it a potential candidate for post-treatment.
- High-temperature oxidation of AlCrCoCuFeNi-HEA at 1000˚C for 200h formed dominant Fe_2O_3 scales, which do not demonstrate resistance to oxidation at high temperatures due to the formation of oxide layers during the oxidation process.

5.2 Recommendations

During the build-up of HEA on direct energy deposited process:

- A flexible processing chamber is required to prevent high argon consumption, which limits the movement and inclination of the powder nozzle.
- Use a thicker substrate to avoid defects on the sample.
- Appropriately sized powder particles (45-150 μm) should be used on the Kuka robot.

For Post-processing

- The use of less abrasive media, such as zirconia balls, during centrifugal barrel finishing is required to prevent scratches.
- Improve the concentrations of the electrolyte to obtain a better surface finish during electropolishing.
- Increasing the polishing range at a constant time to observe the polishing trend.
- The comparable use of different electrolytes to observe the behaviour of materials.

High-temperature oxidation

- Determine the high-temperature oxidation rate at different time intervals and temperatures.
- The need for additional investigation and refinement of laser parameters to improve the oxidation resistance of the HEA.

References

Aboulkhair, N. T., Simonelli, M., Parry, L., Ashcroft, I., Tuck, C. and Hague, R. 2019. 3D printing of Aluminium alloys: Additive Manufacturing of Aluminium alloys using selective laser melting. Progress in Materials Science, 106, p.100578.

Adelkhani, H., Nasoodi, S. and Jafari, A. 2009. A study of the morphology and optical properties of electropolished aluminum in the Vis-IR region. International Journal of Electrochem Sciences, 4, p.238-246.

Aksu, Y., Erdogan, M., Demirci, G. and Karakaya, I., 2016. Electropolishing of an Fe-Ni-Co alloy in acetic acid-perchloric acid mixture. Electrochemical Society Transactions, 72(22), p.13.

Alateyah, A.I., Alawad, M.O., Aljohani, T.A. and El-Garaihy, W.H., 2022. Influence of ultrafine-grained microstructure and texture evolution of ECAPed ZK30 magnesium alloy on the corrosion behavior in different corrosive agents. Materials, 15(16), p.5515.

Arshad, M., Amer, M., Hayat, Q., Janik, V., Zhang, X., Moradi, M. And Bai, M., 2022. High-Entropy Coatings (HEC) for high-temperature applications: Materials, Processing, and Properties. Coatings, 12(5), p.691.

Bahtiar, M. A. 2016. Nano Polishing of Titanium Alloy with Ionic Liquid. Universiti Teknologi Petronas. http://utpedia.utp.edu.my/id/eprint/16880.

Bhat, B.N., Pandey, A.B., Tamirisakandala, S., Nathal, M.V., Ellis, D.L., McGill, P.B., Lee, J.A., Davis, S.E., Koo, J., Nettles, A. and Zhu, D., 2018. Aerospace materials characteristics (No. M17-6171). American Institute of Aeronautics and Astronautics.

Blakey-Milner, B., Gradl, P., Snedden, G., Brooks, M., Pitot, J., Lopez, E., Leary, M., Berto, F. and Du Plessis, A., 2021. Metal additive manufacturing in aerospace: A review. Materials and Design, 209, p.110008.

Blanco, D., Rubio, E.M., Sáenz de Pipaón, J.M. and Marín, M.M., 2020. Thicknesses/roughness relationship in Mg-Al-Mg and Mg-Ti-Mg hybrid component plates for drilled aeronautical lightweight parts. Applied Sciences, 10(22), p.8208.

Boschetto, A., Bottini, L., Macera, L. and Veniali, F. 2020. Post-processing of complex SLM parts by barrel finishing. Applied Sciences, 10, p.1382.

Butler, T. M. and Weaver, M. L. 2016a. Influence of annealing on the microstructures and oxidation behaviors of Al8 (CoCrFeNi) 92, Al15 (CoCrFeNi) 85, and Al30 (CoCrFeNi) 70 high-entropy alloys. Metals, 6, p.222.

Butler, T.M. and Weaver, M.L. 2016, "Oxidation behavior of arc melted AlCoCrFeNi multi-component high-entropy alloys", Journal of Alloys and Compounds, vol. 674, p.229-244.

Butler, T.M., Alfano, J.P., Martens, R.L. and Weaver, M.L. 2015, "High-temperature oxidation behavior of Al-Co-Cr-Ni-(Fe or Si) multicomponent high-entropy alloys", The Journal of The Minerals, Metals and Materials Society, vol. 67, p.246-259.

Campbell, I., Diegel, O., Kowen, J. and Wohlers, T., 2018. Wohlers report 2018: 3D printing and additive manufacturing state of the industry: annual worldwide progress report.

Cao, J., Zhang, J., Hua, Y., Chen, R., Li, Z. and Ye, Y. 2017. Microstructure and hot corrosion behavior of the Ni-based superalloy GH202 treated by laser shock processing. Materials Characterisation, 125, p.67-75.

Chaghazardi, Z. and Wüthrich, R. 2022, Electropolishing of additive manufactured metal parts, Journal of the Electrochemical Society,169(4), p.043510.

Chai, R., Zhang, Y., Zhong, B. and Zhang, C., 2021. Effect of scan speed on grain and microstructural morphology for laser additive manufacturing of 304 stainless steel. Reviews on Advanced Materials Science, 60(1), p.744-760.

Chen, H.S., Tsai, C.W., Tung, C.C., Yeh, L.W., Shun, T.T., Yang, C.C. And Chen, S.K., 2006, November. Effect of the substitution of Co by Mn in Al-Cr-Cu-Fe-Co-Ni high entropy alloys. In Annales De Chimie-Science Des Materiaux 31(6) p.685-698.

Chen, X.H. And Yan, H., 2016. Solid–liquid interface dynamics during solidification of Al 7075–Al2O3 based metal matrix composites. Materials and Design, 94, p.148-158.

Chen, Y.Y., Duval, T., Hung, U.D., Yeh, J.W. And Shih, H.C., 2005. Microstructure and electrochemical properties of high entropy alloys a comparison with type-304 stainless steel. Corrosion Science, 47(9), p.2257-2279.

Chen, Z., Lu, Y., Luo, F., Zhang, S., Wei, P., Yao, S. and Wang, Y. 2022, Effect of laser scanning speed on the microstructure and mechanical properties of laser-powder-bed-fused K418 nickel-based alloy, Materials, 15(9), p.3045.

Cheng, K.H., Lai, C.H., Lin, S.J. and Yeh, J.W., 2006. Recent progress in multi-element alloy and nitride coatings sputtered from high-entropy alloy targets. In Annales de chimie (Paris. 1914) 31(6), p. 723-736.

Chikumba, S. and Rao, V.V., 2015, November. High entropy alloys: development and applications. In Proceedings of the 7th International Conference on Latest Trends in Engineering & Technology (ICLTET'2015) p. 1-5.

Chou, H.P., Chang, Y.S., Chen, S.K. and Yeh, J.W. 2009. Microstructure, thermophysical and electrical properties in AlxCoCrFeNi ($0 \leq x \leq 2$) high-entropy alloys. Materials Science and Engineering: B, 163, p.184-189.

Chowdhury, S., Yadaiah, N., Prakash, C., Ramakrishna, S., Dixit, S., Gupta, L.R. and Buddhi, D. 2022, Laser powder bed fusion: A state-of-the-art review of the technology, materials, properties and defects, and numerical modeling, Journal of Materials Research and Technology, 20, p. 2109-2172.

Chuang, M.H., Tsai, M.H., Wang, W.R., Lin, S.J. and Yeh, J.W., 2011. Microstructure and wear behavior of AlxCo1.5CrFeNi1. 5Tiy high-entropy alloys. Acta Materialia, 59(16), p.6308-6317.

Conner, B.P., Manogharan, G.P., Martof, A.N., Rodomsky, L.M., Rodomsky, C.M., Jordan, D.C. And Limperos, J.W., 2014. Making sense of 3-D printing: Creating a map of additive manufacturing products and services. Additive manufacturing, 1, p.64-76.

Conner, B.P., Manogharan, G.P., Martof, A.N., Rodomsky, L.M., Rodomsky, C. M., Jordan, D. C. and Limperos, J. W. 2014. Making sense of 3-D printing: Creating a map of additive manufacturing products and services. Additive Manufacturing, 1, p.64-76.

Costas Bosque, D., 2018. Characterization of high-entropy alloys: study of the addition of aluminum to the high entropy system HfMoTaTiAl (Bachelor's thesis, Universitat Politècnica de Catalunya).

Crouse, M. (2021) 'Military starts to run with 3D printing and additive manufacturing'. 28 June. Available at: https://www.militaryaerospace.com/home/article/14205856/military-starts-to-run-with-3d-printing-and-additive-manufacturing/ (Accessed: 6 August 2021)

Cui, W., Zhang, X. And Liou, F 2017. Additive manufacturing of high-entropy alloy. In Proceedings of the 28th Annual International Solid Freeform Fabrication Symposium–An Additive Manufacturing Conference, p. 712-724.

Dada, M., Popoola, P., Adeosun, S. and Mathe, N. 2019, High entropy alloys for aerospace applications in Aerodynamics IntechOpen. p.74-174

Dada, M., Popoola, P., Mathe, N., Pityana, S. and Adeosun, S. 2021a. Effect of laser parameters on the properties of high entropy alloys: A preliminary study. Materials Today: Proceedings, 38, p.756-761.

Dada, M., Popoola, P., Mathe, N., Pityana, S., Adeosun, S. and Aramide, O. 2021b. The comparative study of the microstructural and corrosion behaviour of laser-deposited high entropy alloys. Journal of Alloys and Compounds, 866, p.158777.

Dada, M., Popoola, P., Mathe, N., Pityana, S., Adeosun, S. and Lengopeng, T. Fabrication and hardness behaviour of high entropy alloys. TMS 2020 149th Annual Meeting and Exhibition Supplemental Proceedings, 2020b. p.1581-1591.

Dada, M., Popoola, P., Mathe, N., Pityana, S., Adeosun, S., Aramide, O. and Lengopeng, T. 2020a. Process optimization of high entropy alloys by laser additive manufacturing. Engineering Reports, 2, p.12252.

Daoud, H. M., Manzoni, A. M., Völkl, R., Wanderka, N. and Glatzel, U. 2015. Oxidation Behavior of Al8Co17Cr17Cu8Fe17Ni33, Al23Co15Cr23Cu8Fe15Ni15, and Al17Co17Cr17Cu17Fe17Ni17 Compositionally complex alloys (high-entropy alloys) at elevated temperatures in air. Advanced Engineering Materials, 17, p.1134-1141.

De Beer, D., Becker, L., Van Der Walt, P., Mauchline, D., Campbell, I. And Dean, L. 2012. Additive manufacturing of aluminide jewelry.

Debroy,T., Wei, H., Zuback, J., Mukherjee, T., Elmer, J., Milewski, J., Beese, A. M., Wilson-Heid, A. D., De, A. and Zhang, W. 2018. Additive manufacturing of metallic components–process, structure and properties. Progress in Materials Science, 92, p.112-224.

Dewangan, S.K., Mangish, A., Kumar, S., Sharma, A., Ahn, B. and Kumar, V. 2022a, "A review on high-temperature applicability: A milestone for high entropy alloys", Engineering Science and Technology, an International Journal, p. 101211.

Dilberoglu, U. M., Gharehpapagh, B., Yaman, U. and Dolen, M. 2017. The role of additive manufacturing in the era of Industry 4.0. Procedia Manufacturing, 11, p.545-554.

Ding, C., Cui, X., Jiao, J. and Zhu, P. 2018a, "Effects of substrate preheating temperatures on the microstructure, properties, and residual stress of 12CrNi2 prepared by laser cladding deposition technique", Materials, 11(12), p. 2401.

Ding, D., Pan, Z., Cuiuri, D. and Li, H. 2015. Wire-feed additive manufacturing of metal components: technologies, developments and future interests. The International Journal of Advanced Manufacturing Technology, 81, p.465-481.

Dmitriyev,S., Koudrin, A., Labunets, A. and Kindrachuk, M. 2005. Functional coatings application for strengthening and restoration of aviation products. Aviation, 9, p.39-45.

Dobbelstein,H., Gurevich, E.L., George, E.P., Ostendorf, A. and Laplanche, G. 2018. Laser metal deposition of a refractory TiZrNbHfTa high-entropy alloy. Additive Manufacturing, 24, p.386-390.

Dobbelstein,H., Gurevich, E.L., George, E.P., Ostendorf, A. and Laplanche, G. 2019. Laser metal deposition of compositionally graded TiZrNbTa refractory high-entropy alloys using elemental powder blends. Additive Manufacturing, 25, p.252-262.

Enneti, R.K., Morgan, R. And Atre, S.V., 2018. Effect of process parameters on the Selective Laser Melting (SLM) of tungsten. International Journal of Refractory Metals and Hard Materials, 71, p.315-319.

Frazier, W.E. 2014. Metal additive manufacturing: a review. Journal of Materials Engineering and performance, 23, p.1917-1928.

Freire, B., Babcinschi, M., Ferreira, L., Señaris, B., Vidal, F. and Neto, P. 2020. direct energy deposition: a complete workflow for the additive manufacturing of complex shape parts. Procedia Manufacturing, 51, p.671-677.

Monroe, F.C., 2020. Effects of Phase Decomposition on the Strength of CoCrFeMnNi High Entropy Alloy (Doctoral dissertation, Clemson University).

Gateway, N.L. 2016. Wire feed additive manufacturing. Inside Metal Additive Manufacturing [Online].12 February 2016. Available from: https://www.insidemetaladditivemanufacturing.com/blog/wire-feed-additive-manufacturing [Accessed 10 May 2022].

Gelnar, D., Jezerska, L., Rozbroj, J., Zegzulka, J., Necas, J. and Ramirez-Gomez, A., 2018. Internal friction angle of metal powders. Metals 8(4), p.2075-4701.

Gibson, I., Rosen, D., Stucker, B., Gibson, I., Rosen, D. and Stucker, B., 2015. Directed energy deposition processes. Additive manufacturing technologies: 3D printing, rapid prototyping, and direct digital manufacturing, p.245-268.

Gleeson, B. 2010, "1.09-Thermodynamics and theory of external and internal oxidation of alloys", Shreir's corrosion, p.180-194.

Glicksman, M. E. 2011. principles of solidification an introduction to modern casting and crystal growth concepts. Springer Link. https://link.springer.com/book/10.1007/978-1-4419-7344-3

Gokuldoss, P.K., Kolla, S. and Eckert, J. 2017. Additive manufacturing processes: Selective laser melting, electron beam melting and binder jetting. Materials, 10, p.672.

Gong, H., Rafi, K., Gu, H., Starr, T. and Stucker, B. 2014. Analysis of defect generation in Ti–6Al–4V parts made using powder bed fusion additive manufacturing processes. Additive Manufacturing, 1, p.87-98.

Gorr, B., Azim, M., Christ, H.-J., Mueller, T., Schliephake, D. and Heilmaier, M. 2015. Phase equilibria, microstructure, and high-temperature oxidation resistance of novel refractory high-entropy alloys. Journal of Alloys and Compounds, 624, p.270-278.

Gu, D. and Shen, Y. 2009. Balling phenomena in direct laser sintering of stainless-steel powder: Metallurgical mechanisms and control methods. Materials and Design, 30, p.2903-2910.

Guo, J., Goh, M., Zhu, Z., Lee, X., Nai, M.L.S. and Wei, J. 2018. On the machining of selective laser melting CoCrFeMnNi high-entropy alloy. Materials and Design, 153, p.211-220.

Gurrappa, I. and Malakondaiah, G. 2008, "Effect of environment on corrosion characteristics of newly developed DMR-1700 structural steel", Science and technology of advanced materials, 9(2) p. 255.

Habibzadeh,S.,Shum-Tim, D.,Davis, E. C. and Omanovic, S. 2014, . Electrochemical polishing as a 316L stainless steel surface treatment method: Towards the improvement of biocompatibility. Corrosion Science 87, p.89–100.

Han, W. and Fang, F. 2019. Fundamental aspects and recent developments in electropolishing. International Journal of Machine Tools and Manufacture, 139, p.1-23.

Hassen, A. A. Noakes, M., Nandwana, P., Kim, S., Kunc, V., Vaidya, U., Love, L. and Nycz, A. 2020. Scaling Up metal additive manufacturing process to fabricate molds for composite manufacturing. Additive Manufacturing, 32, p.101093.

Heralic, A. 2012. Monitoring and Control of Robotized Laser Metal-Wire Deposition (Publication No. 27752856.) [University West]. https://www.proquest.com/openview/15e4cd024311b9ab6694ca8281ab49b2/1?pq-origsite=gscholar&cbl=18750&diss=y

Hong, S., Li, J., Zhao, P., Xu, Y. and Li, W. 2022, "Evolution in wear and high-temperature oxidation resistance of laser-clad AlxMoNbTa refractory high-entropy alloys coatings with Al addition content", Coatings, 12(2), p. 121.

Huang, C., Chen, Y. and Chang, J. 2008. The electrochemical polishing behavior of the Inconel 718 alloy in perchloric–acetic mixed acids. Corrosion Science, 50, P.480-489.

Huang, L. 2022. Everything You Need to Know About Polishing Surface Finish [Online]. Rapid Direct. Available: https://www.rapiddirect.com/blog/polishing-surface-finish [Accessed 24 March 2022].

Huang, W., Li, Y., Yanjie, R., Sun, J., Xia, Z., Zhou, L., Li, C., Chen, J., Niu, Y. and Zhao, Y. 2022. Effect of scanning speed on the high-temperature oxidation resistance and mechanical properties of Inconel 625 alloys fabricated by selective laser melting. Vacuum, 206, P.111447.

Huang, Y.S. 2009. Recent patents on high-entropy alloy. Recent Patents on Materials Science, 2, P.154-157.

Ingrassia, T., Nigrelli, V., Ricotta, V. And Tartamella, C., 2017. Process parameters influence in additive manufacturing. In advances on mechanics, design engineering and manufacturing: Proceedings of the international joint conference on mechanics, Design Engineering and Advanced Manufacturing, p. 261-270.

Jia, W., Zhao, H., Hong, Q., Li, L. And Mao, X., 2016. Research on the thermal stability of a near α titanium alloy before and after laser shock peening. Materials Characterization, 117, p.30-34.

Jiang, J., Xiao, G., Wang, Y. and Liu, Y. 2019. High-temperature oxidation behavior of the wrought Ni-based superalloy GH4037 in the solid and semi-solid state. Journal of Alloys and Compounds, 784, p.394-404.

Jiao, Z., Wang, Q., Yin, F. and Cui, C. 2019. Special corrosion behavior of an inoculant refined Cu-Al-Mn shape memory alloy during electropolishing process. Materials Characterization, 153, p.348-353.

Polychronis, K. 2002. A sub-process approach of selective laser sintering. https://doi.org/10.5075/epfl-thesis-2506

Karunakaran, K., Suryakumar, S., Pushpa, V. and Akula, S. 2010. Low cost integration of additive and subtractive processes for hybrid layered manufacturing. Robotics and Computer-Integrated Manufacturing, 26, p.490-499.

Kaschel, F.R., Celikin, M. and Dowling, D.P. 2020, "Effects of laser power on geometry, microstructure and mechanical properties of printed Ti-6Al-4V parts", Journal of Materials Processing Technology, 278, p. 116539.

Kaynak, Y. and Kitay, O. 2019. The effect of post-processing operations on surface characteristics of 316L stainless steel produced by selective laser melting. Additive Manufacturing, 26, p.84-93.

Ke, R., Hu, C., Zhong, M., Wan, X. and Wu, K. 2022, "Grain refinement strengthening mechanism of an austenitic stainless steel: critically analyze the impacts of grain interior and grain boundary", Journal of Materials Research and Technology, 17, p. 2999-3012.

Khana., Patidar, M., Petare, A., Chouhan, R., Chouhan, P., Vishwakarma, B., Sharma, U., Kaushal, S., Dhepte, D. and Madhukar, Y. 2020. Development of barrel finishing machine to improve surface finish of the wire arc additive manufactured parts. Procedia CIRP, 91, p.330-335.

King, W., Anderson, A. T., Ferencz, R. M., Hodge, N. E., Kamath, C. and Khairallah, S. A. 2015. Overview of modeling and simulation of metal powder bed fusion. Materials Science and Technology, 31, p.957-968.

Kobryn, P.A., Ontko, N.R., Perkins, L.P. And Tiley, J.S., 2006. Additive manufacturing of aerospace alloys for aircraft structures. Air Force Research Lab Wright-Patterson AFB OH Materials and Manufacturing Directorate.

Kok, Y., Tan, X.P., Wang, P., Nai, M.L.S., Loh, N.H., Liu, E. And Tor, S.B., 2018. Anisotropy and heterogeneity of microstructure and mechanical properties in metal additive manufacturing: A critical review. Materials and Design, 139, p.565-586.

Kouprianoff, D., Yadroitsava, I., Du Plessis, A., Luwes, N. and Yadroitsev, I. 2021, "Monitoring of laser powder bed fusion by acoustic emission: Investigation of single tracks and layers", Frontiers in Mechanical Engineering, 7, p. 678076.

Kumar, A. And Das, M., 2021. Multiphysics simulation and experimental investigation of microtool fabricated by EMM. Materials and Manufacturing Processes, 36(13), p.1489-1500.

Abhinav, K. Suraj K. and Manas D. Parametric investigation of EP to enhance surface characteristics of maraging steel with organic electrolyte, 2021, available at research square [https://doi.org/10.21203/rs.3.rs-932299/v1].

Kumar, P. and Jain, N. K. 2020. Effect of material form on deposition characteristics in micro-plasma transferred arc additive manufacturing process. Journal of Manufacturing Science and Technology, 30, p.195-205.

Lalegani, M., Serjouei, A., Zolfagharian, A., Fotouhi, M., Moradi, M., Ariffin, M.K.A. and Bodaghi, M. 2022, A review on additive/subtractive hybrid manufacturing of directed energy deposition (DED) process, Advanced Powder Materials, 1(4), p. 100054.

Lan, L., Wang, W., Cui, Z. And Hao, X., 2023. Effect of scanning speed on microstructure and mechanical properties of selective laser melting AlCoCrFeNi2. 1 eutectic high-entropy alloy. Materials Letters, 330, p.133321.

Landolt, D., Chauvy, P. F. and Zinger, O. 2003. Electrochemical micromachining, polishing and surface structuring of metals: fundamental aspects and new developments. Electrochimica Acta, 48, p.3185-3201.

Lee, H.K. 2008. Effects of the cladding parameters on the deposition efficiency in pulsed Nd: YAG laser cladding. Journal of Materials Processing Technology, 202, p.321-327.

Li, G., Li, X., Guo, C., Zhou, Y., Tan, Q., Qu, W., Li, X., Hu, X., Zhang, M.-X. and Zhu, Q. 2022. Investigation into the effect of energy density on densification, surface roughness and loss of alloying elements of 7075 aluminum alloy processed by laser powder bed fusion. Optics and Laser Technology, 147, p.107621.

Li, J., Huang, Y., Meng, X. and Xie, Y. 2019. A review on high entropy alloys coatings: fabrication processes and property assessment. Advanced Engineering Materials, 21, p.1900343.

Li, J., Jia, W., Wang, J., Kou, H., Zhang, D. and Beaugnon, E., 2016. Enhanced mechanical properties of a CoCrFeNi high entropy alloy by supercooling method. Materials and Design, 95, p.183-187.

Li, J., Zhang, C., Chen, C., Wei, Q., Zhang, Y., Cui, Y., and Sun, J. 2019. Microstructure and mechanical properties of AlCrCoCuFeNi high entropy alloy fabricated by directed energy deposition. Materials and Design, 166, p.107584.

Liang, G., Ali, Y., You, G. and Zhang, M. 2018, Effect of cooling rate on grain refinement of cast aluminum alloys, Materialia, 3, p.113-121.

Liu, S. and Guo, H. 2020, Balling behavior of selective laser melting (SLM) magnesium alloy, Materials, vol. 13, no. 16, pp. 3632.

Liu, T., Wang, Q., Cai, X., Pan, L., Li, J., Zong, Z., Cheng, Z., Tian, Z., Luo, L. and Su, Y. 2022, Effect of laser power on microstructures and properties of Al-4.82 Mg-0.75 Sc-0.49 Mn-0.28 Zr alloy fabricated by selective laser melting, Journal of Materials Research and Technology, 18, p.3612-3625.

Liu, T., Wang, Q., Cai, X., Pan, L., Li, J., Zong, Z., CheNG, Z., Tian, Z., Luo, L. and Su, Y. 2022. Effect of laser power on microstructures and properties of Al-4.82 Mg-0.75 Sc-0.49 Mn-0.28 Zr alloy fabricated by selective laser melting. Journal of Materials Research and Technology, 18, p3612-3625.

Liu, Y., Wang, F., Xu, D., Wang, J., Jiang, F., Zarinejad, M. and Tong, Y. 2023, Microstructure and mechanical properties of laser metal deposited Ti6Al4V alloy with near equiaxed β grain structure, Journal of Materials Research and Technology, 22, p.1935-1947.

Löber, L., Flache, C., Petters, R., Kühn, U. and Eckert, J., 2013. Comparison of different post processing technologies for SLM generated 316l steel parts. Rapid Prototyping Journal, 19(3), p.173-179.

Lu, J., Li, L., Chen, Y., Liu, X., Zhao, X., Guo, F. and Xiao, P. 2021. Y-Hf co-doped AlCoCrFeNi high-entropy alloy coating with superior oxidation and spallation resistance at 1100 ºC. Corrosion Science, 182, p.109267.

Lyczkowska, E., Szymczyk, P., Dybala, B. and Chlebus, E. 2014. Chemical polishing of scaffolds made of Ti-6Al-7Nb alloy by additive manufacturing. Archives of Civil and Mechanical Engineering, 14, p.586–594.

Machio, C., Machaka, R., Motsai, T., Chikosha, S. and Rossouw, P. 2018. Production of spherical titanium-based powders from powder metallurgy bars. RAPDASA 2018 Conference Proceedings.https://site.rapdasa.org/wp-content/uploads/2019/03/production-of-spherical-titanium-based-powders-from-powder-metallurgy-bars.pdf

Mahamood, R. and Akinlabi, E. 2017. Laser Power and Powder flow rate influence on the metallurgy and microhardness of Laser metal Deposited Titanium alloy. Materials Today: Proceedings, 4, p.3678-3684.

Mahamood, R.M. and Akinlabi, E.T. 2017, Laser Power and Powder flow rate influence on the metallurgy and microhardness of Laser metal Deposited Titanium alloy, Materials Today: Proceedings, 4(2), p. 3678-3684.

Manakari, V., Parande, G. and Gupta, M. 2016, Selective laser melting of magnesium and magnesium alloy powders: a review, Metals, 7(1), p. 2.

Markusson, L. (2017). Powder Characterization for Additive Manufacturing Processes [Luleå University of Technology]. https://www.diva-portal.org/smash/record.jsf?dswid=-7089&pid=diva2%3A1084670

Mate 2016. A Relationship between the microstructure and mechanical properties of an equiatomic AlCoCrFeNi high-entropy alloy fabricated by selective electron beam melting. Material Science and Engineering, 656, p.39-46.

Maurya, A. and Chauhan, P. 2011. Structural and optical characterization of CdS/TiO2 nanocomposite. Materials Characterization, 62, p.382-390.

Mazumder, J., 2017. Laser-aided direct metal deposition of metals and alloys. In Laser additive manufacturing , p. 21-53.

Mehta, R., Mehta, D. and Mehta, N. K. 2012. An exploratory study on implementation of lean manufacturing practices (with special reference to automobile sector industry). Yönetim ve Ekonom, 19, p.289-299.

Miracle, D. B., Miller, J. D., Senkov, O. N., Woodward, C., Uchic, M. D. and Tiley, J. 2014. Exploration and development of high entropy alloys for structural applications. Entropy, 16, p.494-525.

Mishra, R. K. and Shahi, R. R. 2018. Magnetic characteristics of high entropy alloys. Magnetism and Magnetic Materials, p.67-80.

Mohamed, A. M., Samuel, E., Zedan, Y., Samuel, A. M., Doty, H. W. and Samuel, F. H. 2022. Intermetallics Formation during Solidification of Al-Si-Cu-Mg Cast Alloys. Materials, p.15, 1335.

Murr, L. 2015. Metallurgy of additive manufacturing: Examples from electron beam melting. Additive Manufacturing, 5, p.40-53.

Murr, L.E., Martinez, E., Amato, K.N., Gaytan, S.M., Hernandez, J., Ramirez, D.A., Shindo, P.W., Medina, F. And Wicker, R.B., 2012. Fabrication of metal and alloy components by additive manufacturing: examples of 3D materials science. Journal of Materials Research and Technology, 1(1), p.42-54.

Najmon, J. C., Raeisi, S. and Tovar, A. 2019. Review of additive manufacturing technologies and applications in the aerospace industry. Additive Manufacturing for the Aerospace industry, p.7-31.

Nalli, F., Bottini, L., Boschetto, A., Cortese, L. and Veniali, F. 2020. Effect of industrial heat treatment and barrel finishing on the mechanical performance of Ti6AL4V processed by selective laser melting. Applied Sciences, 10, p.2280.

Niu, P., Li, R., Yuan, T., Zhu, S., Chen, C., Wang, M. and Huang, L. 2019. Microstructures and properties of an equimolar AlCoCrFeNi high entropy alloy printed by selective laser melting. Intermetallics, 104, p.24-32.

Nziu, P., Masu, L., Mendonidis, P. and Alungogo, A. 2014. Characterization of titanium powder flow: A review on current status on flowability. Sabinet African Journals, 11, p.239-255.

Otto, F., Dlouhý, A., Somsen, C., Bei, H., Eggeler, G. and George, E. P. 2013. The influences of temperature and microstructure on the tensile properties of a CoCrFeMnNi high-entropy alloy. Acta Materialia, 61, p.5743-5755.

Parimin, N. and Hamzah, E. 2020a. Oxide Growth Behaviour of Fe-Ni-Cr Alloy at High-Temperature Oxidation. IOP Conference Series: Materials Science and Engineering, IOP Publishing, p.012001.

Parimin, N. and Hamzah, E. Role of Alloyed niobium on the isothermal oxidation of Fe-40Ni-24Cr Alloy. Materials Science Forum, 2020b. Trans Tech Publications, p.79-85.

Parimin, N., Hamzah, E., Ahad, N. A. and Derman, M. N. Isothermal oxidation behaviour of 800h nickel-based alloy. Journal of Physics: Conference Series, 2022. IOP Publishing, p.012038.

Parry, L., Ashcroft, I. and Wildman, R. D. 2016. Understanding the effect of laser scan strategy on residual stress in selective laser melting through thermo-mechanical simulation. Additive Manufacturing, 12, p.1-15.

Peltier, F. and Thierry, D. 2022, Review of Cr-free coatings for the corrosion protection of aluminium aerospace alloys, Coatings, 12(4), p. 518.

Pereira, T., Kennedy, J.V. And Potgieter, J., 2019. A comparison of traditional manufacturing vs additive manufacturing, the best method for the job. Procedia Manufacturing, p.11-18.

Pircher, E., Martinez, M. R., Hansal, S. and Hansal, W. 2003. Electropolishing of copper alloys in phosphoric acid solutions with alcohols. Plating and Surface Finishing, 90, p.74-79.

Pouraliakbar, H., Shim, S. H., Kim, Y. K., Rizi, M. S., Noh, H. and Hong, S. I. 2021. Microstructure evolution and mechanical properties of (CoCrNi) 90 (AlTiZr) 5 (CuFeMo) 5 multicomponent alloy: A pathway through multicomponent alloys toward new superalloys. Journal of Alloys and Compounds, 860, p.158412.

Prasad, M.R., Gao, S., Vajragupta, N. and Hartmaier, A. 2020, Influence of trapped gas on pore healing under hot isostatic pressing in nickel-base superalloys, Crystals, 10(12) p. 1147.

Protomatic, 2015. Murr, L.E., Martinez, E., Amato, K.N., Gaytan, S.M., Hernandez, J., Ramirez, D.A., Shindo, P.W., Medina, F. and Wicker, R.B., 2012. Fabrication of metal and alloy components by additive manufacturing: examples of 3D materials science. Journal of Materials Research and Technology, 1(1), p.42-54.

Puma-Araujo, S., Olvera-Trejo, D., Elías-Zuñiga, A., Martínez-Romero, O. and Rodríguez, C. 2016. Design and characterization of a magnetorheological damper for vibration mitigation during milling of thin components. MRS Online Proceedings Library (OPL), 1812, p.65-70.

Qin, S., Bo, Y., Herzog, S., Hallstedt, B., Kaletsch, A. And Broeckmann, C., 2022. Influence of process parameters on porosity and hot cracking of AISI H13 fabricated by laser powder bed fusion. powders, 1(3), p.184-193.

Raines, A. L., Olivares-Navarrete, R., Wieland, M., Cochran, D. L., Schwartz, Z. and Boyan, B. D. 2010. Regulation of angiogenesis during osseointegration by titanium surface microstructure and energy. Biomaterials, 31, p.4909-4917.

ReCreate3D Printing. (2017) 3D Printing of digital models into physical objects. 24 August 2017. Available at; https://www.recreate3d.co.za/recreate3d-3d-printing/ (Accessed: 2 March 2022)

Recreate3dprinting. 2021. Printing of digital models into physical objects [Online]. Available: https://www.recreate3d.co.za/author/philipventermweb-co-za/ [Accessed 2 June 2021].

Riener, K., Albrecht, N., Ziegelmeier, S., Ramakrishnan, R., Haferkamp, L., Spierings, A. B. and Leichtfried, G. J. 2020. Influence of particle size distribution and morphology on the properties of the powder feedstock as well as of AlSi10Mg parts produced by laser powder bed fusion (LPBF). Additive Manufacturing, 34, p.101286.

Rodriguez, P., Ruiz, F., Dillard, J. and Tyagi, P. 2020. Electropolishing of surfaces in metallic parts obtained by Additive Manufacturing. https://engrxiv.org/preprint/view/868/

Sadeghi, E., Pant, P., Jafari, R., Peng, R. L. and Karimi, P. 2020. Subsurface grain refinement in electron beam-powder bed fusion of Alloy 718: Surface texture and oxidation performance. Materials Characterization, 168, p.110567.

Saha, M. 2020. Understanding the role of Al2O3 formed during isothermal oxidation in a dual phase AlCoCrFeNi2. Eutectic High-Entropy Alloy. Journal of Materials NanoScience, 7, p.68-72.

Serres, N., Tidu, D., Sankare, S. and Hlawka, F. 2011. Environmental comparison of MESO-CLAD® process and conventional machining implementing life cycle assessment. Journal of Cleaner Production, 19, p.1117-1124.

Sexton, L., Lavin, S., Byrne, G. and Kennedy, A. 2002. Laser cladding of aerospace materials. Journal of Materials Processing Technology, 122, p.63-68.

Sheasby, P.G., Pinner, R. And Wernick, S., 2001. The surface treatment and finishing of aluminum and its alloys Materials Park, OH: ASM International, l(1), p. 231.

Sheng, H., Gong, M. and Peng, L. 2013. Microstructural characterization and mechanical properties of an Al0. 5CoCrFeCuNi high-entropy alloy in as-cast and heat-treated/quenched conditions. Materials Science and Engineering: A, 567, p.14-20.

Sibisi, P.N., Popoola, A.P.I., Arthur, N.K. And Pityana, S.L., 2020. Review on direct metal laser deposition manufacturing technology for the Ti-6Al-4V alloy. The International Journal of Advanced Manufacturing Technology, p.1163-1178.

Sing, S.L., Tey, C.F., Tan, J.H.K., Huang, S. And Yeong, W.Y., 2020. 3D printing of metals in rapid prototyping of biomaterials: Techniques in additive manufacturing. In Rapid prototyping of biomaterials. Woodhead Publishing. p. 17-40.

Singh, N., Hameed, P., Ummethala, R., Manivasagam, G., Prashanth, K.G. and Eckert, J. 2020, Selective laser manufacturing of Ti-based alloys and composites: Impact of process parameters, application trends, and future prospects, Materials today advances, 8, p. 100097.

Singh, R., Gupta, A., Tripathi, O., Srivastava, S., Singh, B., Awasthi, A., Rajput, S.K., Sonia, P., Singhal, P. and Saxena, K.K. 2020, Powder bed fusion process in additive manufacturing: An overview, Materials Today: Proceedings, 26, p. 3058-3070.

Singh, R., Gupta, A., Tripathi, O., Srivastava, S., Singh, B., Awasthi, A., Rajput, S., Sonia, P., Singhal, P. and Saxena, K. K. 2020. Powder bed fusion process in additive manufacturing: An overview. Materials Today: Proceedings, 26, p.3058-3070.

Singleton, R. And Singleton, E., 2011. Fundamentals of barrel plating. Metal Finishing, 8(109), p.14-22.

Sistla, H. R., Newkirk, J. W. and Liou, F. F. 2015. Effect of Al/Ni ratio, heat treatment on phase transformations and microstructure of AlxFeCoCrNi2− x (x= 0.3, 1) high entropy alloys. Materials and Design, 81, p.113-121.

Sonkusare, R., Biswas, K., Al-Hamdany, N., Brokmeier, H.G., Kalsar, R., Schell, N. and Gurao, N.P. 2020, A critical evaluation of microstructure-texture-mechanical behavior heterogeneity in high-pressure torsion processed CoCuFeMnNi high entropy alloy, Materials Science and Engineering, 782, p.139187.

Spranger, F., Graf, B., Schuch, M., Hilgenberg, K. and Rethmeier, M. 2018. Build-up strategies for additive manufacturing of three-dimensional Ti-6Al-4V-parts produced by laser metal deposition. Journal of Laser Applications, 30, p.022001.

Sreehitha, V. 2017. Impact of 3D printing in automotive industry. International Journal of Mechanical and Production Engineering, 5, p.91-94.

Strano, G., Hao, L., Everson, R. M. and Evans, K. E. 2013a. Surface roughness analysis, modeling and prediction in selective laser melting. Journal of Materials Processing Technology, 213, p.589-597.

Sukiman, N.L., Zhou, X., Birbilis, N., Hughes, A.E., Mol, J., Garcia, S.J., Zhou, X. and Thompson, G.E. 2012, Durability and corrosion of aluminum and its alloys: overview, property space, techniques and developments, Aluminium Alloys-New Trends in Fabrication and Applications, 5, p.47-97.

Sun, F., Liu, P., Chen, X., Zhou, H., Guan, P. And Zhu, B., 2020. Mechanical properties of high-strength Cu–Cr–Zr alloy fabricated by selective laser melting. Materials, 13(21), p.5028.

Thompson, S., Bianc, L., Shamsaeia, N. and Yadollahi, A. 2015. An overview of direct laser deposition for additive manufacturing. Additive Manufacturing, 18, p.36-42.

Tlotleng, M., Masina, B. and Pityana, S. 2017. Characteristics of laser In-situ alloyed titanium aluminide coatings. Procedia Manufacturing, 7, p.39-45.

Tokarewicz, M. and Grądzka-Dahlke, M. 2021, Review of recent research on AlCoCrFeNi high-entropy alloy, Metals, 11(8), p. 1302.

Tokarewicz, M. and Grądzka-Dahlke, M. 2021. Review of recent research on alcocrfeni high-entropy alloy. Metals, 11, p.1302.

Tsai, K.Y., Tsai, M.H. and Yeh, J.W. 2013. Sluggish diffusion in Co–Cr–Fe–Mn–Ni high-entropy alloys. Acta Materialia, 61, p.4887-4897.

Tsai, M.H. and Yeh, J.W. 2014. High-entropy alloys: a critical review. Materials Research Letters, 2, p.107-123.

Tshabalala, L. C., Mathe, N. and Chikwanda, H. 2018. Characterization of gas atomized Ti-6Al-4V powders for additive manufacturing. Trans Technology Publication, p.3-8.

Tung, C.C., Yeh, J.W., Shun, T.T., Chen, S.K., Huang, Y.S. and Chen, H.C. 2007. On the elemental effect of AlCoCrCuFeNi high-entropy alloy system. Materials Letters, 61, p.1-5.

Ur Rahman, N., Matthews, D., De Rooij, M., Khorasani, A., Gibson, I., Cordova, L. and Romer, G. 2019. An Overview: Laser-Based Additive Manufacturing for High Temperature Tribology. Front. Mechanical Engineering 5, p.1-15.

Urlea, V. and Brailovski, V. 2017. Electropolishing and electropolishing-related allowances for powder bed selectively laser-melted Ti-6Al-4V alloy components. Journal of Materials Processing Technology, 242, p.1-11.

Vock, S., Klöden, B., Kirchner, A., Weißgärber, T. and Kieback, B. 2019. Powders for powder bed fusion: a review. Progress in Additive Manufacturing, 4, p.383-397.

Wall, I., Donos, N., Carlqvist, K., Jones, F. and Brett, P. 2009. Modified titanium surfaces promote accelerated osteogenic differentiation of mesenchymal stromal cells in vitro. Bone, 45, 17-26.

Wang, F., Zhang, Y., Chen, G. and Davies, H. 2009. Cooling rate and size effect on the microstructure and mechanical properties of AlCoCrFeNi high entropy alloy. Journal of Engineering Materials and Technology, p.131.

Wang, J., He, Q., Liu, G., Zhang, Q., Liu, G., Huang, Z., Zhu, X. and Fu, Y. 2021. High-Temperature Oxidation Behavior of AlTiNiCuCox High-Entropy Alloys. Materials, 14, p.5319.

Wang, Y., Li, R., Niu, P., Zhang, Z., Yuan, T., Yuan, J. and Li, K. 2020. Microstructures and properties of equimolar AlCoCrCuFeNi high-entropy alloy additively manufactured by selective laser melting. Intermetallics, 120, p.106746.

Wen, L., Kou, H., Li, J., Chang, H., Xue, X. and Zhou, L. 2009. Effect of aging temperature on microstructure and properties of AlCoCrCuFeNi high-entropy alloy. Intermetallics, 17, p.266-269.

Wong, K.V. and Hernandez, A. 2012, "A review of additive manufacturing", International scholarly research notices.

Xu, Y., Lu, J., Li, W. and Yang, X. 2018. Oxidation behaviour of Nb-rich Ni-Cr-Fe alloys: role and effect of carbides precipitates. Corrosion Science, 140, p.252-259.

Yadhuraj, S. and Kumari, U. Measurement of thickness and roughness using gwyddion. 2016 3rd International Conference on Advanced Computing and Communication Systems (ICACCS), 2016. IEEE, p.1-5.

Yadhuraj, S.R. and Kumari, U. 2016, Measurement of thickness and roughness using gwyddion, 2016 3rd International Conference on Advanced Computing and Communication Systems (ICACCS) IEEE, p. 1.

Yang, G., Xie, Y., Zhao, S., Qin, L., Wang, X. and Wu, B. 2022, Quality control: Internal defects formation mechanism of selective laser melting based on laser-powder-melt pool interaction: A review, Chinese Journal of Mechanical Engineering: Additive Manufacturing Frontiers, p. 100037.

Yang, J., Wan, Y., Li, Y., Li, X., and Zhang, T. (2018). A review of the oxidation behavior of metallic materials: application and mechanism of oxide coatings. Journal of Materials Science and Technology, 34(2), p.249-261.

Yardley, S., 2017. Oxidation mechanisms in zirconium alloys for nuclear applications (Doctoral dissertation, University of Oxford). https://ora.ox.ac.uk/objects/uuid:bb4776ae-60f7-49f1-b93f-9d1542e79431.

Yeh, J. W., Chen, S. K., Lin, S. J., Gan, J. Y., Chin, T. S., Shun, T. T., Tsau, C. H. and Chang, S. Y. 2004. Nanostructured high-entropy alloys with multiple principal elements: novel alloy design concepts and outcomes. Advanced Engineering Materials, 6, p.299-303.

Yeh, J. W., Chen, Y. L., Lin, S. J. and Chen, S. K. 2007. High-entropy alloys–a new era of exploitation. Materials Science Forum, Trans Technology Publication, p.1-9.

Yeh, J.W., 2016. Overview of high-entropy alloys. High-entropy alloys: fundamentals and applications, p.1-19.

Yu, J., Rombouts, M., Maes, G. and Motmans, F. 2012. Material properties of Ti6Al4 v parts produced by laser metal deposition. Physics Procedia, 39, p.416-424.

Yusuf, S. M. and Gao, N. 2017. Influence of energy density on metallurgy and properties in metal additive manufacturing. Materials Science and Technology, 33, p.1269-1289.

Yuting, L., Ding, Z., Sun, X., Li, L., Sha, G., Liu, R. and Wang, L. 2019. Gradient microstructures and mechanical properties of Ti-6Al-4V/Zn composite prepared by friction stir processing. Materials, 12, p.2795.

Zaraska, L., Stępniowski, W. J., Jaskuła, M. and Sulka, G. D. 2014. Analysis of nanopore arrangement of porous alumina layers formed by anodizing in oxalic acid at relatively high temperatures. Applied Surface Science, 305, p.650-657.

Zegzulka, J., Gelnar, D., Jezerska, L., Prokes, R. and Rozbroj, J. 2020. Characterization and flowability methods for metal powders. Scientific Reports, 10, p.1-19.

Zhai, Y., Lados, D. A. and Lagoy, J. L. 2014. Additive manufacturing: making imagination the major limitation. Jom, 66, p.808-816.

Zhang W, Ma Z, Li C, Guo C, Liu D, Zhao H, Ren L. 2022. Micro/nano-mechanical behaviors of individual FCC, BCC and FCC/BCC interphase in a high-entropy alloy. Journal of Materials Science and Technology. 1(114), p.102-10.

Zhang, M., Zhou, X., Wang, D., He, L., Ye, X. and Zhang, W., 2022. Additive manufacturing of in-situ strengthened dual-phase AlCoCuFeNi high-entropy alloy by selective electron beam melting. Journal of Alloys and Compounds, 893, p.162259.

Zhang, Y., Han, T., Xiao, M. and Shen, Y. 2020. Effect of iron content on microstructure and properties of FexNi2Co2CrTiNb high-entropy alloy coating. Optik, 204, p.164168.

Zhang, Y., Zuo, T. T., Tang, Z., Gao, M. C., Dahmen, K. A., Liaw, P. K. and Lu, Z. P. 2014. Microstructures and properties of high-entropy alloys. Progress in Materials Science, 61, p.1-93.

Zhao, Z., Li, J. and Jiang, Q. 2004. Hypereutectic Al-Si Binary Alloys Prepared by Melt Spinning Method. Advanced Engineering Materials, 6, p.303-306.

Zhou, L., Chen, S., Wei, M., Liang, J., Liu, C. and Wang, M. 2019, Microstructure and properties of 24CrNiMoY alloy steel prepared by direct laser deposited under different preheating temperatures, Materials Characterization, 158, p. 109931.

Abdulhameed, O., Al-Ahmari, A., Ameen, W. and Mian, S.H., 2019. Additive manufacturing: Challenges, trends, and applications. Advances in Mechanical Engineering, 11(2), p.1687814018822880.

Zhou, Y., Zhang, Y., Kim, T. and Chen, G. 2008. Microstructure characterizations and strengthening mechanism of multi-principal component AlCoCrFeNiTi0.5 solid solution alloy with excellent mechanical properties. Materials Letters, 62, P.2673-2676.

Zhou, Y., Zhang, Z., Wang, Y., Liu, G., Zhou, S., Li, Y., Shen, J. and Yan, M. 2019. Selective laser melting of typical metallic materials: An effective process prediction model developed by energy absorption and consumption analysis. Additive Manufacturing, 25, p.204-217.

Zhu, Y., Sun, K. and Frankel, G.S., 2018. Intermetallic phases in aluminium alloys and their roles in localized corrosion. Journal of The Electrochemical Society, 165(11), p.C807.

Appendix A: Angle of internal friction

Table A1

Powder	Cohesion kPa	UYS kPa	MPS kPa	MCS kPa	FF	Rel (p)	AIF º	BD g/ml
R01	0.226	0.850	14.9	3.98	17.5	12.9	34.0	2.82
R02	0.724	2.84	16.6	3.57	5.84	4.58	36.0	2.79
R03	0.338	1.21	14.5	4.11	11.9	8.52	31.7	2.80

Appendix B: Measured densities of AlCrCoCuFeNi-HEA using Archimedes principal.

Table B1

	Sample a	**Sample b**	**Sample c**	**Sample d**	**Sample e**	**Sample f**
1st measurement	6.7456	6,9165	6,9445	6,8158	6,551	6,4028
2nd measurement	6.7475	6,9177	6,9463	6,8183	6,5263	6,4863
3rd measurement	6.7485	6,9171	6,9471	6,8182	6,5531	6,4286
Average measure density [g/cm^3]	6,75	6,92	6,95	6,82	6,54	6,44

Appendix C: 2022 RAPDASA-RobMech-PRASA-CoSAAMI Conference

MATEC Web of Conferences **370**, 06007 (2022) https://doi.org/10.1051/matecconf/202237006007
2022 RAPDASA-RobMech-PRASA-CoSAAMI Conference

Post-processing of direct metal deposited AlCrCoCuFeNi HEA using centrifugal barrel finishing

Thembisile Modikwe[1*], *Nthabiseng* Maledi[1], *Ntombi* Mathe[2], *Sisa* Pityana[2], *Modupeola* Dada[3], *Washington* Makoana[2]

[1] School of Chemical and Metallurgical Engineering, University of the Witwatersrand, Private Bag 3, Wits, Johannesburg 2050, South Africa.
[2] Council for Scientific Industrial Research (CSIR), Manufacturing, National Laser Centre, Laser Enabled Manufacturing Group, P.O. Box 395, Pretoria 0001, South Africa.
[3] Department of Chemical, Metallurgical and Materials Engineering, Tshwane University of Technology, Staatsartillerie Rd, Pretoria West, Pretoria, 0183, South Africa.

Abstract. Stainless steels, Ni-based alloys, Ti-based alloys, and more recently high entropy alloys have been used in the aerospace industry to improve the exterior properties of components and coatings that require a fine surface finishing with over high temperature range. High- entropy alloys (HEA) have become a ground-breaking research field that provides solutions for structural/ functional materials in the aerospace industry. These alloys, fabricated via direct metal deposition, have better properties than those produced by arc melting. However, the poor surface finish acquired by the layer-by-layer laser deposition process fails to meet the industrial requirements. The implementation of surface treatment by centrifugal barrel finishing is employed to improve the surface roughness of AlCoCrCuFeNi laser deposited HEA. The results have shown a minimum surface roughness decrease of 40%. Thus, an improved surface finish was achieved.

1. Introduction

Conventional alloys such as Cu-based alloys, stainless steels, Ni-based alloys, and Ti-based alloys have been used for years but with time they have been found to have limitations, including restrictions in the number of possible compositions [27]. Today, High entropy alloys (HEA) are becoming a recognisable phenomenon in the material science fraternity. HEA is novel concept, designed to supersede conventional alloys' potential [4]. Aluminium alloys have been used over the years in aircraft engines by virtue of its low-density characteristics, but the inability to withstand high temperatures has limited its application [3]. Dada *et al.*[6] conducted a comparative microstructural and corrosion behaviour HEA study between AlCoCrFeNiCu and AlCoCrFeNiTi. The study revealed that even though Ti-based HEA displayed high corrosion resistance compared to Cu-based HEA, the resistance of both these alloys was still higher than that of traditional alloys. Yeh *et al.*[31] defined HEAs as metallic materials that consist of five or more principal elements in equiatomic or close to equiatomic atomic ratios, with an atomic percentage ranging between 5 % and 35 %. HEAs have become a ground-breaking research field that provides solutions to complex problems in the aerospace industry [28]. The industry requires improvement in the application of structural materials that are well-functioning at a low cost, for example, in turbine blades [3].

* Corresponding author: 673864@students.wits.ac.za

© The Authors, published by EDP Sciences. This is an open access article distributed under the terms of the Creative Commons Attribution License 4.0 (http://creativecommons.org/licenses/by/4.0/).

This results in the deployment of functional coatings, which are applications driven, particularly for surface protection resulting in an improved mechanical and chemical properties [18].

Environmental degradation of the surface subjected to high temperature, abrasion, fatigue, erosion, gas and hydro-abrasion etc. leads to surface wear damage, causing a reduction of the service life [10]. Laser surface cladding of HEA alloys has been shown to improve and/or enhance surface properties in tribological applications. Functional components by means of laser additive manufacturing (AM) using HEAs materials, have also been receiving great attention in recent times [20, 21]. The fabrication of metal parts obtained using laser-based additive manufacturing (LBAM) techniques such as selective laser melting (SLM), direct metal deposition (DMD), laser engineering net shaping (LENS) and wire-laser additive manufacturing (WLAM) usually produce a poor-quality surface finish, resulting from the layer-by-layer process which fails to fulfil industrial requirement [13,25]. Guo *et al*.[12] machined CoCrFeMnNi HEA, following fabrication using a selective laser melting (SLM) process. The surface finish could however not fulfil industrial requirements. Poor surface quality often deteriorates over time due to environmental factors such as the oxygen present in air and temperature [15]. The deployment of post-processing methods creates a reflective surface to prevent the contamination on the surface created by environmental substances [15]. There are various post-processing treatments used in AM metallic components to reduce surface roughness, such as electropolishing (EP), sandblasting, chemical polishing, centrifugal barrel finishing (CBF), ultrasonic polishing and oxidation polishing [13, 19].

CBF post-processing treatments have shown promising results in the deburring of compounds. The CBF operation requires the loading of a component in a rotating barrel that consists of ceramic media, polishing liquid and water. The rotation of the barrel generated an abrasion action that permits the micro-removal of the material [1]. The CBF operation enables the polishing of complex shapes and sizes with the added benefit of low maintenance costs [11,30]. De Beer *et al.*[9] polished low surface manufactured Alumide® jewellery in a tumbler using an abrasive media and obtained a smooth attractive metallic lustre surface. Tokarewicz *et al*.[27] developed barrel finishing methodologies to condition Ti6Al4V and inconel718 for complex geometries fabricated using SLM processes. The study confirmed a successful reduction of the surface roughness. Tsai *et al*.[28] investigated barrel finishing on wire arc additive manufactured (WAAM) components and found that their barrel finishing setup could successfully be used for material cleaning, material removal, deburring, and descaling of WAAM parts. However, in this process of polishing, there is a need for the operator to be highly involved, due to the manual loading and unloading of the sample(s).

The purpose of the study is to demonstrate the application of the CBF method for surface improvement on DMD AlCrCoCuFeNi HEA at different scanning speed. Optimum barrel finishing parameters were determined based on previous studies [13]. There is limited scientific research and mathematical model publications in the area of mass finishing with respect to HEAs.

2. Methodology and Materials

2.1 Materials

The chemical composition of commercially available AlCrCoCuFeNi HEA powder, used in this study, shown in Table 1. The as-received powder was supplied by F.J. BRODMANN & CO., L.L.C SUPPLIERS with each element purities above 99.9% and particle size distribution in the range of 32-140 µm. Figure 1 illustrates the scanning electron microscope

(SEM) image of the AlCrCoCuFeNi HEA powder. Before deposition, the Ti6Al4V baseplate was sandblasted to promote bonding between the alloy and the baseplate.

Table 1. Chemical Composition of AlCrCoCuFeNi Powder (wt. %)

Al	Cr	Co	Cu	Fe	Ni
25.52	12.28	27.57	1.29	30.02	3.32

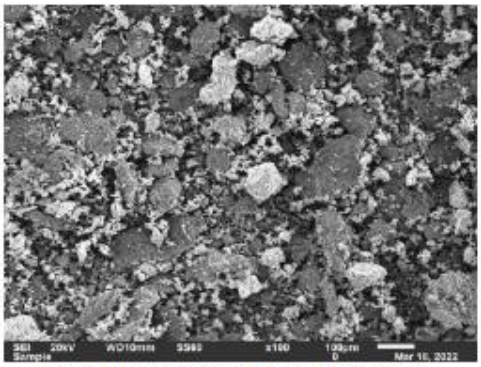


Figure 1. SEM Image of AlCrCoCuFeNi Powder

2.2 DMD Process

A KUKA robot [4, 26] with a 3 kW IPG [26] continuous fibre laser was used to deposit the AlCoCrCuFeNi HEA powder into an argon-controlled system, in order to protect the surface from oxidation. Six cubic DMD samples in the size 20 mm × 20 mm ×15 mm were fabricated at the National Laser Centre Council for Scientific and Industrial Research, South Africa. These samples will serve to demonstrate the application of the CBF method for surface improvement. Optimised parameters (see Table 2) based on previous studies were used [4]. The deposition process was carried out in a double crucible electric lifting melting furnace preheating furnace with model number RR3-50K at 600˚C [4].

Table 2. Laser process parameters of AlCrCoCuFeNi [4]

Sample	Laser Power (W)	Scanning speed (m/min)	Powder feed rate (rpm)	Beam diameter (mm)
a_2	1200	0.48	2.5	2
a_3	1200	0.48	2.5	2
b_2	1200	0.60	2.5	2
b_3	1200	0.60	2.5	2
c_2	1200	0.72	2.5	2
c_3	1200	0.72	2.5	2

2.3 Post-processing

The primary objective of this experiment is to determine the barrel finishing process for AlCrCoCuFeNi HEA parts. An industrial barrel finishing machine, CB320-CBF from the National Laser Centre Council for Scientific and Industrial Research, South Africa, was used to treat sample a_2, b_2 and c_2 using fixed machine parameters of 85 rpm for 14 hours. The finishing operation is performed on account of rotary movement with abrasive tumbling media to create a high centrifugal force and sliding friction. Angle cut ceramic media, with nominal dimensions of 10 mm x 10 mm was used. Figure 2 shows images of the CB320-CBF and the ceramic media used. The total quantity of the samples (a_2, b_2 and c_2), abrasive media, LC-13 polishing lubricant and water put in the tumbler is 11kg, accounting for the load of 50% volume in the tumbler. The change of water and LC-13 polishing liquid was executed after 14 hours to further improve the surface finish of the samples.



Figure 2. CB320-CBF Machine (I) and ceramic media (II)

2.3.1 Surface analysis

The surface roughness of the treated (a_2, b_2, c_2) and untreated (a_3, b_3, c_3) samples were measured before (a_3, b_3, c_3) and after (a_2, b_2, c_2) polishing and further analysed using a Taylor Hobson Strutronic S-100 series – roughness tester [24]. The surface morphology and composition were examined JEOL-JSM-6010PLUS/LA Analytical Scanning Electron Microscope (SEM) equipped with Energy dispersive X-ray spectroscopy (EDS) [7]. In addition, Gwyddion 2.9.32 software [29] characterised SEM images to obtain the topography and roughness profile of the samples.

3. Results and Discussion

Three samples were manufactured with DMD at three different scanning speeds. One sample at each scan speed was kept untreated (samples a_3, b_3, c_3) and the other samples were treated with CBF (samples a_2, b_2, c_2). The surface roughness of the untreated samples were measured to be a_3 = 13.78 µm, b_3 = 13.36 µm and c_3 = 17.36 and the treated sample a_2, b_2, c_2 was measured to be 7.63 µm, 5.59 µm and 5.68 µm respectively. The average surface removal trend per 3.5 hour is estimated to be 2 µm for a_2, 2 µm for b_2, and 3 µm for c_2 (see Figure 3). Insignificant improvement of the surface was observed after 14 hours of polishing time, consequently leading to a negligible surface progress. This was attributed to the excessive

impact caused by the centrifugal force which sequentially accumulated abrasiveness at the boundary of the barrel. Thus, a change of water and LC-13 polishing liquid was implemented however the samples showed an insignificant improvement in the surface finish. Boschetto *et al.*[1] barrel finished selective laser melting (SLM) Ti6Al4V parts, the processing time took 24 hours to give sufficient result. Khan *et al.* [16] used CBF to polish wire + arc additive manufactured samples, the water induced the samples to corrode thus more time was required to remove the corrosion. The samples experienced an insignificant improvement in the surface finish after 8 hours. The polishing of AlCrCoCuFeNi HEA gave an improved surface quality while experiencing low disorientation as opposed to the conventional alloys.

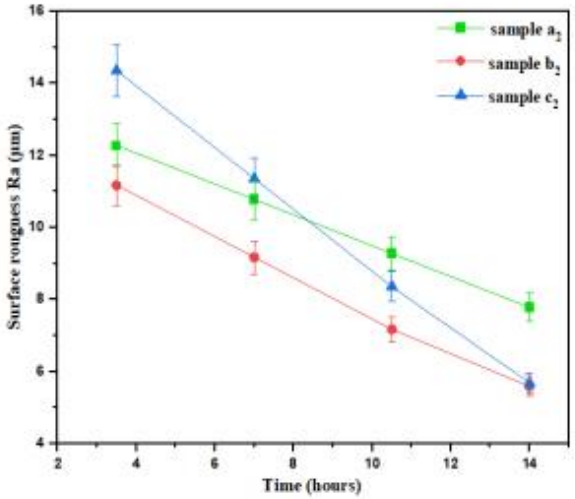


Figure 3. Surface roughness variation development with time at 85rpm

Figure 4 (i,) (ii) shows images of the treated CBF and untreated as-built samples. The barrel finishing process removed sloping plane 3i (A) (C) on the sides caused by the balling-effect. It could be seen that the finishing process removed the oxides effectively and additionally removed the some spatters 3i (A) (B).

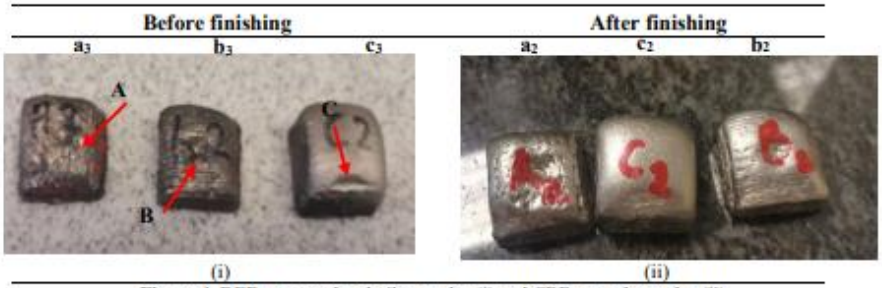


Figure 4. DED untreated as-built samples (i) and CBF treated samples (ii)

Figure 5, presents the average surface roughness comparison between as-build and CBF post-processing samples. From Figure 5 it can be observed that the as-built samples had a higher surface roughness, Ra, in comparison to the CBF polished samples. The low scan speed sample produced a higher surface removal and the high scan speed removal resulted in a lower surface removal. Hardinnawirda *et al*. [14] found that cooling rate have a significant effect on the mechanical integrity of the joint and as the cooling rate increase, the strength increases. Therefore, the increase in scanning speed is associated with an increase in the rapid cooling rates [5]. Thus, sample c_2 producing a lower surface removal because of the acquired strength.

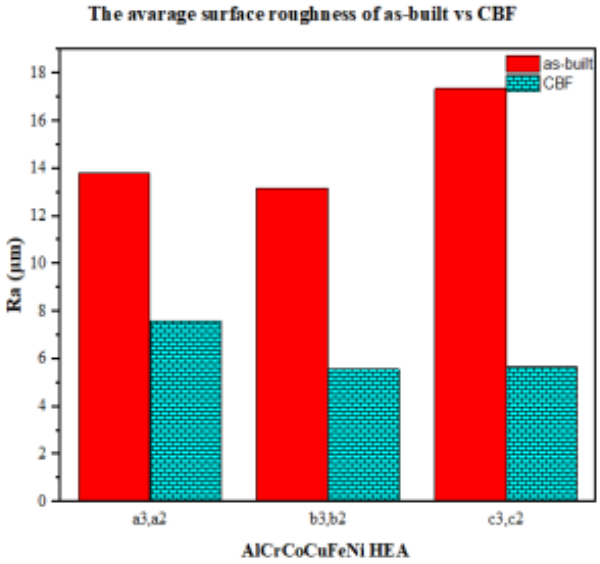


Figure 5. Graphical comparison between as-built to CBF

Figure 6 exhibits SEM images of CBF treated and untreated as-built samples. The untreated surface is affected by the balling effect which is more evident in sample c_3, thus leading to a greater Ra value. The polished samples contain embedded scratches Figure 6 (A, B, C), since the surface removal action is based on rubbing and deburring. The CBF process produced reduced surface roughness therefore smooth surface was obtained. The EDS analysis of the CBF polished samples confirms the chemical composition established in Table 1.

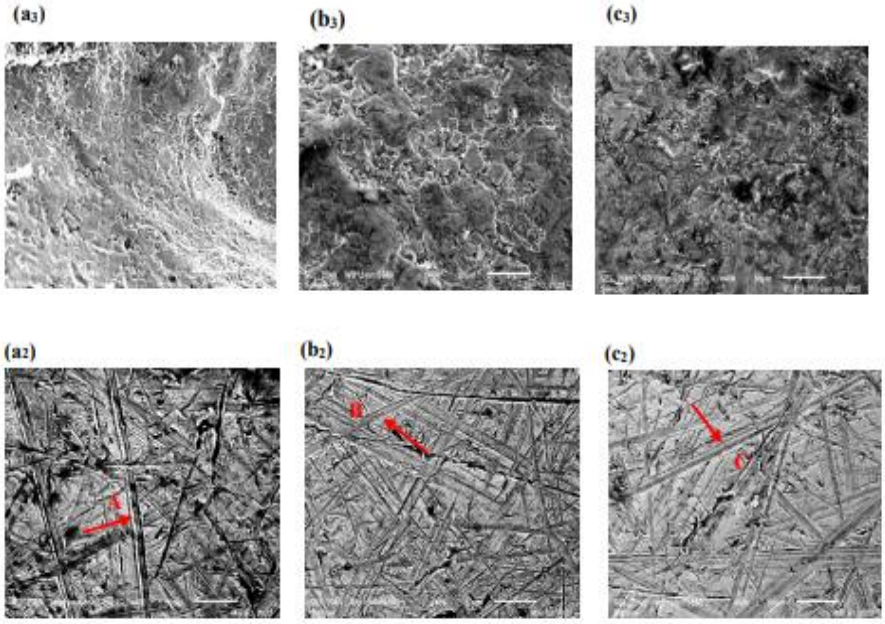


Figure 6. SEM images of untreated as-built samples (a_3,b_3,c_3) and treated CBF samples (a_2,b_2,c_2)

In Figure 6, samples a_3 and a_2 average surface roughness Ra is 13.78 µm and 7.63 µm respectively with the peak-to-valley, Rt, of a_3 = 159.55 µm and a_2 = 83.34 µm. The average roughness, Ra, was decreased by 55% Rt. Samples b_3 and b_2 had an Ra improvement of 13.17 µm to 5.59 µm for b_3 and b_2 respectively with Rt values of b_3= 131.85 µm and b_2= 74.49 µm amounting to a decrease of 42%. For samples c_3 and c_2 the Ra values decreased by 33% with the Ra values of 17.36 µm and 5.68 µm for c_3 and c_2 respectively. The Rt value was found to be: c_3= 168.47 µm and c_2= 64.06 µm. The as-built surface contains higher peak-to-valleys which dissolves to a lower surface area valley causing a polishing effect on the CBF surface [23].

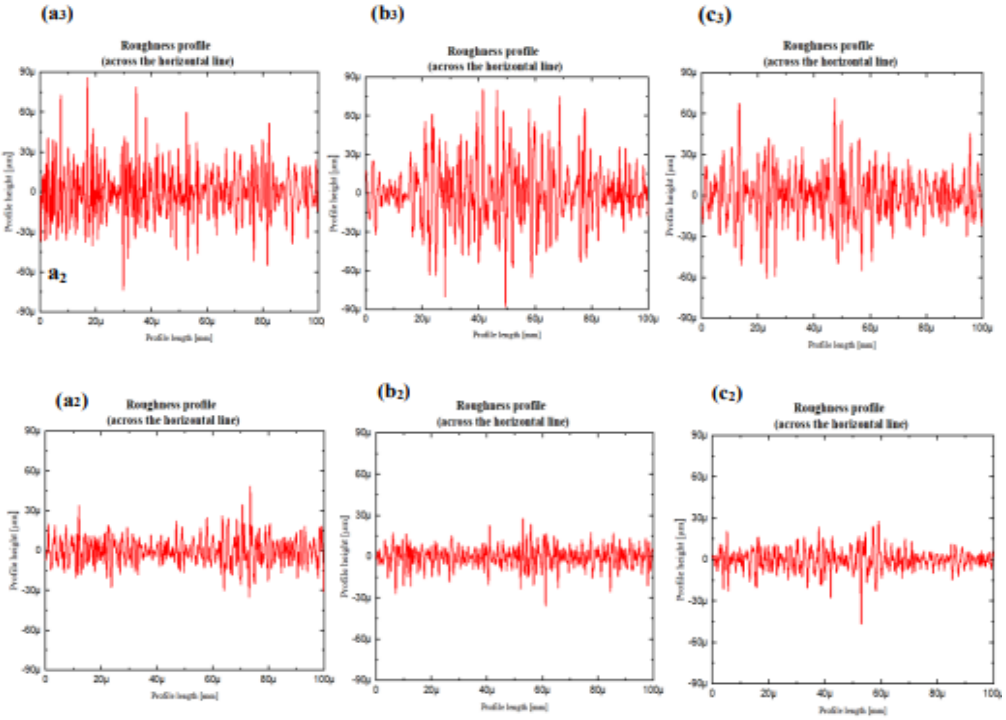


Figure 7. Roughness profile of the as-built (a_3,b_3,c_3) and CBF samples (a_2,b_2,c_2)

Figure 8, illustrates 3D topographical analysis for the as-built and CBF samples. There is a considerable difference in the peak-to-valley of the post-processing and as-built surface. The as-built sample a_3, b_3 and c_3 are characterised by the very high peaks-to-valley height rough surfaces are observed. After the 14 hour processing time CBF maps appeared to have an overall decreased peak-to-valley were a decrease of over 33% was observed. CBF produced samples which resulted in the smooth and improved surface quality of AM AlCoCrCuFeNi.

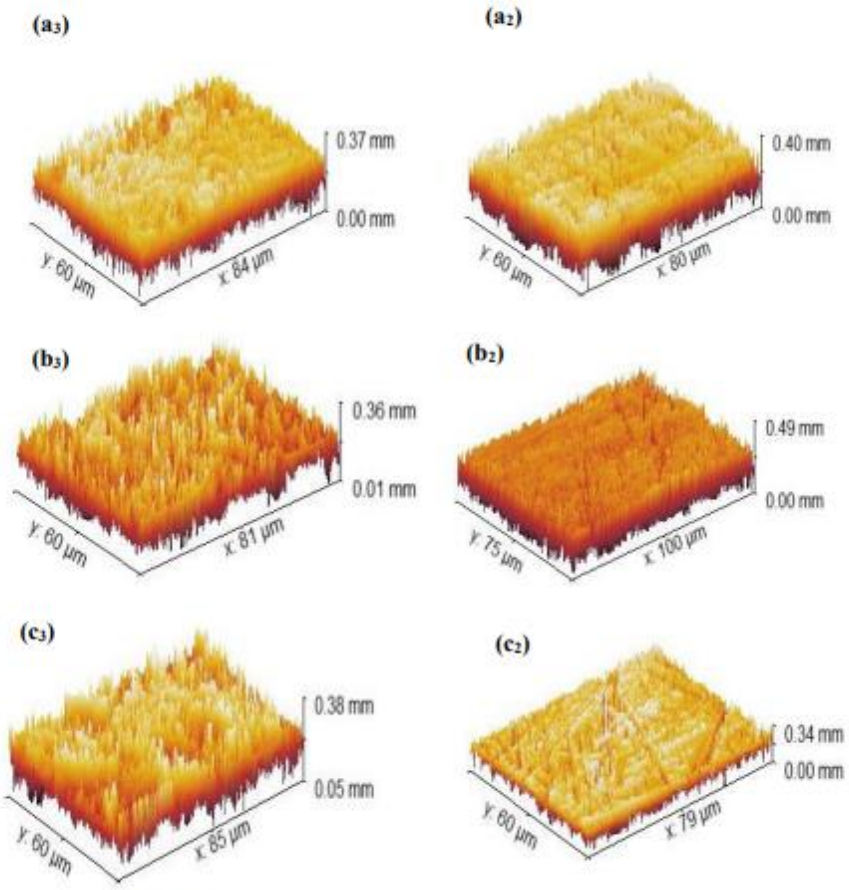


Figure 8. Three-dimension topographical representation of as-built (a_3,b_3,c_3) and CBF samples (a_2,b_2,c_2)

4. Conclusion

DMD plays a critical role in the production of complex parts, but the fabrication of surface quality remains a crucial aspect. This study investigated and analysed the CBF process of HEA samples.

The AlCrCoCuFeNi HEA fabricated at different scan speed and laser power, were treated using CBF post-processing methods to improve the external surface quality of the HEA. An improvement of 55% for a_2, 42% for b_2 and 33% for c_2 is observable. The CBF process on AlCrCoCuFeNi HEA has been found to produce an improved surface finishing with minimum complexity. CBF process produced smooth fine surface finish attributed to the process' easy sliding to all corners of the external surface. The scratched surface observed were caused by the ceramic media which could be avoided by changing to a less abrasive

media (such as plastic media) at the final stages of polishing. The lower scan speed sample produced an improved post surface finish due to lower cooling rates. More parameter variation such as laser power range and time interval is recommended for future work to observe polishing development.

Acknowledgement

The authors would like to thank the National Laser Center (Laser Enabled Manufacturing Research Group) at the Council for Scientific and Industrial Research, a notable appreciation to Mr Samuel Skosana for fabrication assistance, the Surface Engineering Research Laboratory at the Tshwane University of Technology, and the University of the Witwatersrand for their technical and scientific support.

References

1. BOSCHETTO, A., BOTTINI, L., MACERA, L. & VENIALI, F. 2020. Post-processing of complex SLM parts by barrel finishing. *Applied Sciences,* 10, 1382.
2. BOSCHETTO, A., BOTTINI, L. & VENIALI, F. 2013. Microremoval modeling of surface roughness in barrel finishing. *The International Journal of Advanced Manufacturing Technology,* 69, 2343-2354.
3. DADA, M., POPOOLA, P., ADEOSUN, S. & MATHE, N. 2019. High entropy alloys for aerospace applications. *Aerodynamics.* IntechOpen.
4. DADA, M., POPOOLA, P., MATHE, N., PITYANA, S. & ADEOSUN, S. 2020. Parametric optimization of laser deposited high entropy alloys using response surface methodology (RSM). *The International Journal of Advanced Manufacturing Technology,* 109, 2719-2732.
5. DADA, M., POPOOLA, P., MATHE, N., PITYANA, S. AND ADEOSUN, S., 2021. Effect of laser parameters on the properties of high entropy alloys: A preliminary study. *Materials Today: Proceedings*, *38*, pp.756-761.
6. DADA, M., POPOOLA, P., MATHE, N., PITYANA, S., ADEOSUN, S. & ARAMIDE, O. 2021. The comparative study of the microstructural and corrosion behaviour of laser-deposited high entropy alloys. *Journal of Alloys and Compounds,* 866, 158777.
7. DADA, M., POPOOLA, P., MATHE, N., PITYANA, S. AND ADEOSUN, S., 2022. In-situ reactive synthesis and characterization of a high entropy alloy coating by laser metal deposition. *International Journal of Lightweight Materials and Manufacture*, *5*(1), pp.11-19.
8. DADA, M., POPOOLA, P., MATHE, N., PITYANA, S., ADEOSUN, S. AND LENGOPENG, T., 2020. Fabrication and hardness behaviour of high entropy alloys. In *TMS 2020 149th Annual Meeting & Exhibition Supplemental Proceedings* (pp. 1581 1591). Springer, Cham.
9. DE BEER, D., BECKER, L., VAN DER WALT, P., MAUCHLINE, D., CAMPBELL, I. & DEAN, L. 2012. Additive manufacturing of alumide jewellery.
10. DMITRIYEV, S., KOUDRIN, A., LABUNETS, A. & KINDRACHUK, M. 2005. Functional coatings application for strengthening and restoration of aviation products. *Aviation,* 9, 39 45.
11. GILLESPIE, L. K. 1999. *Deburring and edge finishing handbook*, Society of Manufacturing Engineers.

12. GUO, J., GOH, M., ZHU, Z., LEE, X., NAI, M. L. S. & WEI, J. 2018. On the machining of selective laser melting CoCrFeMnNi high-entropy alloy. *Materials & Design,* 153, 211-220.
13. HABIBZADEH, S., LI, L., SHUM-TIM, D., DAVIS, E. C. & OMANOVIC, S. 2014, . Electrochemical polishing as a 316L stainless steel surface treatment method: Towards the improvement of biocompatibility. *Corros. Sci*, 87, 89–100.
14. HARDINNAWIRDA, K., AKHTAR, A.Z., AISHA, I.S.R. AND MAHADZHIR, I., 2016. A review on the effect of surface finish and cooling rate on solder joint reliability. *High Performance and Optimum Design of Structures and Materials II*, *166*, p.201.
15. HUANG, L. 2022. *Everything You Need to Know About Polishing Surface Finish* [Online]. Rapid Direct. Available: https://www.rapiddirect.com/blog/polishing-surface-finish [Accessed 24 March 2022].
16. KHAN, A., PATIDAR, M., PETARE, A., CHOUHAN, R., CHOUHAN, P., VISHWAKARMA, B., SHARMA, U., KAUSHAL, S., DHEPTE, D. & MADHUKAR, Y. 2020. Development of barrel finishing machine to improve surface finish of the wire arc additive manufactured parts. *Procedia CIRP,* 91, 330-335.
17. KHAN, A.U., PATIDAR, M., PETARE, A.C., CHOUHAN, R., CHOUHAN, P., VISHWAKARMA, B., SHARMA, U., KAUSHAL, S., DHEPTE, D. AND MADHUKAR, Y.K., 2020. Development of barrel finishing machine to improve surface finish of the wire arc additive manufactured parts. *Procedia CIRP*, *91*, pp.330-335.
18. LI, J., HUANG, Y., MENG, X. & XIE, Y. 2019. A review on high entropy alloys coatings: fabrication processes and property assessment. *Advanced Engineering Materials,* 21, 1900343.
19. LYCZKOWSKA, E., SZYMCZYK, P., DYBALA, B. & CHLEBUS, E. 2014. Chemical polishing of scaffolds made of Ti-6Al-7Nb alloy by additive manufacturing. . *Arch. Civ. Mech. Eng*, 14, 586–594.
20. MAZUMDER, J. 2017. Laser-aided direct metal deposition of metals and alloys. *Laser additive manufacturing.* Elsevier.
21. PROTOMATIC 2015. https://www.protomatic.com/about-us/newsletters/3d-printing/2015/10/arc-additive-or subtractive-manufacturing-methods.
22. RAINES, A. L., OLIVARES-NAVARRETE, R., WIELAND, M., COCHRAN, D. L., SCHWARTZ, Z. & BOYAN, B. D. 2010. Regulation of angiogenesis during osseointegration by titanium surface microstructure and energy. *Biomaterials*, 31, 4909-4917.
23. SEPÚLVEDA, M., QUINTERO, D., CASTAÑO, J. & ECHEVERRÍA, F. 2018. Improved two-step Brytal process for electropolishing of aluminum alloys. *Corrosion Science,* 136, 386-392.
24. SHAH, P., P. BHAT, AND N. KHANNA, *Life cycle assessment of drilling Inconel 718 using cryogenic cutting fluids while considering sustainability parameters.* Sustainable Energy Technologies and Assessments, 2021. 43: p. 100950.
25. STRANO, G., HAO, L., EVERSON, R. M. & EVANS, K. E. 2013. Surface roughness analysis, modelling and prediction in selective laser melting. *J. Mater. Process. Technol*, 213, 589–597.
26. TLOTLENG, M., B. MASINA, AND S. PITYANA, *Characteristics of laser In-situ alloyed titanium aluminides coatings.* Procedia Manufacturing, 2017. 7: p. 39-45.
27. TOKAREWICZ, M. & GRĄDZKA-DAHLKE, M. 2021. Review of Recent Research on AlCoCrFeNi High-Entropy Alloy. *Metals,* 11, 1302.

28. TSAI, M.-H. & YEH, J.-W. 2014. High-entropy alloys: a critical review. *Materials Research Letters,* 2, 107-123.
29. TSOEUNYANE, G.M., MATHE, N., TSHABALALA, L. AND MAKHATHA, M.E., 2022. Electropolishing of Additively Manufactured Ti-6Al-4V Surfaces in Nontoxic Electrolyte Solution. *Advances in Materials Science and Engineering*, *2022*.
30. TULINSKI, E. H. 1994. *Mass Finishing in: ASM Metals Handbook,* OH, USA, Surface Engineering.
31. YEH, J. W., CHEN, Y. L., LIN, S. J. & CHEN, S. K. High-entropy alloys–a new era of exploitation. Materials Science Forum, 2007. Trans Tech Publ, 1-9.